Persistent Radiative States in the Arctic: Drivers, Trends, and Model Representation

By
Cameron Bertossa

A dissertation submitted in partial fulfillment of
the requirements for the degree of

Doctor of Philosophy
(Atmospheric and Oceanic Sciences)

at the
UNIVERSITY OF WISCONSIN-MADISON
2025

Date of final oral examination: 1/22/2025

The dissertation is approved by the following members of the Final Oral Committee:
Tristan L'Ecuyer, Professor, Atmospheric and Oceanic Sciences
Elizabeth Maroon, Assistant Professor, Atmospheric and Oceanic Sciences
Till Wagner, Assistant Professor, Atmospheric and Oceanic Sciences
Angela Rowe, Assistant Professor, Atmospheric and Oceanic Sciences
Sam Stechmann, Professor, Mathematics

Abstract

Persistent Radiative States in the Arctic: Drivers, Trends, and Model Representation

by Cameron Bertossa

The Arctic climate is rapidly changing. The ability for the high latitudes to effectively emit longwave radiation to space is vital for shedding excess energy received in the tropics, thus regulating the global energy balance. Several Arctic field campaigns have found the presence of two preferred radiative states, each of which heavily modulate the surface energy balance, affecting whether processes such as the melting or freezing of ice and snow can occur. These states are characterized by persistent optically thick clouds ('opaque') rapidly transitioning to persistent optically thin clouds or cloud-free conditions ('transmissive'), and vice versa.

Using satellite observations, models, and in-situ measurements, we investigate the spatial and temporal occurrence of these states, their underlying mechanisms, models' ability to represent them, and their long-term trends. Our findings demonstrate that CloudSat and CALIPSO can effectively detect bimodal longwave flux distributions across the polar regions. We show that these two radiative states are ubiquitous throughout the Arctic and Antarctic and are connected to both liquid-containing and ice-only clouds. The frequency of these states varies by region and season.

Models, including reanalyses, struggle to represent the correct frequency of the two states. However, cloud-resolving, polar-specific products, such as the Arctic System Reanalysis, generally perform better than coarser global models. Due to the non-Gaussian nature of polar longwave flux distributions, some traditional model evaluation methods, especially those relying on monthly means, likely miss errors in the representation of these states entirely. Thus, we urge model evaluators to consider the existence of distinct states in their assessments and, more generally, to adopt evaluation methods that can assess non-Gaussian distributions.

Long-term observations from the North Slope of Alaska reveal that pronounced changes in downwelling longwave radiation are linked to changing frequencies of these states, specifically, a disappearance of transmissive conditions. These changes are linked to both local and non-local moisture processes, which contribute to the formation of optically thick clouds. This shift highlights a strong positive feedback mechanism, where decreasing the transmissive state amplifies the warming and moistening of the Arctic atmosphere, further promoting the opaque state. Any region prone to future sea ice loss may experience a similar feedback, and thus, a disappearance of the transmissive state.

"A dog will teach you unconditional love. If you can have that in your life, things won't be too bad."

Robert Wagner

Acknowledgements

There are so many people to thank for supporting me throughout this long process. First, I want to express my deepest gratitude to Tristan for allowing me to freely explore what interests me. When I began graduate school, I didn't (and still don't!) have a clear direction for my career. I just knew that I wanted to keep learning and pursue questions that were interesting to me. I can imagine this is a headache for an advisor whose job is to keep a student on track and is also constrained by the project funding the student's research. Despite this, Tristan has always supported my desire to pull at new threads, even when they diverged from my immediate project.

I'd also like to thank the rest of my committee: Angela, Liz, Sam, and Till. I wanted to put together a committee that I thought best represented AOS: kind individuals who are experts in their respective fields, yet who also value collaboration and appreciate the interdisciplinary nature of weather and climate science. At some point or another, I think I have stopped in each of your offices to get research and/or existential advice. The AOS department has done an excellent job with the recent wave of faculty hires over the past five years. With every new addition, I've felt a genuine push toward fostering a more inclusive and supportive department, one that prioritizes its students. I recognize that balancing teaching, advising, research, family, and life is not easy for you all. As a student, thank you for all the sacrifices you make for us; I've received email responses well past midnight by more than one of you.

To my fellow AOS students, thank you for making this an incredibly welcoming environment. Interacting with all of you has been the best reminder that I'm not alone in this journey and that there are so many others who can relate to my experiences. I'd like to give a special shout-out to my office mates, James Anheuser and Stephanie Ortland. I wish both of you (and your partners!) the very best in the future, and I'm excited to remain friends with you for years to come.

Lastly, I want to thank my non-academic support systems: my parents, siblings, and wife. While the days are busy in grad school, I've always found it challenging to talk about the work. It's not exactly exciting to share how you spent the better part of a day getting a colormap to be *just* right. Thank you for your patience, your understanding, and for putting up with me over the past five years.

Contents

List of Figures

List of Tables

Abbreviations

ARM-NSA	The **A**tmospheric **R**adiation **M**easurement's **N**orth **S**lope of **A**laska atmospheric observatory
ASR	**A**rctic **S**ystem **R**eanalysis
CALIOP	**C**loud-**A**erosol **L**idar with **O**rthogonal **P**olarization (aboard CALIPSO)
CALIPSO	**C**loud-**A**erosol **L**idar and **I**nfrared **P**athfinder **S**atellite **O**bservation
CESM	**C**ommunity **E**arth **S**ystem **M**odel
CPR	**C**loud **P**rofiling **R**adar (aboard CloudSat)
CRE$_{LW}$	Longwave **C**loud **R**adiative **E**ffect
DLR	**D**ownwelling **L**ongwave **R**adiation (at the surface)
DLR$_{clr}$	Clearsky **D**ownwelling **L**ongwave **R**adiation (at the surface)
ERA5	**E**CMWF **Rea**nalysis Version**5**
GCM	**G**eneral **C**irculation **M**odel
MERRA2	**M**odern-**E**ra **R**etrospective Analysis for **R**esearch and **A**pplications Version**2**
MYNN	**M**ellor-**Y**amada-**N**akanishi-**N**iino
OLR	**O**utgoing **L**ongwave **R**adiation (at the top of atmosphere)
P3	**P**redicted **P**article **P**roperties
PDF	**P**robability **D**ensity **F**unction
PWRF	**P**olar-optimized **W**eather **R**esearch and **F**orecasting Model
RCM	**R**egional **C**limate **M**odel
RCP	**R**epresentative **C**oncentration **P**athway

Chapter 1

Introduction*

The ability for the high latitudes to effectively emit longwave radiation to space is vital for shedding excess energy received in the tropics (Nakamura and Oort, 1988). Within this context, the polar regions can be thought of as Earth's thermostats, where processes that modify the amount of energy shed to space at the high latitudes not only affects the local energy balance, but also the amount of heat transported from lower latitudes and, thus, circulation patterns and global energy balance. Several Arctic regions (such as the Beaufort Sea, Amundsen Gulf, and north of Svalbard) have been found to have preferred radiative states, manifesting themselves as bimodality in longwave flux distributions (Stramler et al., 2011a, Raddatz et al., 2015, Graham et al., 2017). These states result in prolonged periods, ranging from days to weeks, where either minimal or

*This is a lightly modified introduction from: Bertossa, Cameron, and Tristan L'Ecuyer. "Two ubiquitous radiative states observed across the high latitudes." Journal of Climate 37.8 (2024): 2585-2610.

substantial longwave radiation is transferred from the surface to the lower atmosphere, with little intermediate behavior. Moreover, despite their persistence, transitions between these states occur rapidly, often within hours (Morrison et al., 2012).

In the high latitudes, downwelling longwave radiation plays a critical role in defining the surface energy balance. This energy balance ultimately regulates the surface temperature and the rate at which ice freezes (Shupe and Intrieri, 2004). As such, downwelling longwave radiation is highly correlated to many other surface characteristics (Lu and Cai, 2009, Kapsch et al., 2014, Nygård et al., 2019). However, it is becoming increasingly evident that the environmental characteristics of the Arctic, particularly those tied to radiation, may be changing more rapidly than anywhere else on Earth (Serreze and Francis, 2006, Overland et al., 2019, Ford et al., 2021). Consequentially, the frequency of the presented radiative states may also be changing. Critically understanding present day polar radiative properties, especially within the context of states that frequently occur, is essential to modeling how those properties affect the climate system.

Studies using data from The Surface Heat Budget of the Arctic Ocean (SHEBA) campaign (1997-1998) first highlighted the preference for two longwave flux regimes in the Arctic (Shupe and Intrieri, 2004, Stramler et al., 2011a, Persson et al., 2017). One of these modes is characterized as 'radiatively clear' (meaning a relatively large amount of energy can be exchanged from the surface to the atmosphere) while the other is 'radiatively opaque' (relatively little energy can be exchanged). These preferred radiative modes are frequently accompanied by recurring characteristics in temperature, humidity and pressure (Stramler

et al., 2011a, Morrison et al., 2012, Graham et al., 2017). As a consequence, Raddatz et al. (2015) finds that downwelling longwave flux is a relatively 'complete' descriptor of the Arctic state, indicating that if models can correctly capture the longwave flux behavior, then other climatic characteristics will likely be accurate as well. However, capturing the nature of these distributions goes beyond accurately describing their mean and variance, but also their higher moments (including modality). In fact, only capturing the mean and variance of these multimodal distributions and ignoring their non-Gaussian nature can lead to especially poor interpretations of the state of the climate (Bertossa et al., 2021).

Multiple studies have since followed to understand what processes lead to the existence of these preferred Arctic states (Kalesse et al., 2016, Graham et al., 2017, Sedlar et al., 2021), as well as how well they are represented in models (Cesana et al., 2012, Engström et al., 2014). Of particular importance is the role of moisture intrusions into the Arctic (Woods et al., 2013, Pithan et al., 2018). These frequent events, often occurring several times per month, can inject large amounts of moisture and aerosol that are not characteristic of the locally pristine, dry, and cold polar atmosphere (Woods and Caballero, 2016, Willis et al., 2018, Papritz et al., 2022). Such events are also thought to help maintain standing inversions in temperature and moisture (Pithan et al., 2018, Tjernström et al., 2019). These inversions allow for low-level clouds to have a strengthened radiative effect (Sedlar and Tjernström, 2009).

Arctic mixed-phase clouds have received much attention in particular since they can

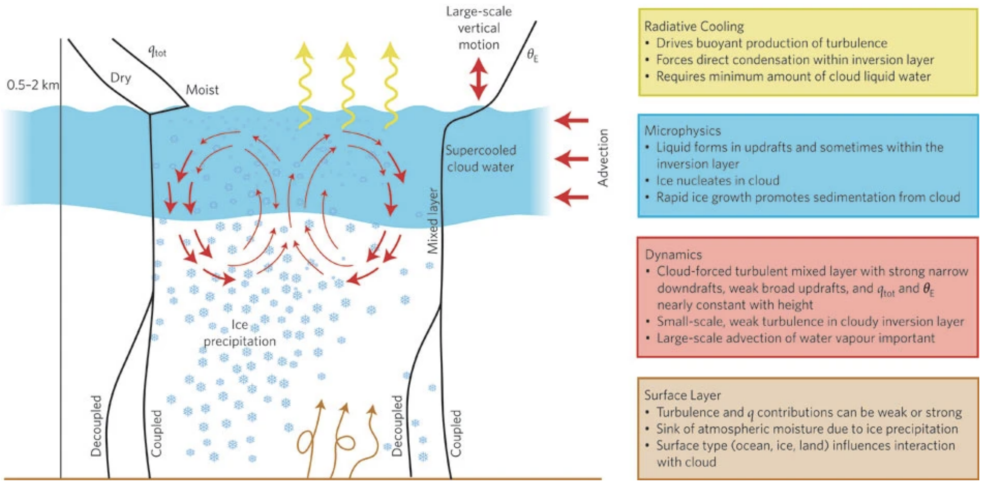

FIGURE 1.1: Figure 3 from Morrison et al. (2012): "The main features are described in text boxes, which are colour-coded for consistency with elements shown in the diagram. Characteristic profiles are provided of total water (vapour, liquid and ice) mixing ratio (qtot) and equivalent potential temperature (θ_E). These profiles may differ depending on local conditions, with dry versus moist layers/moisture inversions above the cloud top, or coupling versus decoupling of the cloud mixed layer with the surface. Cloud-top height is 0.5–2 km. Although this diagram illustrates many features, it does not fully represent all manifestations of these clouds."

persist for unusually long periods of time (10-14 days) and are typically optically thick due to the presence of liquid water (Shupe et al., 2006, de Boer et al., 2009, Fu et al., 2019, Tan and Storelvmo, 2019). This persistence is particularly remarkable given that ice particles typically grow at the expense of liquid water via the Wegener-Bergeron-Findeisen process (Bergeron, 1935, Findeisen, 1938). These clouds are exceptionally complex due to the interaction of large-scale, surface, and microphysical processes (see Fig. 1.1 for a 'simple' conceptual schematic). Due to these properties, mixed-phase clouds are often deemed the dominant driver for these preferred radiative modes (Persson et al., 1999, Morrison et al., 2012). That is, the existence of a low-level liquid containing cloud will lead to a relatively opaque atmosphere, and the lack thereof leads to a much more transmissive atmosphere.

However, ice clouds also enhance atmospheric emission to the surface in the absence of super-cooled liquid. For example, Van Tricht et al. (2016) showed that the frequency of ice clouds over Greenland is nearly 40% in the yearly mean, leading to about half of the increased meltwater runoff, and that cloud liquid water contributes only a fraction of the total radiative effect. Elsewhere within the Arctic, ice clouds are frequently observed to be geometrically thick and occur near the surface (Shupe, 2011), leading to large enhancements in longwave emission towards the surface. Therefore, studies explicitly analyzing how ice clouds are associated with each state are warranted.

Owing to the lack of systematic measurements, the documentation of these states beyond a limited number of localized campaigns is relatively minimal. Thus, it is often assumed that recurring transmissive and opaque radiative states exist to some extent across the Arctic Basin (Graham et al., 2017). However, the Arctic is highly inhomogeneous and so it is unclear if, why, and to what degree this bimodality persists across space and time. Furthermore, whether similar behavior exists in the southern hemisphere's polar region has yet to receive much attention.

The purpose of this dissertation is to explore the following research questions:

1. To what extent are bimodal longwave flux distributions observed across the Arctic and Antarctic?

2. What processes give rise to bimodal longwave flux distributions, and why are they seemingly unique to the polar regions?

3. How accurately do models, including reanalyses, represent the higher moments of longwave flux distributions?

4. How have these radiative states evolved over time, and how might they change in the future?

These research questions are further motivated and expanded upon in the subsequent chapters.

Chapter 2

Identification of Preferred Polar Radiative States*

*This is a lightly modified version of: Bertossa, Cameron, and Tristan L'Ecuyer. "Two ubiquitous radiative states observed across the high latitudes." Journal of Climate 37.8 (2024): 2585-2610.

2.1 Preface

As mentioned, the documentation of where bimodal longwave flux distributions are present in the Arctic is minimal. The purpose of this chapter is to characterize the downward longwave flux distributions for much of the high latitudes (poleward of 60 degrees), documenting where bimodality is present, indicating the presence of two preferred radiative states. To effectively sample throughout the poles, we use the unique capabilities offered by active satellite observations, specifically CloudSat and CALIPSO (Stephens et al., 2002). The differing sensitivities of these instruments allow for accurate mapping of cloud vertical structure, and are commonly used in the sparsely observed polar regions (e.g., McIlhattan et al., 2017, Morrison et al., 2018, Arouf et al., 2022). Atmospheric properties, whether those be cloud-induced or the clear-sky atmospheric fluxes, that lead to the existence of distinct transmissive and opaque states are investigated.

2.2 Dataset and Methodology

The launch of CloudSat and Cloud-Aerosol Lidar and Infrared Pathfinder Satellite Observation (CALIPSO) (Stephens et al., 2002) in 2006 offered unprecedented cloud characterization capabilities. In addition to mapping cloud vertical structure from 82°S to 82°N, the combination of CloudSat's cloud profiling radar (CPR) and CALIPSO's lidar measurements allow for effective classification of cloud phase and precipitation type (among other cloud properties). Furthermore, since the CPR is sensitive to ice particles while the lidar is sensitive to liquid water, the combination of the two instruments allows

for the identification of mixed-phase clouds, a capability much more limited on previous spaceborne sensors. Numerous studies have since leveraged products derived from the instruments' synergistic measurements (L'Ecuyer et al., 2008, Kay et al., 2016, Matus and L'Ecuyer, 2017, Ham et al., 2017, and the references therein). We give a brief overview of several CloudSat-CALIPSO products used throughout this study.

2.2.1 Clouds and Radiation

The 2B-CLDCLASS-LIDAR product (a level 2 product pertaining to CLouD CLASSification, Sassen et al., 2008) allows for reliable cloud phase detection for up to 10 cloud layers for each scene, with an attached quality flag (from 1-10) for each classification. To determine phase, this product uses co-located CALIOP L1 measurements with CPR footprints. The CALIPSO lidar and CloudSat radar attenuate differently due to microphysical distinctions between water and ice particles (size, shape, number concentration). Cloud phase is effectively determined using the different sensitivities of the radar and lidar, in conjunction with the cloud temperature (Wang et al., 2013). The 2B-CLDCLASS-LIDAR phase determination algorithm is rooted in ground-based observations (Sassen et al., 2008).

As recommended by the product guidelines, only classifications which exceed a quality flag of 5 are used for analysis. Since high-altitude clouds in the polar regions are relatively transmissive, the lidar-radar signal can often reach the lower cloud layers, allowing for sampling of the full vertical column. Thus, quality flags below 5 are found to occur in less than 5% of polar clouds. Following Matus and L'Ecuyer (2017), a scene's cloud type

is defined as 'liquid' if only a single liquid-containing cloud layer is detected, 'ice' if only a single ice-containing cloud layer is detected, 'mixed-phase' if only a single cloud layer in which both liquid and ice are ubiquitous is detected, and 'multilayer' if multiple cloud layers are detected (where these layers may or may not be of the same phase classification). This relatively simple classification provides valuable insights into cloud characteristics while avoiding more subjective definitions that can be difficult to emulate in models or other datasets.

The 2B-FLXHR-LIDAR product (FLuXes and Heating Rates, Henderson et al., 2013) models the radiative flux (longwave and shortwave) for each 240 m height bin sampled by the CPR from the surface to 20 km, based on the measured reflectivity of each instrument. 2B-FLXHR-LIDAR derives cloud water content values through the 2B-CWC (cloud water content) product, but is supplemented by optical depths from the MOD06-1KM-AUX product (when available) (Austin et al., 2009). The fifth release of 2B-FLXHR-LIDAR also enhances previous versions by incorporating explicit retrievals of ice water content (IWC) and effective radii through the 2C-ICE product (Deng et al., 2015). Atmospheric profiles of water vapor, temperature, and ozone are determined from ECMWF analyses. While each product has some amount of uncertainty, the combination of CALIOP and CPR are especially effective in the polar regions since attenuation typically only occurs for clouds very near the surface, allowing for effective characterization of the profile. Furthermore, 2B-FLXHR-LIDAR shows good agreement with the Clouds and the Earth's Radiant Energy System (CERES) observations (Wielicki et al., 1996, Henderson et al., 2013). Uncertainties are discussed more explicitly in the next section.

As in Raddatz et al. (2015), we examine these radiative regimes through surface Downwelling Longwave Radiation (DLR) rather than net longwave radiation at the surface (which includes surface emission). The latter includes the strong influences of surface type and temperature, making it harder to isolate atmospheric effects. In a similar vein, while shortwave fluxes are briefly examined in the conclusions, they are not used to directly identify the presence of preferred polar radiative states since incident solar radiation varies greatly over the annual (and diurnal) cycle. 2B-FLXHR-LIDAR also includes radiative fluxes should all clouds be removed from the scene (referred to as 'clear-sky'). We examine the clear-sky DLR at the surface (DLR_{clr}) to understand what influence the residual atmospheric flux (i.e., that caused by the emissivity of water vapor and other atmospheric constituents) has on the surface energy balance. The Cloud Radiative Effect (CRE) is a commonly used metric to estimate the effect that a cloud has relative to the clear-sky flux (Shupe and Intrieri, 2004, Zhao and Garrett, 2015, Alkama et al., 2020, Shaw et al., 2022). Focusing on the longwave fluxes caused by these preferred states, we limit analysis to just the longwave portion of CRE. This can be simply defined as $\mathrm{CRE}_{LW}=\mathrm{DLR}-\mathrm{DLR}_{clr}$. We present an example swath with these three defined variables of interest in Fig. A.1.

Due to a CloudSat battery anomaly that occurred in 2011, observations beyond this point are limited to daytime only. To capture complete seasonal variations in polar regions, we limit this analysis to only those observations which took place from 2007 through 2010 (four years), prior to the anomaly.

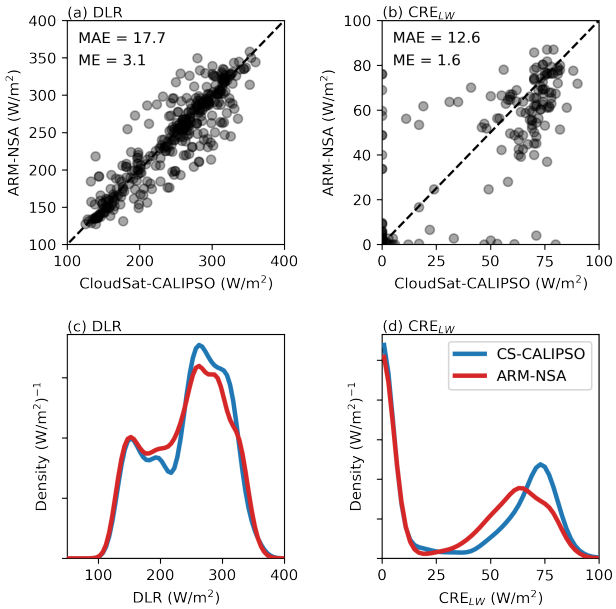

FIGURE 2.1: (a) Surface downwelling longwave radiation (DLR) derived from the CloudSat-CALIPSO 2B-FLXHR-LIDAR product versus co-located ARM-NSA hourly-averaged measurements for 2007 to 2010. The mean absolute error (MAE) and mean error (ME) are listed at the top left of the panel. (c) The PDFs of those values in (a). (b,d) as with (a,c) but for CRE_{LW}. Note that in (b,d) only observations in which the NSA dataset identifies the cloud fraction to be 0% or 100% are used, this avoids discrepancies caused by partially cloudy field of view that are not present in the CloudSat-CALIPSO dataset.

2.2.2 Reliability of CloudSat-CALIPSO

Being a spaceborne instrument, one may question CloudSat-CALIPSO's ability to effectively sample conditions just above the surface. We first validate its radiometric accuracy against co-located ground-based measurements. There are several options for ground-based validation, however, the Atmospheric Radiation Measurement (ARM) North Slope of Alaska (NSA) site (71.4 ^{o}N, 156.7 ^{o}W) at Utqiagvik (formerly known as Barrow), Alaska, offers some of the most persistent measurements of the Arctic state (1998-present) (Stamnes et al., 1999). Many previous studies of Arctic weather and climate have relied on this site's measurements (Dong and Mace, 2003, Kay et al., 2008, Shupe, 2011). Here,

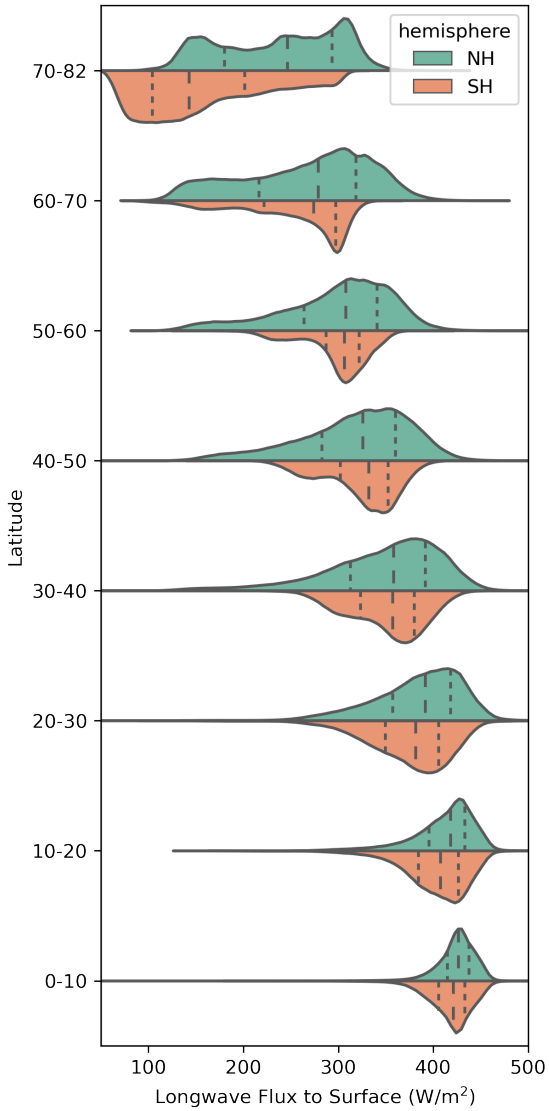

FIGURE 2.2: Density plots of surface downwelling longwave radiation derived from the CloudSat-CALIPSO 2B-FLXHR-LIDAR product for various latitude bins. Green distributions represent the northern hemisphere portion of the latitude bin and orange is for the the southern hemisphere. Vertical dashed lines within each distribution indicates the separations of the quartiles.

downwelling longwave radiance measurements are captured by a sky radiometer on a stand (Andreas et al., 2018): this is a direct measure of radiation, and using a model for estimating atmospheric profiles is not required.

Figure 2.1a provides a scatter plot of DLR for co-located CloudSat-CALIPSO and ARM-NSA observations (Zhang, 2003) from 2007 to 2010. Since CloudSat overpasses rarely occur directly overtop the NSA site, we consider overpasses within a 1 degree by 1 degree box centered on the NSA site. That is, co-location in space and time are not exact. Differences further arise through the distinct fields of view provided by each instrument. Despite this, observations generally agree with one another, with an DLR mean absolute error of 17.7 W/m^2 and a mean error of 3.1 W/m^2. The PDFs of the two datasets also match relatively well (Fig. 2.1c). This is consistent with McIlhattan et al. (2017) who performed similar comparisons against ground-based observations at Summit Station, Greenland. We further compare the observed values of CRE_{LW} of the two datasets (Fig. 2.1b,d). Once again, values generally agree with one another, and the PDFs of the two datasets look quite similar. Cases in which there are larger differences between the two datasets may arise from the discrepancies in time and space co-location, noting that, the NSA station is located near the coast where spatial inhomogeneities are large.

As a means of increasing confidence in the ability for CloudSat-CALIPSO to sample radiative conditions just above the surface, we refer the reader to a study by Liu (2022) which estimates the uncertainties in radiation flux due to limitations in CloudSat-CALIPSO detection over the Arctic ocean. Using SHEBA observations as inputs to QuickBeam (Haynes et al., 2007), a multipurpose radar simulation package to simulate the CloudSat reflectivity, a (simplified) CloudSat-CALIPSO cloud mask is derived. Comparing computed radiation fluxes with all clouds (as determined by SHEBA observations) versus only those detected by CloudSat-CALIPSO results in absolute differences less than 1 W/m^2

69% of the time in the yearly mean. The largest differences are on the order of 10-20 W/m^2, which occurs approximately 5% of the time in the yearly mean. Since CALIOP is not often attenuated prior to reaching the polar surface (due to low liquid water amounts in the upper atmosphere) it can frequently capture even low-level cloud tops. Even when CALIOP is attenuated prior to reaching the cloud base, the FLXHR algorithm utilizes an estimated lifted condensation level to predict cloud base. While this may not capture the precise location of cloud base, the radiative influence of extending the cloud base into the obscured zone near the surface is relatively small (approximately 1.5 W/m^2 per 250 meters; Henderson et al., 2013). This reflects the fact that while it is important to be aware of these limitations of satellite observations, they are generally much smaller than the difference between transmissive and opaque states discussed below and do not significantly impact the presented results.

2.3 Multimodality in Longwave Flux

Already evident in Fig. 2.1b are two distinct peaks in DLR that are captured in both the Cloudsat-CALIPSO and ARM datasets. A first logical question that follows from this result is: to what extent is this behavior unique to the Arctic?

2.3.1 Global Properties

DLR distributions from 2B-FLXHR-LIDAR for various latitude bins are presented in Fig. 2.2. As supported by previous campaign studies, there is clear multimodal behavior evident in DLR, especially in the high Arctic (70-82 ^{o}N). Equatorward, however, variance

not only decreases, but the existence of a transmissive mode (defined by occurrences of DLR around 150 W/m^2) also vanishes.

In the poleward-most bins, the differing radiative properties of the northern and southern hemisphere are more evident. In the highest latitude bin, for example, not only is the southern hemisphere distribution shifted to lower values (representing a more transmissive atmosphere), but the shape, particularly the modality, is very different than the northern hemisphere. It is not until 30-40 ^{o}N/S that the southern hemisphere nearly mirrors the northern hemisphere DLR distribution. Notably, there is a strong discontinuity between the Antarctic continent's DLR distribution (70-82 ^{o}S) and the surrounding ocean (60-70 ^{o}S). That is, inhomogeneity across neighboring latitude bins is especially large in the southern hemisphere.

2.3.2 Defining Regions

Separating climatically distinct regions is an especially important process when analyzing cloud feedbacks in the Arctic (Morrison et al., 2018). As supported by the latitudinal discontinuities present in Fig. 2.2, as well as previous studies relating to inhomogeneities in cloud properties, surface type, and moisture advection across the Arctic and Antarctic (see, for example, Cesana et al., 2012, Matus and L'Ecuyer, 2017), the multimodality exhibited in polar DLR distributions is explored with physically smaller regions than the pan-polar views in Fig. 2.2.

To form these regions, a hierarchical clustering algorithm is applied (Sasirekha and Baby,

2013). First, CloudSat-CALIPSO data is grouped onto a regular 2x2° grid. Then, for each 2x2° gridbox, a probability density function of DLR is estimated (using the native CloudSat-CALIPSO observations) using a histogram with bin widths of 5 W/m^2 (this is larger than the error in nearly 90% of cases analyzed by Liu, 2022). Finally, gridboxes are clustered based on the Euclidean distance between density functions (average linkage method). Mathematically the distance between density functions in two gridboxes p and q can be represented by:

$$d(\vec{p}, \vec{q}) = \sum_{i=1}^{n} (p_i - q_i)^2$$

where $\vec{p}$ represents a gridbox's estimated density function (using n bins) and p_i is the normalized count for bin i.

This clustering procedure offers several advantages: a) regions of similar behavior in longwave fluxes are identified (and, therefore, unique regions indicate distinct behavior), b) if the formed regions are relatively homogeneous, samples across gridboxes can be pooled together, increasing the sample size for each of the formed distributions, and c) we avoid mixing regions with very different weather and/or climate characteristics, which risks washing out important signals in the processes leading to multimodality.

Typically, one determines a priori the appropriate number of clusters to be formed by the clustering routine; however, since there is no indication as to what the 'correct' number of clusters should be in this case, several options are explored. Figure 2.3 depicts the

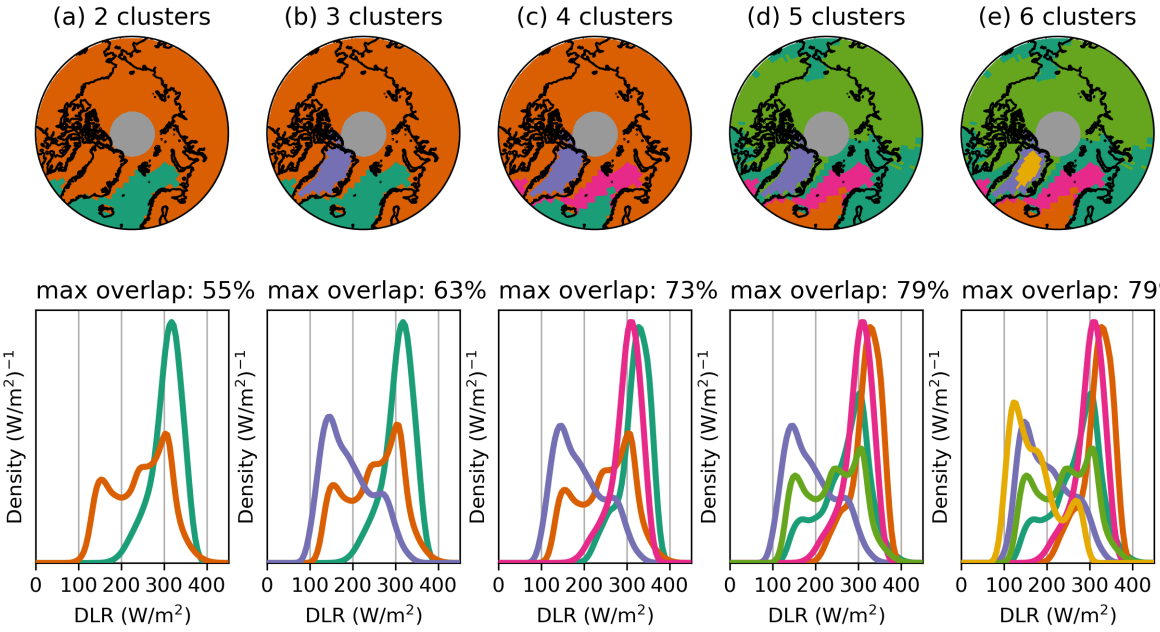

FIGURE 2.3: Formed clusters using compiled PDFs of DLR for the CloudSat-CALIPSO dataset. Each panel is labeled with the number of clusters to be formed. Each color corresponds to a unique cluster. The top row depicts the gridboxes which belong to each cluster. The bottom row depicts the PDFs of DLR from those formed clusters. For each set of clusters, the maximum overlapping area for any two distributions is listed (a higher percentage represents more similar distributions).

groupings that result from various numbers of clusters applied to the northern hemisphere data. Immediately several insights can be gained from the clustering process itself. For example, the moisture intrusion region near the North Atlantic storm track is labeled unique from the remainder of the Arctic domain (Fig. 2.3a). This is perhaps not a surprising result considering water vapor is an effective emitter of longwave radiation. Ultimately, this leads to a left skewed distribution with a mode around 310 W/m^2, versus the remainder of the Arctic which continues to exhibit multimodal behavior. Three clusters leads to the separation of the Greenland ice sheet, which has relatively low DLR values, representing the most transmissive portion of the Arctic (Fig. 2.3b). Increasing the number of clusters beyond three leads to smaller differences in the derived PDFs, with

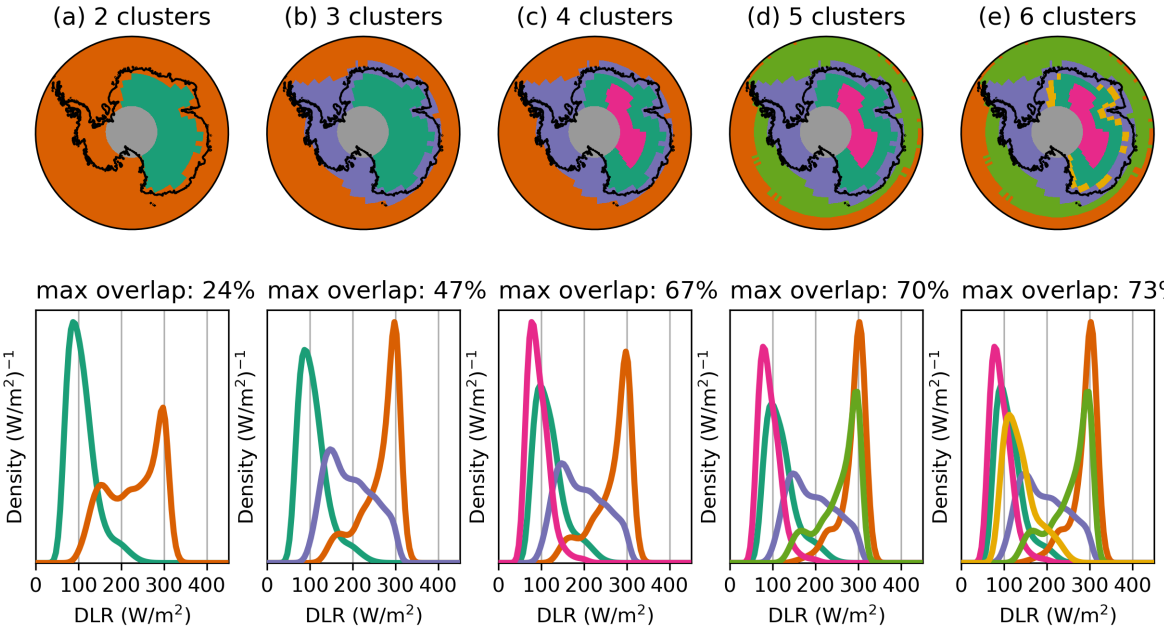

FIGURE 2.4: As Fig. 2.3 but for the southern hemisphere.

more minute subdivisions of the moisture intrusion region. This is further represented by a saturation in the overlapping percentage of any two distributions, where the addition of a fourth cluster (and beyond) leads to relatively high distributional overlap (approximately 75-80%). We conclude that, for our purposes, using four or more clusters over-fits the data and find that three clusters (Fig. 2.3b) yield sufficiently distinct PDFs while still sampling geographically diverse areas (such as the North Atlantic storm track, the central Arctic, and Greenland). Fig. A.2 depicts several other geophysical variables within the northern hemispheric domain and their respective PDFs as separated by the regions formed in Fig. 2.3b. The regions are clearly unique in properties other than DLR, providing further justification in defining distinct regions versus mixing the entire domain.

A similar process is repeated for the southern hemisphere (Fig. 2.4), noting that the clusters formed here have no relation to those formed in the northern hemisphere. As hinted

in Fig. 2.2, the two most distinct regions within this domain are the Antarctic continent and the nearby surrounding ocean (Fig. 2.4a). The third unique cluster separates the higher elevation Antarctic Plateau from the surrounding sea ice and lower elevation ice sheet. Compared to the Arctic, the Antarctic is seemingly less homogeneous in general, where DLR distributions have less overlap for the same number of clusters. For similar reasons as the Arctic, three clusters are also thought to sufficiently represent the polar region in the southern hemisphere (Fig. 2.4b).

While some subjectivity is introduced into the region formation process based on aggregated gridbox size, the number of clusters to be formed, and the particular clustering algorithm, this study does not necessarily intend to find 'optimal regions', but rather, convey that there are *relatively* homogeneous regions that exhibit differing DLR behavior. One may wish to modify the clustering routine for their particular purpose; for example, a greater number of clusters may be required if one wishes to examine more specific regional characteristics. That being said, confidence in this procedure can be given through prior studies. For example, the clusters formed in Fig. 2.3b approximately align with the perennial sea ice mask derived from Morrison et al. (2018). Furthermore, the clusters formed in Fig. 2.3e align with the regions derived in Naakka et al. (2018), which separates the Arctic based on lower tropospheric specific humidity. The geophysical properties tied to the regions formed in both of these prior studies are strongly linked to longwave radiation characteristics.

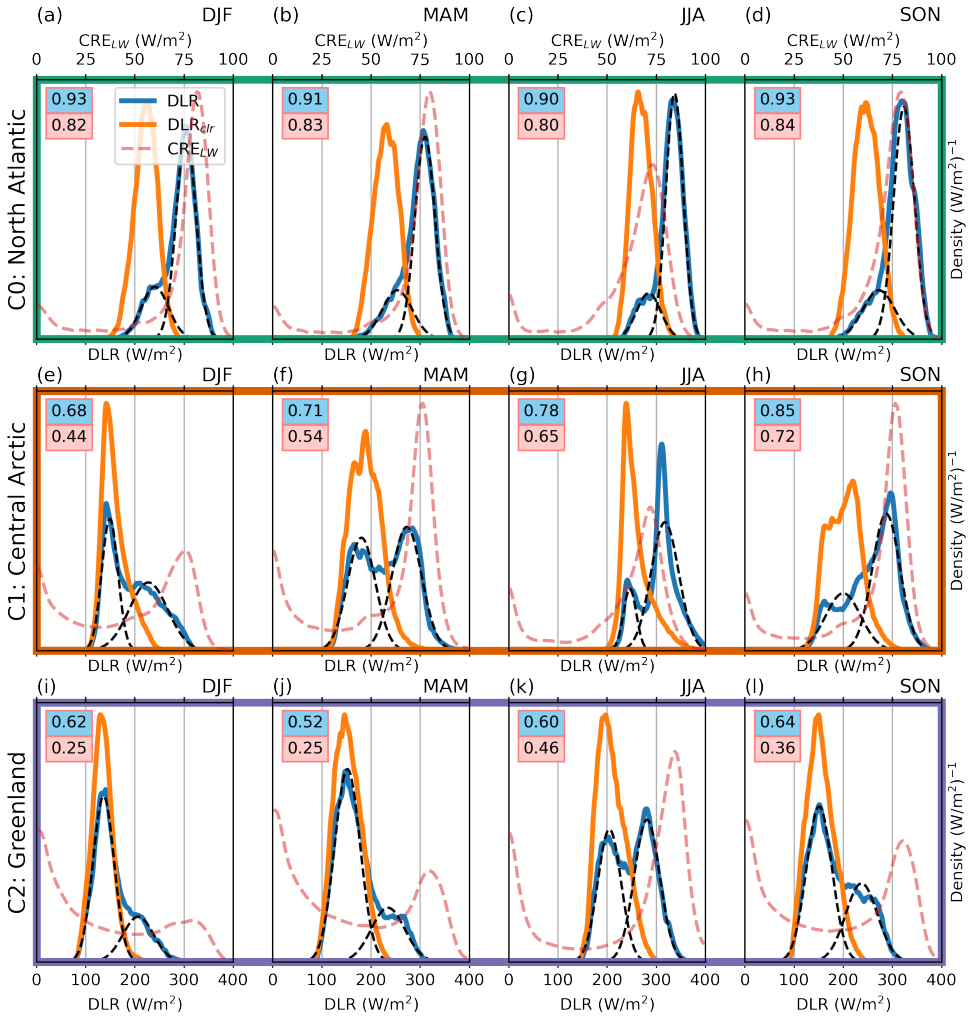

FIGURE 2.5: DLR$_{clr}$ (orange), DLR (blue) and CRE$_{LW}$ (red dashed) density functions of the unique regions in Fig. 2.3b. Only cloudy scenes are included in the CRE$_{LW}$ density functions, since, by definition, cloud-free scenes will have a CRE$_{LW}$ of 0. Each row contains a different region, where boxes are colored to match with those in Fig. 2.3b. Each column depicts a different season. For each panel, the fraction of time in which scenes are identified as cloudy is listed in blue and the fraction of time in which the CRE$_{LW}$ is >40 W/m^2 (relative to all scenes) is listed in red. For all DLR distributions, a two-mode Gaussian mixture model has been fit (black dashed), whose parameters are listed in Tab. A.1.

2.3.3 Seasonal Behavior

Once regions with similar DLR properties have been formed, the risk of mixing climatically distinct regions (which in turn may have distinct processes leading to multimodality)

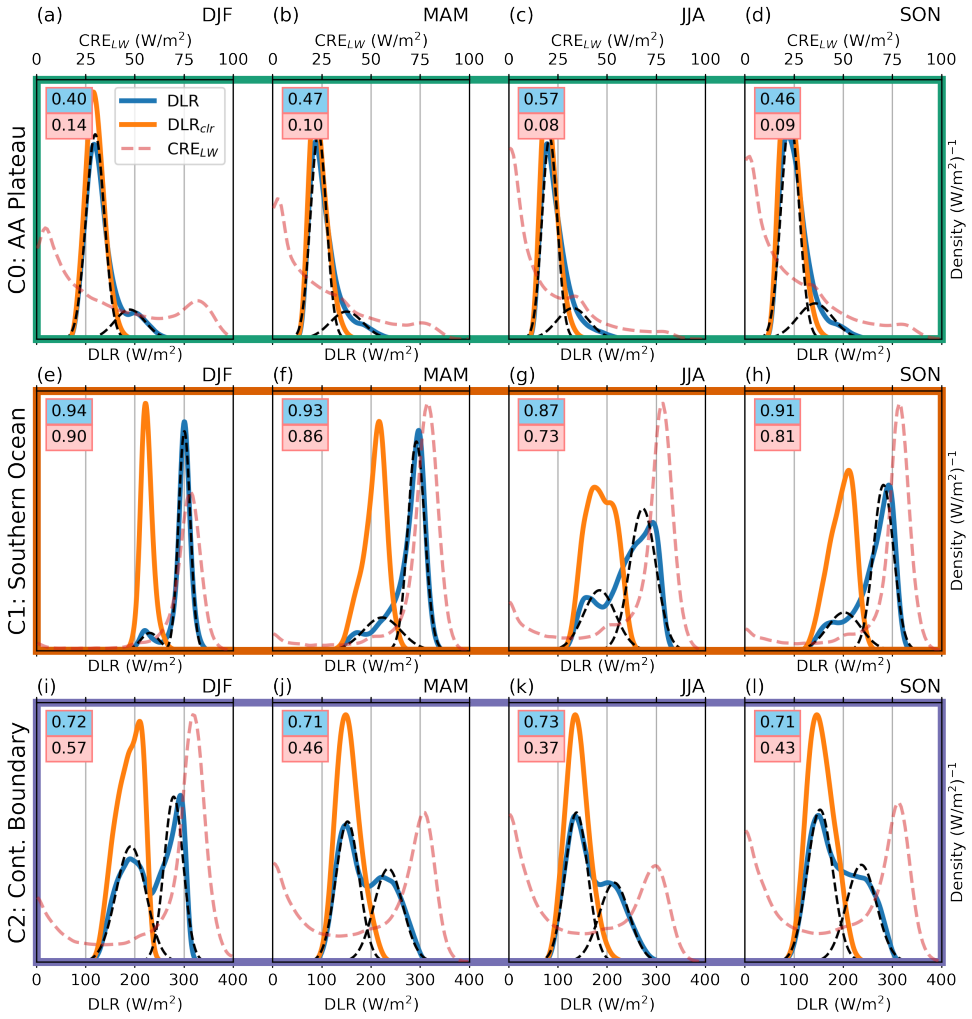

FIGURE 2.6: As Fig. 2.5 but for the southern hemisphere clusters (Fig. 2.4b).

is reduced. Figure 2.5 shows seasonal distributions of DLR, DLR$_{clr}$, and CRE$_{LW}$ for the three different Arctic clusters (complementary, Fig. A.3 presents these same distributions for a single randomly sampled 2x2° gridbox belonging to each region). Physically, DLR$_{clr}$ is the background atmospheric flux driven by emission from water vapor, carbon dioxide, and other atmospheric constituents and CRE$_{LW}$ represents the effect of clouds in modulating the longwave flux emitted towards the surface.

Remarkably, relatively few clear-sky distributions exhibit multimodal behavior; though

there are exceptions, such as the central Arctic during fall and spring. The unimodality in DLR_{clr} supports previous insights that the documented bimodality in longwave flux distributions is generally not forced by the humidity and temperature distributions directly, but rather, the clouds which form under those conditions.

This insight is directly exhibited in distributions of CRE_{LW}. Despite considering regions that are geographically diverse, two prominent modes emerge in CRE_{LW} for every region. One mode occurs near 0 W/m^2 and the other near 75 W/m^2. The latter aligns well with previous ground-based studies from the North Slope of Alaska (Shupe and Intrieri, 2004). There are relatively few occurrences of CRE_{LW} between 5 W/m^2 and 40 W/m^2. For succinctness, in the following discussion, scenes fall into the 'transmissive cloud mode' if they have a CRE_{LW} less than 5 W/m^2 and scenes fall into the 'opaque cloud mode' if they have a CRE_{LW} greater than 40 W/m^2. Note, however, that a cloud need not have an emissivity much less than one for it to fall in the transmissive mode, it may simply emit from a level such that it does not have an effect on surface longwave radiation. For all regions, cloud frequency typically reaches a maximum in the fall (Fig. 2.5d,h,l), as does the opaque cloud frequency (with the exception of Greenland, which peaks in the summer). The properties of these CRE_{LW} modes (for example, frequency and variance) directly influence the degree to which multimodality is exhibited in DLR distributions.

To quantitatively distinguish DLR distributions with multiple modes, we fit each DLR distribution with a two-mode Gaussian mixture model of the form:

$$p(x) = w\mathcal{N}(x; \mu_t, \sigma_t) + (1 - w)\mathcal{N}(x; \mu_o, \sigma_o)$$

where $\mathcal{N}(\mu_t, \sigma_t)$ is a Gaussian distribution representing the more transmissive mode with a weight of w, and $\mathcal{N}(\mu_o, \sigma_o)$ is a Gaussian distribution representing the more opaque mode with a weight of $(1 - w)$. Distributions are fit by minimizing the log loss of the Gaussian mixture model. Finally, we use these parameters to estimate the Ashman's D statistic (Tab. A.1, Ashman et al., 1994), defined as:

$$D = \sqrt{2}\frac{\mu_o - \mu_t}{\sqrt{\sigma_o^2 + \sigma_t^2}}$$

Larger D values indicate greater separation of the modes and a value larger than 2 is thought to indicate 'distinct' separation (i.e., multimodality).

Intuitively, nearly all the DLR distributions have a mode matching the DLR_{clr} mode (Fig. 2.5e-h, i-l): scenes that fall within this mode are cloud-free or have a transmissive cloud ($\text{CRE}_{LW} \approx 0$ W/m^2). As the opaque cloud mode increases in frequency, more scenes shift to a relatively opaque state (approximately +75 W/m^2 relative to DLR_{clr}). And thus, the opaque mode of the mixture model increases in weight ($w \to 0$).

With this in mind, discussion now focuses on each region, beginning with the central Arctic which has the clearest instances of multimodality in DLR (Fig. 2.5 second row). In winter and summer DLR_{clr} distributions are unimodal and have relatively little spread,

with a mean of approximately 150 W/m^2 and 250 W/m^2, respectively. Larger variance in DLR occurs during the shoulder seasons, mainly driven by an increase in DLR$_{clr}$ variance. That being said, an opaque cloud mode with small variance and frequency of approximately 40% to 70% for each season leads to relatively well defined modes.

The North Atlantic region (Fig. 2.5 first row) is not only nearly always cloudy (approximately 90% of the time), but these clouds are also frequently opaque. This behavior, rather than leading to two distinct evenly-weighted modes, essentially translates the DLR$_{clr}$ distribution by +75 W/m^2 to an 'always opaque state'. This effect is clearest when the opaque clouds are the most frequent (Fig. 2.5d, 84% of scenes reside in the opaque cloud mode), and is further reflected by values of w approaching 0 and decreasing values of D (Tab. A.1).

The Greenland cluster (Fig. 2.5 third row) has CRE$_{LW}$ modes which vary significantly as a function of the season. Not only do clouds occur less frequently in this region, but the clouds are also infrequently opaque (especially in the winter). While the opaque cloud mode is less pronounced in the winter, it does become defined in the summer; and thus, DLR develops two well-defined, evenly-weighted modes ($w \to 0.5$). This appears to be consistent with the hypothesis that supercooled liquid (which is more prevalent in the summer and fall; Cesana et al., 2012) may be responsible for the bimodality, but it will be demonstrated in Sect. 2.3.5 that this may not be the cause.

From these examples we may understand that the mechanism by which multimodality arises in longwave flux distributions across the Arctic is actually quite simple. In the

simplest case, with a unimodal DLR_{clr} distribution, there are two paths that the state can take: either the state remains in its current form (i.e., the scene is cloud-free or contains a cloud with $\mathrm{CRE}_{LW} \approx 0$ W/m^2), or it jumps to an opaque state with an opaque cloud of $\mathrm{CRE}_{LW} \approx 75$ W/m^2. The more distinct a region's cloud states (small variance around extremely transmissive or extremely opaque clouds), the more distinct the modes in DLR are (D becomes large). If the occurrence of cloud-free plus transmissive clouds versus opaque clouds is approximately equal, the more evenly weighted the DLR modes are ($w \to 0.5$). Importantly, the largest longwave flux values of clear-sky scenes (i.e., in the right tail of DLR_{clr}) are only around the mean of the all-sky longwave flux values, emphasizing the large radiative effect of clouds in the polar regions.

Therefore we can present two statistical ingredients necessary for distinct modes to arise in DLR distributions: small variance in the clear-sky fluxes and small variance in the transmissive and opaque cloud modes of CRE_{LW}. After satisfying these conditions, an opaque cloud mode frequency of approximately 50% leads to more evenly weighted DLR modes. Of course, multimodality can also arise through the existence of multiple DLR_{clr} modes, however, that does not seem to be the case in a majority of the distributions examined here.

Figure 2.6 depicts the density functions of DLR, DLR_{clr}, and CRE_{LW} for the three Antarctic clusters. Much like Fig. 2.5, the DLR_{clr} density functions are typically unimodal with relatively little spread. The three Antarctic clusters are essentially unique from one another, with one region that is nearly always transmissive (the Antarctic Plateau; first

row), one that is nearly always opaque (the Southern Ocean; second row) and one that has frequent occurrences of both states (the Antarctic continental boundary; third row).

Similar to the central Arctic, the Antarctic continental boundary (Fig. 2.6 third row) exhibits multiple, somewhat evenly weighted, modes in every season. This is mainly controlled by the fact that a) the variance is small in DLR_{clr} for every season, b) the frequency of the opaque cloud mode is approximately 50% in every season, and c) the opaque cloud mode is well defined (i.e., small variance).

The Antarctic Plateau (Fig. 2.6 first row) is less cloudy (approximately 50%), and clouds are infrequently opaque (a maximum of 14% in the summer). The Antarctic Plateau behaves similar to Greenland in the winter, which is unsurprising considering similar elevation, temperature, and humidity characteristics (though, this persists throughout the year for the Antarctic Plateau). Ultimately this leads to w being closer to 1 and the DLR distributions look more skewed than multimodal (and thus, smaller values of D, Tab. A.1).

Finally, the Southern Ocean region (Fig. 2.6 second row) exhibits similar behavior as that of the North Atlantic. Despite nearly always having opaque clouds (90% of scenes in the summer), two distinct modes sometimes arise due to the small variance in DLR_{clr} (though, the modes are very unequally weighted). For example, during DJF when the transmissive mode is clearly present but $w = 0.11$ (Fig. 2.4e, Tab. A.1).

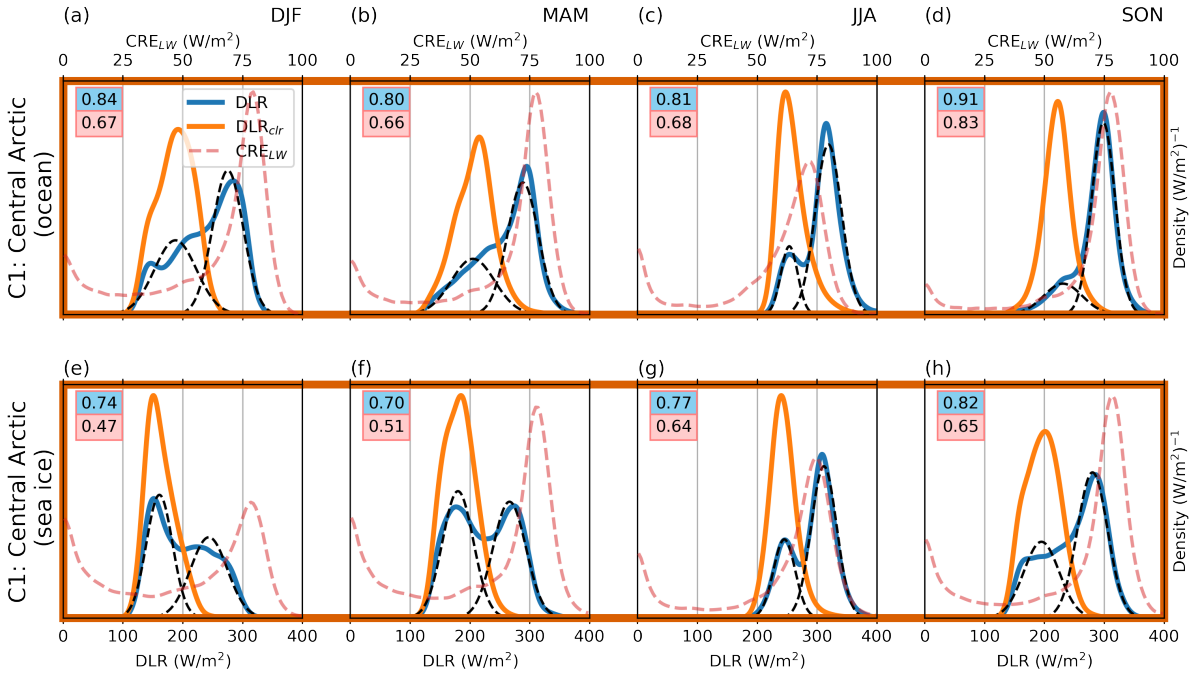

FIGURE 2.7: As Fig. 2.5 second row, but broken down by scenes which are labeled with a surface type of ocean (a-d) and a surface type of sea ice (e-h). Surface labels are extracted from 2B-FLXHR-LIDAR's 'Land_Char', a two-byte integer containing land characteristics according to The International Geosphere–Biosphere Programme (IGBP). Sea ice may be altered if the Near-real-time Ice and Snow Extent (NISE) data set provides sea ice over oceans. See the 2B-FLXHR-LIDAR technical document for a full description on how the product ingests these datasets (Henderson and L'Ecuyer, 2022). Only scenes which correspond to full sea ice or water bodies are used, partially covered sea ice scenes are not included.

2.3.4 Influence of Surface Type

A number of studies have been dedicated to understanding the connection between clouds and surface type in the Arctic, specifically in relation to phase and optical depth (characteristics closely tied to clouds' longwave effect; Schweiger et al., 2008, Morrison et al., 2018, Griesche et al., 2021). It is possible that some bimodality in CRE$_{LW}$ is due to surface type, where clouds in the opaque mode preferentially form over open water (due to increased moisture availability) and those in the transmissive mode are more likely over

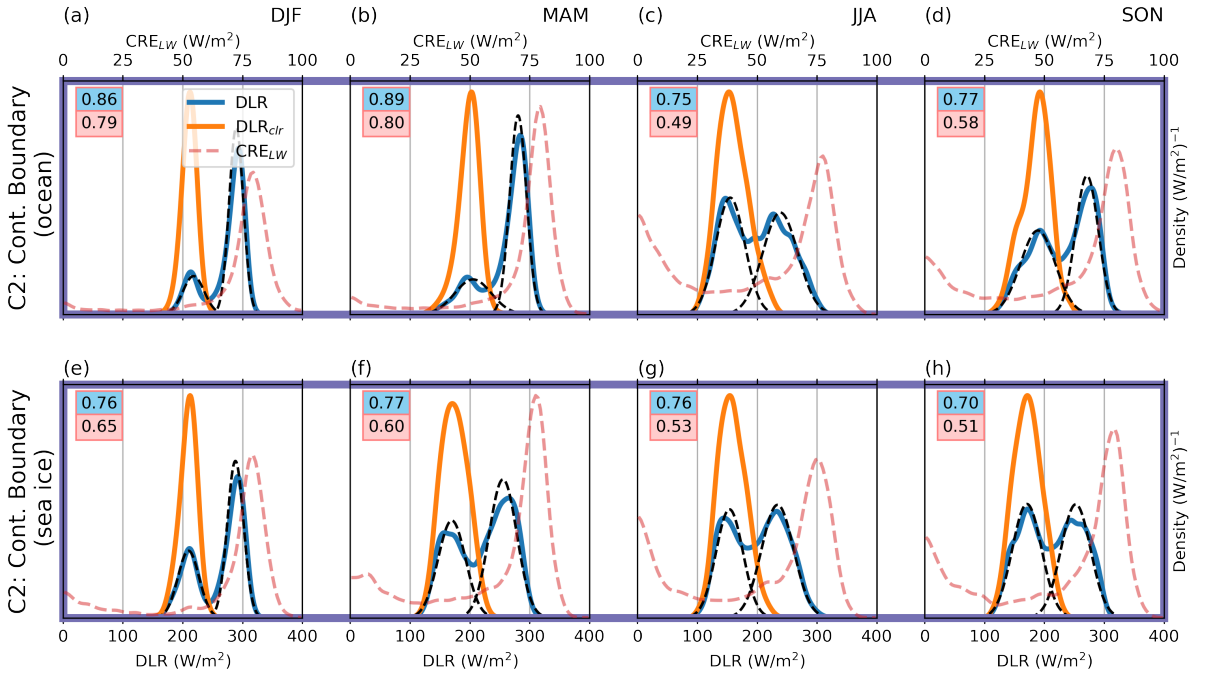

FIGURE 2.8: As Fig. 2.6 third row, but broken down by scenes which are labeled with a surface type of ocean (a-d) and a surface type of sea ice (e-h).

ice covered surfaces (Kay and Gettelman, 2009, Eirund et al., 2019). This is explored explicitly for two regions: the central Arctic and the Antarctic continental boundary. These two regions are selected for analysis since they are the most likely to contain an inhomogeneous mixture of gridboxes with either ocean or ice covered surfaces. Furthermore, this mixture varies greatly over the course of the year and from year to year, and is likely to change in a warmer climate (Stroeve et al., 2014, Stroeve and Notz, 2018, Sledd et al., 2023).

Figures 2.7 and 2.8 depict similar information as that from Figs. 2.5 and 2.6 but broken down for open water and sea ice surfaces. For both regions, indications of bimodality generally persists across all seasons for both surfaces; meaning that the occurrence of a

TABLE 2.1: The frequency of each cloud type (relative to all scenes, including cloud-free) for the CRE_{LW} density functions presented in Fig. 2.9 (left) and Fig. 2.10 (right).

Arctic Regions							**Antarctic Regions**						
	Type	DJF	MAM	JJA	SON	Annual		Type	DJF	MAM	JJA	SON	Annual
C0	Ice	28%	21%	8%	18%	19%	C0	Ice	23%	34%	38%	32%	32%
C0	Mix	21%	24%	17%	24%	22%	C0	Mix	8%	2%	1%	2%	3%
C0	Liq.	7%	14%	33%	15%	17%	C0	Liq.	1%	0%	0%	0%	0%
C0	ML	36%	31%	32%	36%	34%	C0	ML	8%	11%	18%	13%	13%
C1	Ice	31%	28%	13%	21%	23%	C1	Ice	14%	21%	28%	22%	21%
C1	Mix	10%	12%	17%	21%	15%	C1	Mix	30%	27%	16%	23%	24%
C1	Liq.	5%	11%	22%	13%	13%	C1	Liq.	21%	14%	11%	16%	15%
C1	ML	22%	20%	26%	30%	25%	C1	ML	29%	31%	32%	30%	31%
C2	Ice	38%	34 %	21%	32%	31%	C2	Ice	19%	29 %	36%	29%	28%
C2	Mix	4%	4%	14%	9%	8%	C2	Mix	21%	14%	7%	11%	13%
C2	Liq.	2%	2%	8%	4%	4%	C2	Liq.	13%	6%	2%	6%	7%
C2	ML	18%	12%	17%	18%	16%	C2	ML	20%	22%	27%	25%	24%

transmissive and opaque cloud mode is not solely driven by differing surface types within each region.

On average, sea ice covered surfaces are less cloudy and less frequently contain opaque clouds. This leads to some differences in the density functions of DLR between ocean and sea ice covered surfaces. For example, sea ice regions typically have an opaque cloud frequency of approximately 50-60%, whereas open water is closer to 60-80%; and thus, DLR modes are typically more evenly weighted in the sea ice regions. These figures also show the strong relationship between DLR_{clr} and surface type. For example, slightly higher DLR_{clr} values occur over open ocean versus sea ice. Mixing of these two surfaces helps explain the multimodal clear-sky distributions for some regions (Fig. 2.5f,h).

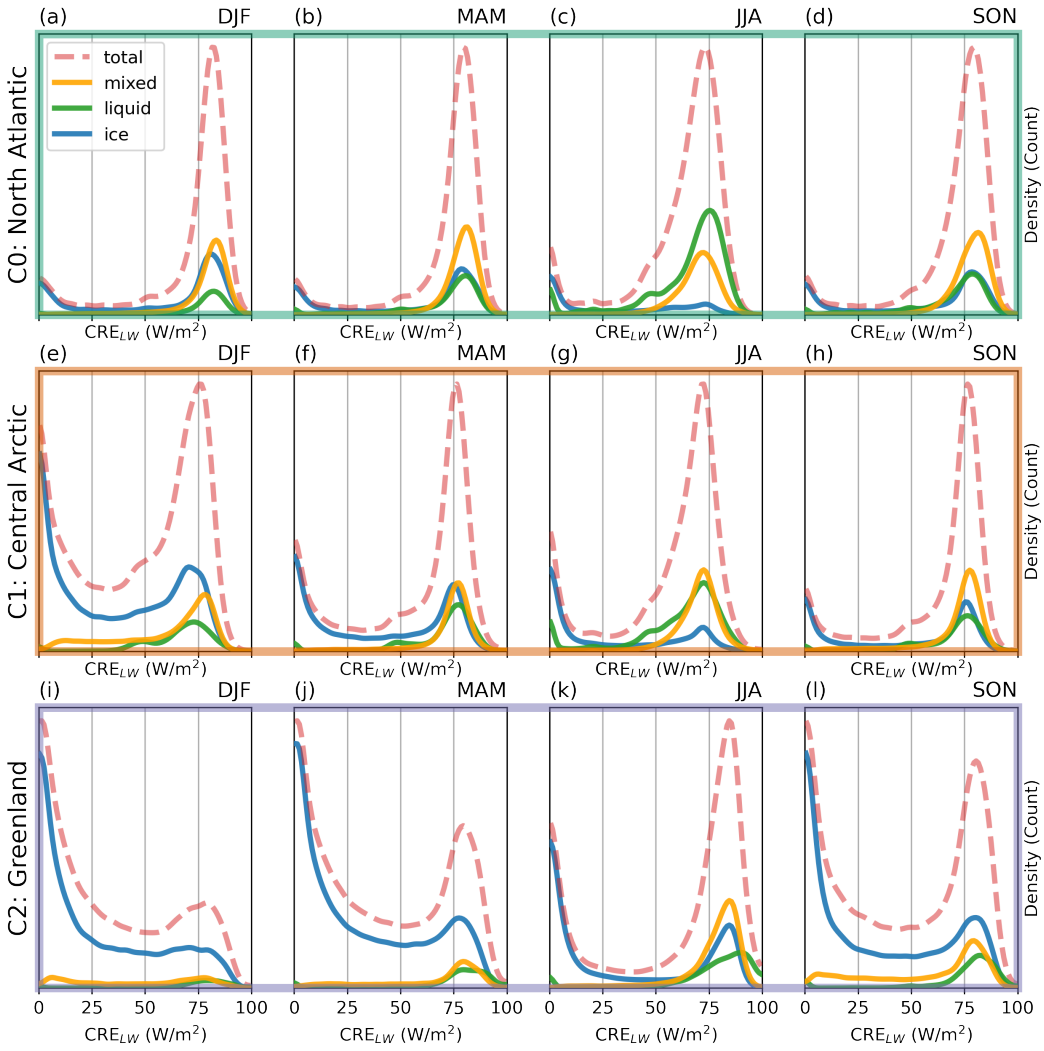

FIGURE 2.9: The CRE$_{LW}$ density functions of the formed regions in Fig. 2.3b. The red curve represents the CRE$_{LW}$ density function for all cloud types (including multi-layer), blue is for only ice clouds, orange is for only mixed-phase clouds, and green is for only liquid clouds. Density functions are scaled based on occurrence and Tab. 2.1 provides the occurrence rate of each cloud phase relative to all scenes (including cloud-free). Each row contains a different region, where boxes are colored to match with those in Fig. 2.3b. Each column depicts a different season.

2.3.5 Cloud Phase

Despite the ubiquitous nature of the two modes, it remains to be determined what type of clouds make up the opaque and transmissive CRE$_{LW}$ modes. Figure 2.9 depicts the

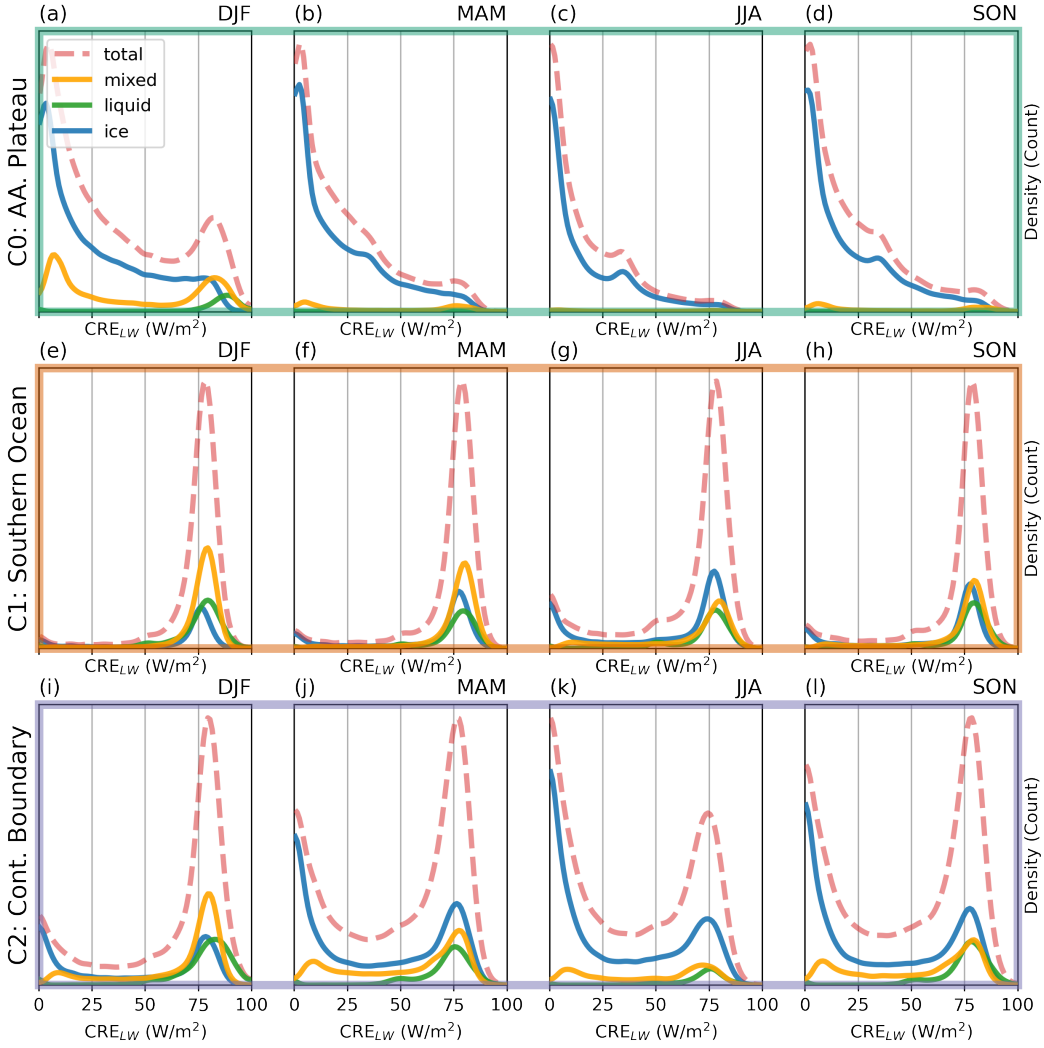

FIGURE 2.10: As Fig. 2.9 but for the Antarctic clusters.

CRE$_{LW}$ density function for each cluster, along with the CRE$_{LW}$ density functions of each particular cloud phase (multi-layer clouds are not explicitly presented but are included in the 'total' PDF, red dashed). While mixed-phase clouds are the dominant factor in controlling the 'peakiness' of the opaque CRE$_{LW}$ mode, ice clouds exhibit a similar structure as the total density function. That is, ice clouds themselves have bimodal behavior in which they either lead to a very opaque or transmissive state. This is particularly evident in the central Arctic, the North Atlantic in fall through spring, and Greenland

in spring through fall. This behavior does not seem to be well documented in previous literature, where most of the occurrences of the opaque mode are typically attributed to the presence of mixed-phase clouds (Morrison et al., 2012). As a note, while transmissive liquid-containing clouds seem somewhat frequent (especially in the North Atlantic during summer; Fig. 2.9c), their absolute occurrence is actually quite low (less than 1% of all scenes). That is, as previous studies would suggest, liquid-containing clouds nearly always lead to an opaque state.

Figure 2.10 depicts the various cloud phases that lead to the CRE_{LW} modes in each of the southern hemisphere clusters. In the Southern Ocean and continental boundary regions, ice clouds exhibit very similar behavior to those in the northern hemisphere, with a large number of occurrences in the either the transmissive CRE_{LW} mode or the opaque CRE_{LW} mode. Consistent with prior studies, mixed-phase clouds nearly always lead to the opaque cloud mode, with a peak occurrence in the summer and a minimum in the winter.

The Antarctic Plateau is typically dominated by the occurrence of ice clouds, however, during the summer season mixed-phase clouds are also frequent. Like Greenland during the winter, ice clouds over the Antarctic Plateau exhibit very little contribution to the opaque CRE_{LW} mode. The opaque CRE_{LW} mode that emerges in the summer for this region owes almost exclusively to the appearance of mixed-phase clouds. Changing occurrence rates of mixed-phase clouds over the Antarctic Plateau should certainly be kept

at the forefront of studies, since these clouds disproportionately lead to the opaque cloud mode (and thus, the largest DLR values) for this region (Adhikari et al., 2012).

2.3.6 Preferred Ice Cloud Configurations

The bimodal nature of CRE_{LW} from Arctic ice clouds suggests that these clouds develop in two preferential states, a behavior that has not been explicitly related to these states. This phenomenon is, therefore, worthy of further investigation. To understand what leads to the preferred transmissive and opaque behavior in ice clouds alone, Fig. 2.11 explores the distributions of cloud base height and cloud thickness that occur within each region. While other cloud properties (such as particle size and density) influence CRE_{LW}, cloud base height and thickness offer intuitive first order controls that CloudSat-CALIPSO can measure with greater skill (Arouf et al., 2022). The fraction of time in which each height-thickness combination leads to one of the two dominant CRE_{LW} modes (transmissive or opaque) is also presented.

Generally, all three regions have three preferential ice cloud configurations (see green arrows in Fig. 2.11b), a 'low-thick regime' (cloud base height below 1 km and thickness of approximately 5 km), a 'high-thin regime' (cloud base height above 5 km and thickness of approximately 1 km or less) and a 'low-thin regime' (cloud base height below 1 km and thickness of approximately 1 km or less. The low-thick regime overwhelmingly leads to the opaque CRE_{LW} mode and occurs frequently in the North Atlantic (Fig. 2.11d) and Southern Ocean (Fig. 2.12e). The high-thin regime is typically very transmissive, and occurs relatively frequently in the continental boundary region (Fig. 2.12c). The low-thin

regime is less frequently attributed to one mode or the other, with anywhere from 10 to 40% of the occurrences being between the two CRE_{LW} modes. Several examples of the low-thick and high-thin regime, and their associated radiative effects, are shown in Fig. A.1d (far right and middle top, respectively).

The frequencies of these three ice cloud regimes is a dominant control on whether ice clouds promote or hinder the formation of two distinct CRE_{LW} modes and they vary significantly from region to region. For example, the North Atlantic and Southern Ocean have very distinct CRE_{LW} modes (Fig. 2.9a,b,d and Fig. 2.10(e-h)). These regions are also overwhelmingly characterized by the low-thick ice cloud regime. In contrast, Greenland and the Antarctic Plateau, have smaller ice cloud CRE_{LW} modes (Fig. 2.9i and Fig. 2.10(a-d)). These regions have less distinct low-thick regimes and CRE_{LW} is often at intermediate values. This is likely due to the elevated Greenland and Antarctic ice sheets, limiting humidity and temperature values (i.e., typically even drier and colder than elsewhere at the poles), and thus, cloud longwave effects. Importantly, however, the increased frequency of (geometrically) thick ice clouds is not the only factor promoting the opaque ice cloud mode. Note that relatively thinner ice clouds near the surface more frequently lead to the opaque mode in the North Atlantic compared to the other regions (indicated by a greater span of dark red boxes in the bottom of Fig. 2.11d). Factors that may promote this behavior include increased optical thickness relative to geometric thickness, as well as interactions with the inversion level (Ettema et al., 2010).

These cloud configurations further vary as a function of season (Fig. A.4). For example,

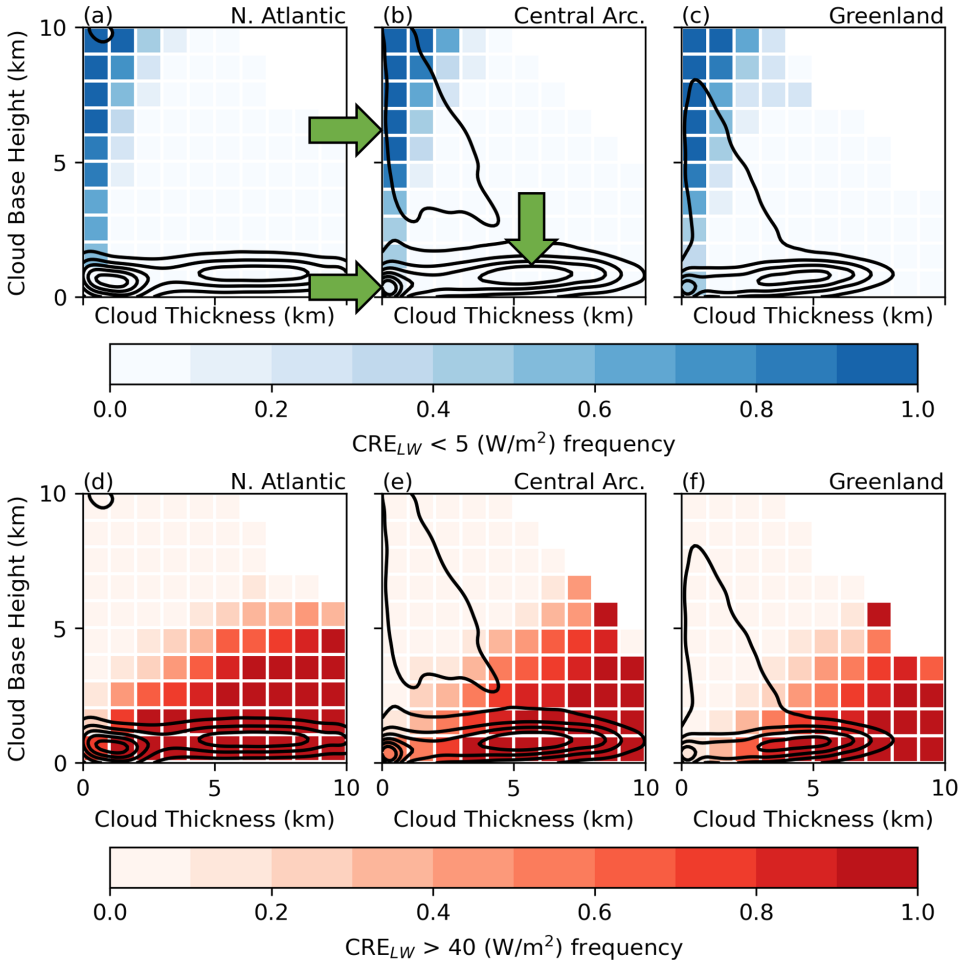

FIGURE 2.11: (a-c) A shaded contour plot depicting the frequency in which various ice cloud configurations lead to a cloud longwave effect <5 W/m^2. (d-f) A shaded contour plot depicting the frequency in which various ice cloud configurations lead to a cloud longwave effect >40 W/m^2. Contours are plotted on top showing the relative occurrence of each height-thickness configuration. The cloud base height is relative to the surface, not sea level. Green arrows are discussed in the text.

the Greenland ice cloud mode is the most distinct in the summer (Fig. 2.9k), which is connected to an increase in the relative frequency of the low-thick regime (Fig. A.4k). Furthermore, the North Atlantic has no opaque ice CRE$_{LW}$ mode during the summer (Fig. 2.9c), which is connected to a dramatic decrease in the relative occurrence of low clouds and an increase in the high-thin regime (Fig. A.4c).

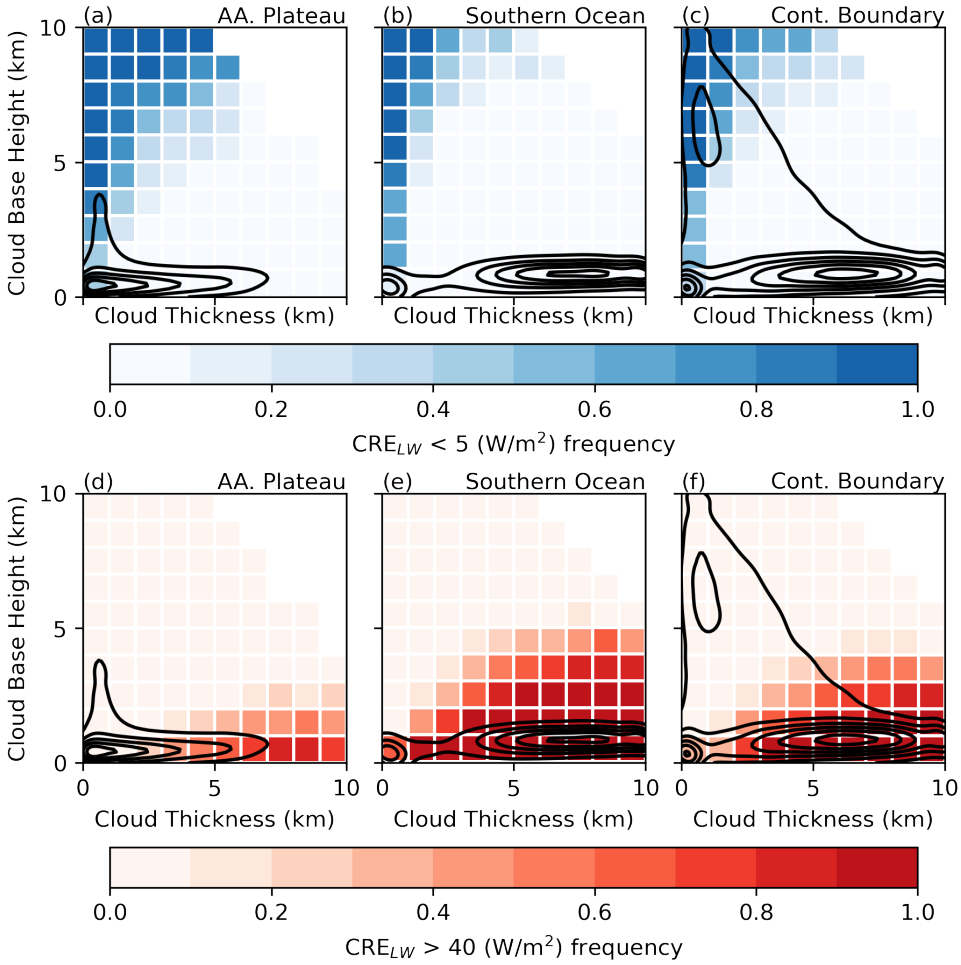

FIGURE 2.12: As Fig. 2.11 but for the Antarctic clusters.

Each of these ice cloud regimes may be attributed to a general cloud type or process leading to them. For example, the low-thick regime likely represents synoptic disturbances which can transport moisture into the entirety of the column, leading to very thick clouds. The high-thin regime most likely represents cirrus clouds. The processes leading to the low-thin regime may be more variable, however, part of these occurrences could represent recently glaciated mixed-phase clouds.

Further investigation is required to better understand the processes leading to each ice

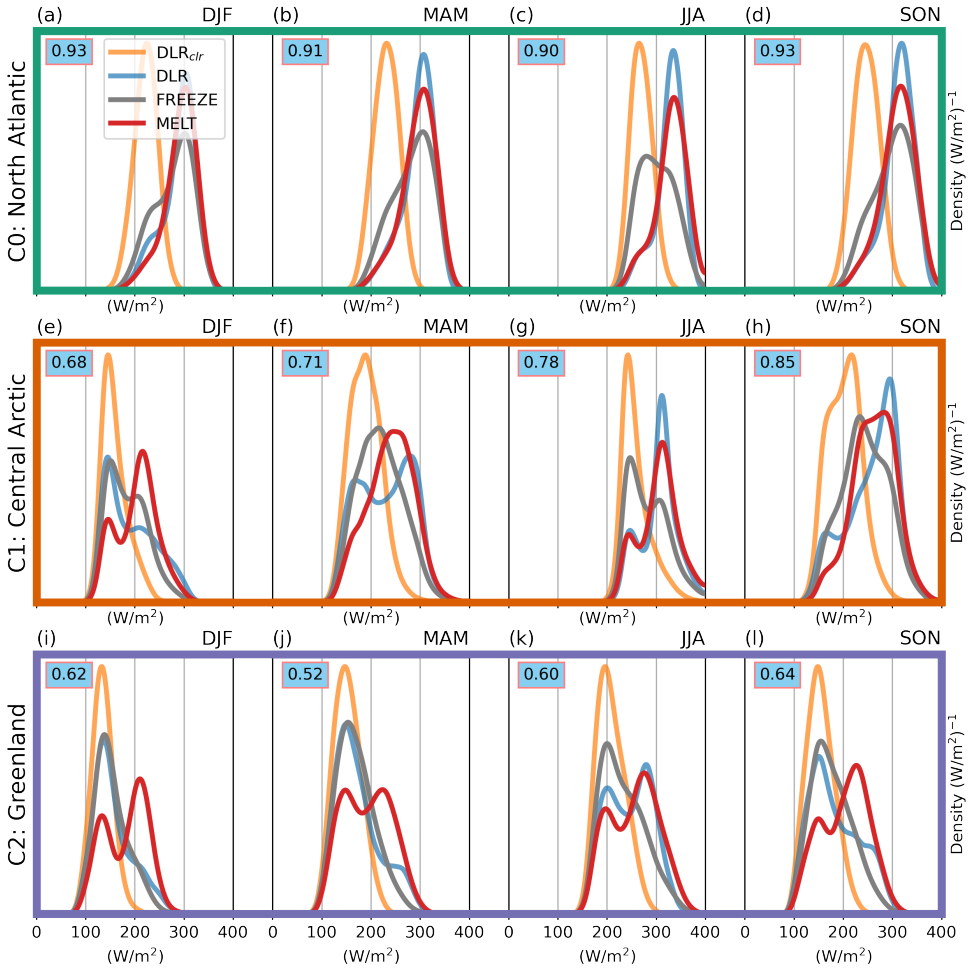

FIGURE 2.13: The DLR and DLR$_{clr}$ density functions of the formed regions in Fig. 2.3b. Orange represents the density functions of the clear-sky DLR distribution (DLR$_{clr}$), blue is the true DLR distribution, red is only sampling CRE$_{LW}$ from liquid clouds and grey is only sampling CRE$_{LW}$ from ice clouds. Each row contains a different region, where boxes are colored to match with those in Fig. 2.3b. Each column represents a different season. For each panel, the sampled frequency of clouds is listed in blue.

cloud regime, but these findings emphasize the importance that non-liquid containing clouds have in defining the preferred atmospheric radiative states in the Arctic and parts of the Antarctic.

TABLE 2.2: Mean (standard deviation) of each distribution plotted in Fig. 2.13

	(W/m^2)	DJF	MAM	JJA	SON	Annual
C0	DLR_{clr}	221 (24)	230 (25)	270 (22)	247 (26)	243 (30)
C0	DLR	287 (37)	294 (35)	326 (29)	311 (33)	305 (37)
C0	FREEZE	276 (41)	283 (42)	302 (37)	300 (42)	294 (45)
C0	MELT	290 (35)	295 (37)	329 (34)	310 (36)	306 (40)
C1	DLR_{clr}	159 (26)	190 (32)	259 (30)	203 (34)	205 (48)
C1	DLR	193 (50)	231 (54)	305 (38)	257 (52)	248 (63)
C1	FREEZE	186 (39)	220 (46)	285 (42)	244 (48)	236 (57)
C1	MELT	204 (42)	239 (47)	307 (43)	262 (45)	254 (58)
C2	DLR_{clr}	135 (21)	153 (27)	209 (28)	155 (28)	164 (38)
C2	DLR	157 (40)	175 (46)	247 (45)	185 (51)	192 (57)
C2	FREEZE	154 (34)	171 (38)	233 (44)	178 (41)	185 (48)
C2	MELT	182 (44)	192 (49)	256 (50)	204 (48)	210 (56)

2.4 Impact of Changing Cloud Phase

We now present a simple sensitivity study to explore how artificial changes in each cloud type affects the modality of longwave flux distributions. This may be useful for understanding the impact that misrepresentation of cloud phase has on climate models as well as assessing the impact of cloud phase changes on future climate. Since DLR = DLR_{clr} + CRE_{LW}, we can produce simple hypothetical scenarios of DLR where, only CRE_{LW} corresponding to ice clouds ('FREEZE') or liquid clouds ('MELT') are sampled to generate DLR distributions (Fig. 2.13, Tab. 2.2). Explicitly, for each Arctic region, DLR_{clr} and cloud frequency mirrors those presented in Fig. 2.5, but CRE_{LW} values from only the ice clouds (Fig. 2.9 blue) or liquid clouds (Fig. 2.9 green) are sampled to produce an DLR distribution. Note that clouds are not directly converted to ice or liquid, but rather, present-day ice clouds are oversampled (comprising 100% of clouds in the case of

'FREEZE') or present-day liquid clouds are oversampled (comprising 100% of clouds in the case of 'MELT').

In some cases, multimodality vanishes if all clouds are converted to liquid or ice (for example, Fig. 2.13f,h) and in other cases, it artificially arises (for example, Fig. 2.13i,j,l). Similarly, in some regions the difference between an all-frozen versus all-melted scenario is significant, for example, Greenland winter (Fig. 2.13i). However, in other cases, melting or freezing all clouds leads to relatively similar distributions, for example, central Arctic spring (Fig. 2.13f, though both are very different than the true distribution).

While these are extreme examples, it becomes evident that misrepresenting cloud processes can mask or artificially exhibit important climate shifts that may manifest themselves in the cloud radiative states. As seen with the regions presented here, some areas will be impacted to a greater degree than others by these misrepresentations. Furthermore, simply representing these distributions with their mean and variance does not necessarily capture the subtleties of the radiative distributions. For example, the mean of DLR in the central Arctic spring is 231 W/m^2 and is characterized by a relatively large variance of 54 W/m^2 (Tab. 2.2). This a) does not capture the fact that there is relatively small variance around two different states and b) incorrectly presents that the most likely state is where there is a local minimum in the true probability (i.e., between the two modes). As others have previously suggested, correctly modeling the *distribution* of longwave fluxes in the Arctic (rather than just the mean and variance) is critical for

accurately evaluating the state of climate models (Raddatz et al., 2015). The present findings certainly emphasize this idea.

2.5 Conclusions

This study explores the properties of surface longwave flux distributions across the northern and southern hemispheric polar regions. While previous studies have identified the presence of 'radiative regimes' stemming from Arctic field campaigns, this has yet to be explored systematically across the full extent of both poles. Taking advantage of the vast polar sampling capabilities provided by multiple years of CloudSat and CALIPSO, this work demonstrates that transmissive and opaque radiative states are nearly ubiquitous across the Arctic and low elevation perimeter around Antarctica. These findings are robust irrespective of the aggregation scale (i.e., Fig. A.1 and A.3 behave similarly to Fig. 2.5).

While previous studies (e.g., Stramler et al., 2011b, Engström et al., 2014, Solomon et al., 2023) are correct in the assumption that these states arise due to the presence of opaque clouds, evidence is provided here that a) the opaque state is not solely attributed to liquid-containing clouds and b) these states exist in the southern hemisphere polar region. Despite bimodality not explicitly manifesting in some regions (for example, the North Atlantic or the Southern Ocean), similar cloud states exist throughout the polar domain.

The fact that this bimodal behavior can arise without the presence of liquid-containing clouds has not been widely characterized in previous studies. It is found that ice clouds

seem to have preferential modes themselves– either leading to a very transmissive or opaque state. This behavior is controlled by preferred cloud base height and cloud thickness configurations. The frequency in which these preferred ice cloud configurations occur vary significantly for each region, which has a dominant role in shaping the distinctness of the DLR modes. The processes which contribute to the formation of the opaque cloud mode *from ice clouds* (i.e., thick, synoptic formations) are likely different than those processes which lead to the presence of relatively thin low-level liquid-containing clouds (perhaps more local processes).

A simple conceptual model is presented which shows how multimodality versus skew versus translation can arise in DLR distributions. This simple model may allow for a greater understanding of how these radiative states will change in the future (by tuning the cloud frequency, shifting the clear-sky distribution, etc.). For example, a simple experiment is conducted which shows what effects the misrepresentation (or alternatively, the changing frequency in a changing climate) of cloud phase has on the longwave flux distributions for several Arctic regions. In some regions, multimodality disappears and in others it artificially manifests. Climate models should continue to address the important issue of appropriately representing cloud phase to understand how longwave flux distributions will change in the future. Furthermore, one should pay attention to the higher moments of these distributions rather than assuming unimodality, even within a single season and region. In some cases, the mean and variance imply relatively large variance around a central state; however, in reality, there is relatively little variance around two preferred states. With a rapidly changing Arctic, this has implications if one of these two modes

can only arise under certain environmental conditions. Similar conclusions could also apply to the area surrounding the Antarctic continent.

There are several questions that naturally arise from this analysis. In this study we mainly consider the effects that clouds have on the longwave flux towards the surface, however, what are their characteristics in the shortwave or at the top of atmosphere? In essence, the longwave effect at the surface saturates in such a way that a very thick ice cloud has the same longwave effect as a thin mixed-phase cloud (Persson et al., 2017); however, these two clouds will have very different radiative effects in the shortwave and at the top of atmosphere. For completeness, we have provided tables of the mean and variance of the outgoing longwave radiation (OLR; Tab. A.2), the shortwave flux towards the surface (FSDS; Tab. A.3), and the outgoing shortwave radiation (OSR; Tab A.4) for the same scenarios presented in Sect. 4 (i.e., an identical DLR_{clr} distribution but sampling cloud radiative effects from only liquid or ice clouds). Linking these states with their shortwave (and top of atmosphere) components is important for an understanding of their effect on the net surface energy budget. However, in order to remain focused on how these longwave states express themselves at the surface, we choose to not discuss these other radiative components further.

Continuing to characterize the environmental characteristics that promote or hinder the formation of these two states may allow one to understand how their frequency (and properties) will change in the future. Arctic-targeted field campaigns such as MOSAiC (Shupe et al., 2020) allow one to take a deep dive into specific processes of interest,

including the influence of leads and aerosols on clouds. Understanding how airmasses affect the evolution of the local climate (in the present and future) should remain of key interest (Tjernström et al., 2019, Nygård et al., 2020); parcel tracking approaches allow one to trace the origins of airmasses, disentangling the influence of local versus remote drivers of the states (Papritz et al., 2022). Finally, future spaceborne missions that will extend the active satellite data record (such as EarthCare; Wehr et al., 2023) are of vital importance for continuing to uncover the secrets of the data-sparse high latitudes and providing a continued record of these radiative states in the coming years.

Chapter 3

Under-Representation of Ubiquitous Opaque and Transmissive Arctic Atmospheric States in Modern Reanalyses*

*This is a lightly modified version of: Bertossa, C., L'Ecuyer, T., Henderson, D., and E. McIlhattan. "Under-Representation of Ubiquitous Opaque and Transmissive Arctic Atmospheric States in Modern Reanalyses." Journal of Climate (in review).

3.1 Preface

Given the sparse and relatively new observational network in the Arctic, researchers rely heavily on models, both forecasts and reanalyses, to understand the past, present, and future climate of the region (Felzer and Thompson, 2001, Kay et al., 2012, Berger et al., 2013, Morrison et al., 2019). However, due to the scarcity of observations, modeling Arctic climate presents unique challenges. In reanalyses, for example, limited observations necessitate a greater reliance on models to initialize the complete atmospheric and oceanic state. Moreover, the paucity of observations complicates model evaluation efforts. Consequently, significant attention is directed towards not only assessing model performance but also refining evaluation practices (Ebert et al., 2013). Common evaluation methods involve comparing the mean and variance of geophysical parameter distributions with observations or employing standard skill scoring metrics (Reichler and Kim, 2008, Vannitsem et al., 2018). However, many of these methods (explicitly or implicitly) assume unimodal distributions (e.g., Gaussian). Thus, their usefulness breaks down in the presence of multimodality and can even actively degrade model skill when deriving bias corrections (Bertossa et al., 2021).

The previous chapter has also shown that bimodality is prominent in observed polar longwave flux distributions, including net longwave radiation at the surface (NET_{LW}, Stramler et al., 2011a), downwelling longwave radiation at the surface (DLR, Engström et al., 2014), and surface longwave cloud radiative effect (CRE_{LW}, Arouf et al., 2024). Furthermore, Raddatz et al. (2015) establishes that DLR is representative of several

other Arctic geophysical variables (including temperature, humidity, pressure, and cloud occurrence), explicitly demonstrated by density functions of 2-meter temperature, which also exhibit bimodality (Graham et al., 2017).

While the prevalence of bimodal behavior in polar regions may pose a challenge for conventional validation approaches, this complexity can be reframed as advantageous. Considering the robust correlation between DLR and other geophysical variables in the Arctic, evidence of precise modeling of DLR behavior may be indicative of potential model skill for numerous other variables. Thus, conducting a thorough examination of DLR distributions in comparison to observational data offers an efficient means of evaluating models' proficiency in capturing the complexities of the Arctic climate system, helping address the difficult issue of evaluating models in data-sparse regions. Given their notable impact on DLR, and thus the surface energy balance, examining the representation of the two recurring radiative states in models is a critical step in this evaluation process.

Accurately capturing the frequencies of these two radiative states requires a comprehensive representation of diverse cloud formation and evolution processes occurring across various scales. However, as shown in the previous chapter, rather than focusing on evaluating these complex underlying processes, considerable insight can also be gained by analyzing the modes' emergence from a statistical perspective. For example, we have shown that distinct modes in DLR distributions are driven by small variability in clear-sky fluxes and the presence of both a transmissive (approximately 0 W/m^2) and opaque

cloud mode (approximately 75 W/m^2) in CRE$_{LW}$. The interaction between these components shapes the surface longwave flux distribution and determines the relative frequency of each mode in DLR. The frequency of the opaque cloud mode in CRE$_{LW}$ governs the frequency of the larger DLR mode.

Several studies have examined how these states are represented in models (Cesana et al., 2012, Engström et al., 2014, Graham et al., 2017, 2019, Solomon et al., 2023). However, these typically examined a localized region or a single year. Leveraging the pan-polar observations offered by polar orbiting satellites, this chapter evaluates the ability of several reanalysis products in simulating Arctic DLR distributions. Special interest is taken in those regions which exhibit distinct bimodality in observed DLR distributions, indicating the presence of two preferred states. Moreover, the main factors leading to the two observed Arctic CRE$_{LW}$ modes are analyzed. By examining reanalyses with different resolutions and degrees of specificity towards polar processes, this investigation sheds light on how model resolution and complexity influences the representation of these states.

3.2 Data and Methods

3.2.1 CloudSat and CALIPSO

This study uses the synergistic measurements offered by CloudSat and Cloud-Aerosol Lidar and Infrared Pathfinder Satellite Observation (CALIPSO) (Stephens et al., 2002) to identify regions and time periods where bimodality is evident in DLR. CloudSat and

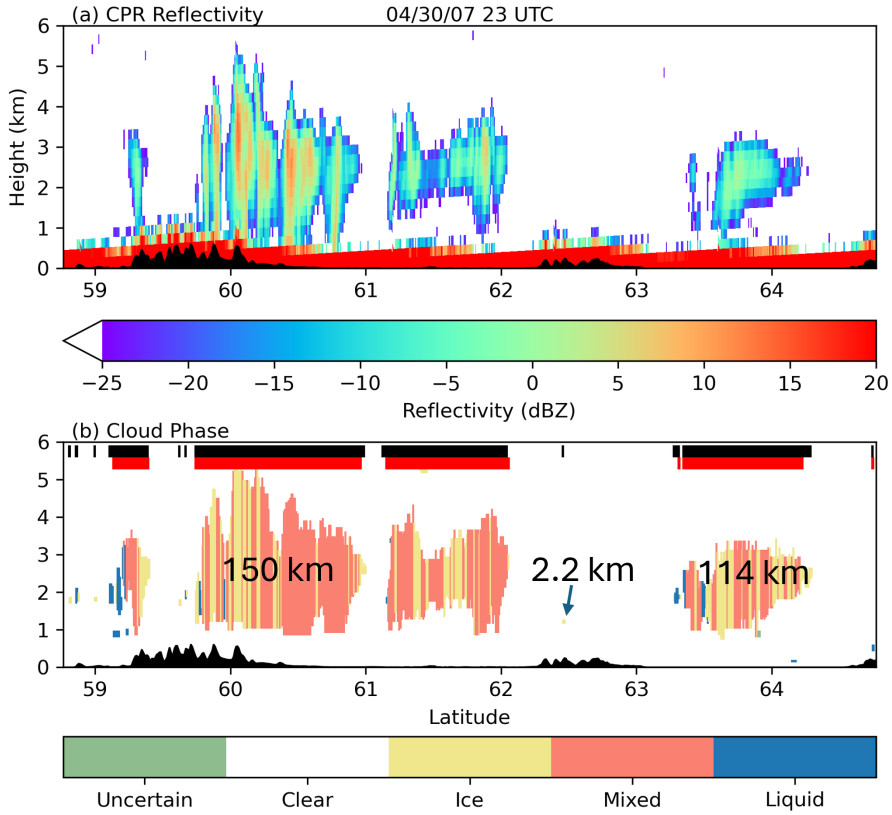

FIGURE 3.1: Example swath cross-section over western Alaska on April 30th 2007 depicting latitude on the x-axis and height on the y-axis, derived from CloudSat-CALIPSO data. (a) Shows reflectivity values obtained from CloudSat's CPR. (b) Displays cloud phase information determined by 2B-CLDCLASS-LIDAR. Black lines at the top represent a binary cloud mask. Red lines at the top indicate scenes in which the CRE_{LW} >40 W/m^2 (defined as an 'opaque cloud', see text) derived from 2B-FLXHR-LIDAR. Several example cloud chord lengths (i.e., horizontal extent, see text) are overlaid.

CALIPSO allow for effective mapping of cloud vertical structure, including phase, precipitation type, and radiative fluxes, from 82°S to 82°N through the combination of CloudSat's cloud profiling radar (CPR) and CALIPSO's lidar. A brief description of the joint CloudSat-CALIPSO products leveraged in this study are given here. CloudSat-CALIPSO products are mapped onto CloudSat footprints, whose size is approximately 1.4 km across-track by 1.8 km along-track sampled at a 1.1 km along-track interval.

The 2B-CLDCLASS-LIDAR product (Sassen et al., 2008) allows for reliable cloud phase detection for up to 10 cloud layers for each scene. This is done independent of underlying surface conditions that often complicate passive sensor retrievals in the polar regions (Liu et al., 2010). Cloud phase is effectively determined using the different sensitivities of the radar and lidar to liquid droplets (Wang et al., 2013) and the product has been developed and refined using ground-based observations.

The 2B-FLXHR-LIDAR product (Henderson et al., 2013) models the radiative flux (longwave and shortwave) for each 240-meter height bin sampled by the CPR from the surface to 20 kilometers. To perform these calculations, the algorithm uses a combination of atmospheric state variables obtained from AN-ECMWF reanalysis data, profiles of cloud ice and liquid water content obtained from the CloudSat 2B-CWC-RO and 2C-ICE products, and derived surface albedos (Henderson and L'Ecuyer, 2022). As in Ch. 2, this study examines atmospheric radiative states through the context of downwelling longwave radiation at the surface (DLR), the clear-sky downwelling longwave radiation at the surface (DLR_{clr}), and the cloud radiative effect at the surface, defined as CRE_{LW}=DLR-DLR_{clr}. By focusing on the downward component of longwave radiation, we help remove the impact of surface albedo assumptions and the additional complications resulting from variable solar zenith angle.

Despite being spaceborne instruments, previous studies have found that CloudSat and CALIPSO are able to effectively estimate radiation at the surface (e.g., Protat et al., 2014, Van Tricht et al., 2016, Blanchard et al., 2021, Arouf et al., 2022). For example,

(Liu, 2022) finds that the combination product can sample even low clouds with relatively high skill, especially those above 1 km. While CloudSat and CALIPSO may not capture the precise location of the cloud base below 1 km, the radiative influence of extending the cloud base into the obscured zone near the surface is minimal (approximately 1.5 W/m^2 per 250 meters; Henderson et al., 2013), far smaller than the distinction between the two radiative modes (approximately 80 W/m^2).

Moreover, Bertossa and L'Ecuyer (2024) and McIlhattan et al. (2017) find that 2B-FLXHR-LIDAR produces similar radiative fluxes as ground-based observations at the North Slope of Alaska and Summit Station, Greenland, respectively. Furthermore, twice daily sampling (approximately 1:30 AM and PM local time) can capture the diurnal cycle of mixed phase clouds over the Southern Ocean (Hinkelman and Marchand, 2020).

Figure 3.1 illustrates CloudSat-CALIPSO products for a selected Arctic swath over western Alaska. Here, several semi-homogeneous cloud formations are evident, featuring a blend of liquid-only, ice-only, and mixed-phase clouds. Note that CLDCLASS-LIDAR (Fig. 3.1b) has clouds detected by CALIPSO that the CPR alone (Fig. 3.1a) does not show. As expected, the liquid-containing clouds exert a large longwave effect as evident by the extensive span of 'opaque' sections (red dashes at the top of Fig. 3.1b).

Due to a CloudSat battery anomaly that occurred in 2011, observations beyond this point are limited to daytime only. To capture complete seasonal variations in polar regions, our analysis is limited to only those observations which took place from 2007 through 2010 (four years), prior to the anomaly.

3.2.2 Reanalyses

Three reanalyses are evaluated in this study: The second version of the Modern-Era Retrospective Analysis for Research and Applications (MERRA2; Gelaro et al., 2017), The European Centre for Medium-range Weather Forecasts Reanalysis 5 (ERA5; Hersbach et al., 2020), and the second version of the Arctic System Reanalysis (ASR; Bromwich et al., 2018). These three products are chosen since they are commonly used in weather and climate studies, globally and in the Arctic specifically (e.g., Yeo et al., 2022, Graham et al., 2019, Herrmannsdörfer et al., 2023, Bromwich et al., 2009). A brief description of each product is provided here.

MERRA2 is a global reanalysis product produced by NASA's Global Modeling and Assimilation Office (GMAO). The model has a horizontal resolution of 0.625° longitude by 0.5° latitude, with 72 hybrid sigma-pressure vertical model levels up to 0.01 hPa and is produced hourly; vertical spacing is smaller closer to the surface (nominal 15 hPa). MERRA2 was designed to improve upon version 1, namely, incorporating new satellite observations, including aerosol data assimilation, improving aspects of the cryosphere and stratosphere, and addressing biases and imbalances in certain atmospheric and land surface hydrological quantities (Gelaro et al., 2017).

ERA5 replaces the widely used ERA-Interim (Dee et al., 2011). ERA5 has global coverage, with a horizontal resolution of 0.25° longitude by 0.25° latitude. ERA5 resolves the atmosphere using 137 vertical levels from the surface up to a height of 0.01 hPa. It

provides hourly analysis and forecast fields. Evaluations of ERA5 have revealed better performance compared to ERA-Interim in, for example, surface irradiance biases, summer warm biases, and precipitation biases (Albergel et al., 2018, Urraca et al., 2018, Wang et al., 2019). Both ERA-Interim and ERA5 have frequently been used for studying changes in the Arctic and forcing ocean and sea ice models (Woods and Caballero, 2016, Graham et al., 2017, Jenkins and Dai, 2022, Pascual-Ahuir and Wang, 2023). Enhanced resolution (spatially and vertically) compared to MERRA2 may lead to more skillful parameterizations of cloud processes.

ASR is an Arctic-specific reanalysis dataset designed to more accurately represent polar processes. ASR leverages the polar version of the Weather Research and Forecasting (WRF) Model (commonly referred to as Polar WRF; Hines and Bromwich, 2008), producing 3-hourly output for 34 pressure levels (71 model levels) at a 15-km horizontal resolution. The lowest full model level is 4-m above ground level, with over 25 levels below 850 hPa. Increased vertical resolution near the surface in ASR may allow for better representations of low-altitude cloud-surface interactions. The inner domain of ASR covers approximately 50% of the northern hemisphere, with lateral boundary conditions provided by ERA Interim. ASR uses subgrid-scale representations of sea ice (including fractional sea ice within each gridbox, which have concentration, thickness, and albedo characteristics), as well as subgrid-scale cloud fraction interaction with radiation (allowing for more realistic representation of shortwave and longwave radiation; Alapaty et al., 2012).

3.3 Observed and Simulated DLR Distributions

To understand if reanalyses are skillful in capturing the longwave flux distributions found in the polar regions, it is necessary to ensure that the comparisons to observations are equivalent spatially and temporally.

3.3.1 Influence of Sampling Time

Figure B.1 in Appendix B demonstrates that each reanalysis product's PDFs are virtually identical whether they are limited to just the local times of 1:00 AM/PM (approximately aligning with the 1:30 AM/PM CloudSat and CALIPSO sampling times) or include all times of day provided by the reanalysis product (hourly for ERA5 and MERRA2, 3-hourly for ASR). A similar result is obtained if physically smaller regions or seasonal data are used to derive the PDFs (not shown). Hence, it can be concluded with some confidence that the sampling time of CloudSat and CALIPSO does not artificially produce the exhibited bimodality. Therefore, we do not limit the reanalysis products to the CloudSat and CALIPSO sampling times, and hereinafter, the full set of times provided by each product are used to allow for increased sample sizes. Furthermore, we test the impact of sampling density on the derived PDFs, where, the higher latitudes are sampled more densely by CloudSat and CALIPSO than the lower latitudes. Generating PDFs of DLR using weighted gridboxes (based on sampling frequency) versus unweighted gridboxes results in essentially identical distributions, and thus we conclude this is also not influencing the presented results.

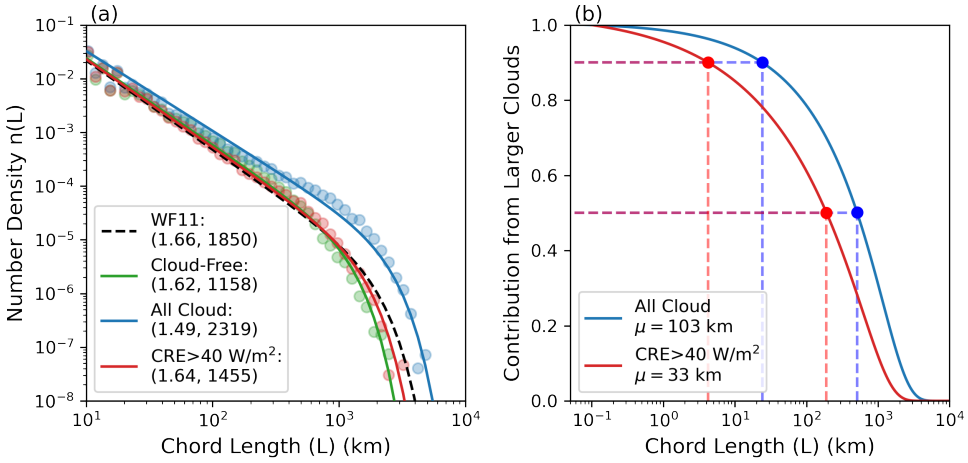

FIGURE 3.2: (a) Arctic cloud chord length distributions derived from CloudSat-CALIPSO data following the methodology of Wood and Field (2011) (WF11). Chord lengths of all Arctic clouds (blue), Arctic clouds which have a CRE_{LW} >40 W/m^2 (red) and Arctic cloud-free (green) scenes are included. The global chord length distribution derived in WF11 is also provided for reference (black dashed). Each distribution is fit with a power law distribution with the form of Eq. 3.1. The legend lists the β and L_* fit to each distribution (see text). (b) Contribution of cloud chord length to total Arctic cloud cover. The 90% and 50% lines have been highlighted (dashed) and the mean chord lengths are provided (legend).

3.3.2 Spatial Scales of Radiative States

Native CloudSat-CALIPSO footprints are able to resolve relatively small scale features whereas models lie on a regular grid representing larger areas: 35 km x 56 km at 60 degrees (12 km x 56 km at 80 degrees) for MERRA2, 14 km x 28 km at 60 degrees (5 km x 28 km at 80 degrees) for ERA5, and a uniform 15 km x 15 km grid for ASR. It is thus natural to wonder whether models can detect the same features as these observations. To address this we present a concise examination of polar clouds' spatial scales. While this can be partially understood by considering the governing processes, it can be explicitly estimated through observations.

We rely on the relatively simple methodology of Wood and Field (2011) and Guillaume et al. (2018) to characterize the spatial scales of clouds. A cloud is represented by its chord length, L, which is calculated from the number of continuous along-track scenes in which the joint CloudSat-CALIPSO cloud mask identifies a cloud, multiplied by the along-track sampling frequency (1.1 km). These chord lengths can then be used to derive a chord length distribution, $n(L)$, to approximate a size distribution of clouds. While this is a horizontally one-dimensional estimate of size, $n(L)$ derived from the MODerate Resolution Imaging Spectroradiometer (MODIS) are found to be identical between the across-track and along-track direction, meaning that these distributions may be horizontally isotropic (Wood and Field, 2011, Guillaume et al., 2018). Wood and Field (2011) find a power law of the form

$$n(L) \sim L^{-\beta} \exp\left[-\left(L/L_*\right)^2\right] \tag{3.1}$$

to be well representative of global n(L) distributions. β determines whether smaller versus larger clouds dominate total cloud cover. As β becomes smaller than 2, large clouds (order of 100 km or larger) contribute a greater proportion to cloud cover; as β becomes larger than 2, smaller clouds (order of 10 km or smaller) contribute a greater proportion to cloud cover. L_* represents a scale break, after which the power law relationship no longer applies. As L_* increases, the power law relationship is valid over a larger range of scales. See Fig. 3.2a (black dashed) for a globally derived density distribution from Wood and Field (2011).

Here we perform a similar analysis limited to poleward of 60 ^{o}N, finding: continuous stretches of clouds (for example, black bars in Fig. 3.1b), continuous stretches of clouds whose CRE_{LW} is at least 40 W/m^2 (for example, red bars in Fig. 3.1b, denoting opaque cloud occurrences), and continuous stretches of cloud-free conditions (for example, no bars in Fig. 3.1b). Distributions of these chord lengths are then created and compared to the global characterization derived in Wood and Field (2011) (Fig. 3.2a).

On average, Arctic cloud chord lengths are 100 km and n(L) has a β smaller than the global distribution, meaning large clouds have higher relative frequency in the Arctic versus the global average (blue in Fig. 3.2). Including a CRE_{LW} restriction of 40 W/m^2 reduces the mean chord length to 33 km, which is similar to the average cloud-free chord length. Figure 3.2b further contextualizes these findings, showing that nearly 90% (50%) of total cloud cover is attributed to cloud chord lengths of 25 (500) km or larger, and 90% (50%) of the total *opaque* cloud cover is due to chord lengths of 4 (200) km or larger. While some of these opaque cloud features may be smaller than a model grid box and thus not explicitly resolved, a large portion (i.e., likely more than 50%) should be adequately represented. This generally aligns with the idea that Arctic cloud states are largely influenced by synoptic scale dynamics (Morrison et al., 2012, Pithan et al., 2018).

3.3.3 Annual DLR Representation

In order to compare DLR distributions, all datasets have been grouped onto a common 6° × 3° (longitude-by-latitude) grid (Figure 3.3). Distributions for CloudSat-CALIPSO, ERA5, MERRA2 and ASR are provided. Selected DLR distributions derived from this

grid are provided (Fig. 3.3a-d). Note that the native resolution of each product is not modified. For example, since ASR has a higher spatial resolution, more samples will be included in each $6^\circ \times 3^\circ$ gridbox than a lower resolution product like MERRA2. For each reanalysis product we also provide the amount of 'overlap' with that of native CloudSat-CALIPSO observations. The overlap of two distributions is defined mathematically as $\sum_{x=1}^{n} \mathbf{min}(\vec{p}, \vec{q})\ dx$, where $\vec{p}$ and $\vec{q}$ are two PDFs estimated with n bins of bin width dx. This overlap percentage represents the amount of shared area between two distributions, where 100 indicates identical distributions. Furthermore, to explicitly understand the effect of spatial inhomogeneity on the derived DLR PDFs, CloudSat-CALIPSO density functions are recalculated using consecutive 30-footprint averages ($\approx$ 33 km chord length; Fig. 3.3a). 33 km aligns with the approximate average spatial scale of these states in Fig. 3.2, and exceeds one or both of the horizontal dimensions in the majority of reanalysis gridboxes.

Figures 3.3(e-h) show spatial maps of the overlap percentage compared to native CloudSat-CALIPSO footprints for each Arctic gridbox. Aggregating 30 footprints results in minimal changes to the derived DLR PDFs, with 95-100% matches between the coarsened and native resolution distributions across most gridboxes (Fig. 3.3e). That being said, there are spatially coherent regions with reduced overlap, such as the North Atlantic and the land areas around the Bering Strait.

MERRA2 tends to exhibit less agreement with observations compared to ERA5 and ASR throughout the domain. ERA5 and ASR are similar in their alignment with observations,

though there is some regional variation. For instance, ASR outperforms ERA5 in the North Atlantic storm track region (green dot area) but slightly underperforms in much of the Arctic Ocean (e.g., red dot area).

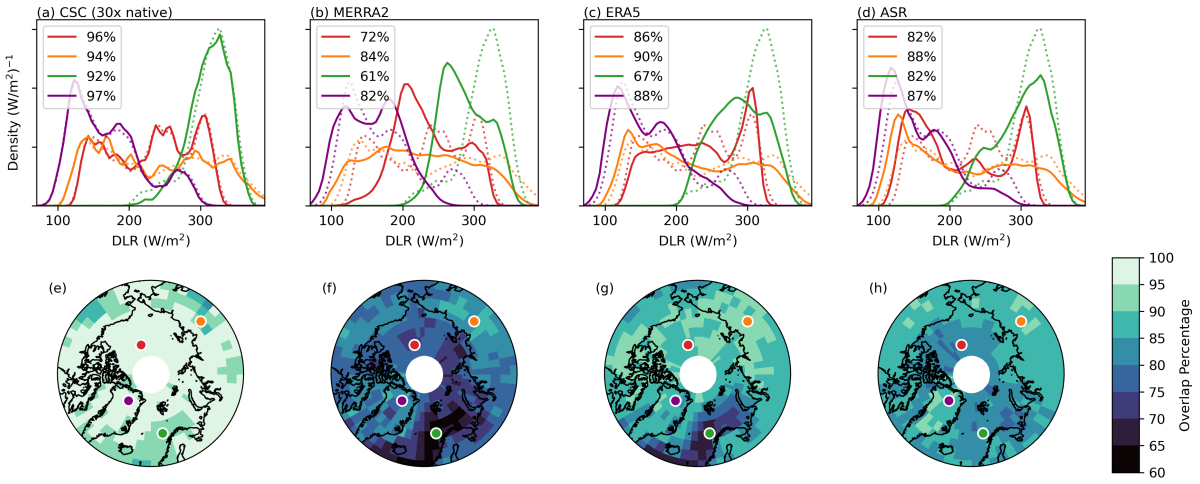

FIGURE 3.3: (a-d) DLR PDFs for four selected 6° × 3° gridboxes in the Arctic derived from coarsened CloudSat-CALIPSO observations, MERRA2, ERA5, and ASR, respectively. Native CloudSat-CALIPSO distributions are shown in each panel in faint dotted lines. The percentage listed in each legend indicates the similarity compared to the native CloudSat-CALIPSO distribution. The four selected points are depicted geographically with the same respective colors in (e-f). (e-f) depicts the overlap percentage to native CloudSat-CALIPSO distributions for each product in every 6° × 3° gridbox. Darker shades indicate distributions that are less similar to observations.

Already apparent in Fig. 3.3 is regionally-dependent DLR behavior, both in terms of the observed PDFs and in how well reanalyses can match those observations.To guide discussion, this chapter adopts a similar methodology as the previous chapter, separating the Arctic into multiple climatically distinct subregions based on observed DLR PDFs. This is done via a clustering algorithm, where, regions with similar DLR PDFs are grouped together. These three regions are depicted geographically in Fig. 3.4b and labeled: The Central Arctic, Greenland, and the North Atlantic.

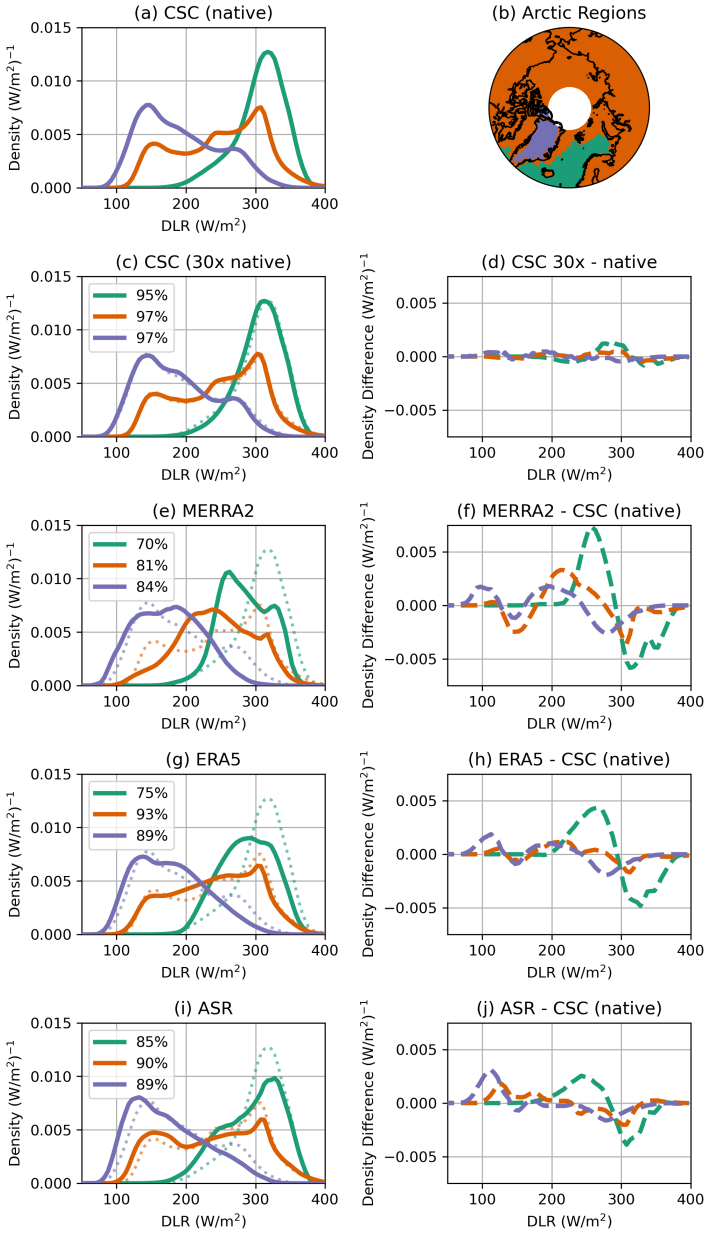

FIGURE 3.4: (a) 2007-2010 CloudSat-CALIPSO DLR density functions for the three regions outlined in (b) using the native resolution of CloudSat-CALIPSO. (c) as (a) but derived from 30 footprint averages of CloudSat-CALIPSO data. (e,g,i) as (a) but for values of DLR obtained from MERRA2, ERA5, and ASR, respectively. Each panel lists the percentage of area which overlaps the native CloudSat-CALIPSO distribution (100% represents perfectly identical distributions, 0% is zero overlap). The native distributions from (a) are overlaid in faint dotted lines for reference. (d,f,h,j) The difference in density functions relative to native CloudSat-CALIPSO PDFs.

Figure 3.4 presents DLR distributions for the three climatically distinct Arctic regions. For each region, DLR distributions for each reanalysis are compared to the native CloudSat-CALIPSO DLR distributions. While somewhat smoother than Fig. 3.3, the individually depicted CloudSat-CALIPSO PDFs in Fig. 3.3a generally resemble most closely to their associated region, as the clustering algorithm is designed to do. For example, the PDF of the Greenland sample (purple dot in Fig. 3.3) largely resembles the PDF of the Greenland region (purple in Fig. 3.4). Even the PDF from the Central Arctic region which is quite large and includes both land and ocean, resembles those of its two individual gridboxes reasonably well (red and orange curves in Fig. 3.3 vs orange curve in Fig. 3.4). As previously indicated, aggregating 30 footprints results in minimal change (3-5%) to the derived DLR PDFs compared to the native resolution (Fig. 3.4c,d). We repeated this coarsening procedure with 60 footprint averages ($\approx$ 66 km chord length) and the overlap with the native resolution only reduces by an additional percent for each region (not shown). Consequently, models should demonstrate similar distributional behavior to CloudSat-CALIPSO, despite a model grid box representing a larger area than a single CloudSat footprint.

Generally, each reanalysis most closely matches observed DLR distributions over Greenland and in the Central Arctic, but struggles with the North Atlantic region. Specifically, each product produces low DLR values more frequently than observations. MERRA2 has the poorest representation of the region with 70% of the North Atlantic distribution matching that of observations. Furthermore, spurious multi-modality seems to be apparent in the distribution when observations simply exhibit left skew. ASR is noticeably

better than the other two reanalyses in reproducing the observed North Atlantic DLR distribution (especially the highest DLR values which may induce the greatest surface warming), with ERA5 outperforming MERRA2.

ASR and ERA5 are nearly equal in capturing observed DLR distribution of Greenland, with a distributional overlap of 89% to observations. Once again, MERRA2 falls short of the other two reanalysis. Notably, however, each reanalysis product seems to miss the hints of a more opaque DLR mode that is present in the observed distribution (approximately 275 W/m^2).

Similarly, ASR and ERA5 are nearly equal in their representation of the Central Arctic, with a distribution similarity of 90-93% to that of observations. Encouragingly, both seem to capture the multimodality clearly present in the observed distribution. In contrast, MERRA2 matches observations the least, blending the two distinct modes observed at approximately 150 and 300 W/m^2 into one broad peak around 225 W/m^2, where relatively few occurrences actually occur.

These results are consistent with previous findings comparing the performance of ERA5 and MERRA2 against CloudSat and CALIPSO cloud observations. Namely that ERA5 more accurately reflects the ratio of ice versus liquid clouds compared to other reanalyses, noting that phase partitioning has a large influence on radiative effect (Jenkins and Dai, 2022, Gu et al., 2021). Moreover, Urraca et al. (2018) find noticeably reduced surface irradiance biases in ERA5 compared to MERRA2.

3.4 Diagnosing Model Deficiencies

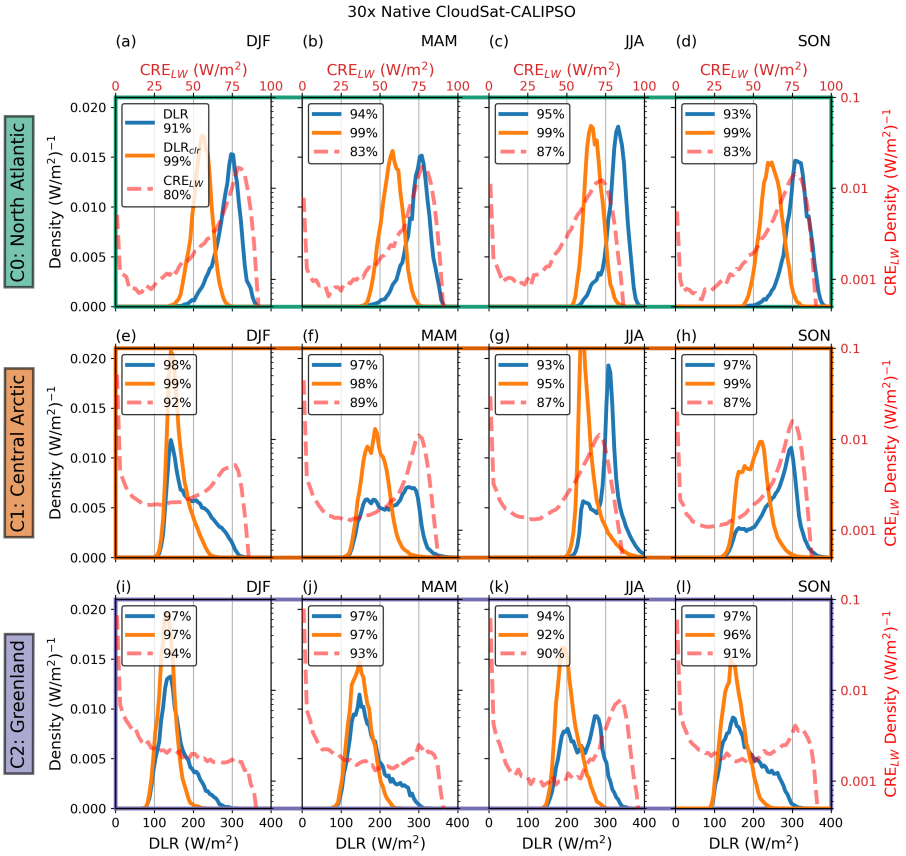

FIGURE 3.5: DLR$_{clr}$ (orange), DLR (blue) and CRE$_{LW}$ (red dashed) density functions of the unique regions in Fig. 3.4b using 30-footprint CloudSat-CALIPSO averages. Cloud-free scenes are included in the CRE$_{LW}$ density functions, which, by definition, have a CRE$_{LW}$ of 0 W/m^2. Each row contains a different region, where boxes are colored to match with those in Fig. 3.4b. Each column depicts a different season. CRE$_{LW}$ is depicted on a log scale to more clearly show the shape of the distribution. The legend of each panel lists the percentage of overlap (similarity) between using the native resolution to derive the PDFs versus the coarsened resolution. See Ch. 2 for the native resolution PDFs.

While the preceding analysis offers insights into how well models represent DLR distributions, it does not explain why these misrepresentations occur. To address this, we analyze seasonal distributions and decompose the components of DLR to better understand the sources of discrepancies between reanalyses and observations. Seasonal deconstructions

are particularly relevant, as the Arctic climate is strongly governed by seasonal variability– neglecting this variability may obscure underlying model biases.

Figure 3.5 presents the regional and seasonal radiative fluxes deconstruction generated in Chapter 2, but using 30-footprint averages. This depicts the three climatically distinct Arctic regions, separated by seasons, with associated density functions of DLR, DLR_{clr}, and CRE_{LW}. The legend of each panel indicates how much area overlaps between the native PDFs and the coarsened PDFs. For brevity, we also provide the overlap statistics for all distributions using 60-footprint averages in the form of a table (Tab. 3.1).

TABLE 3.1: Similarity of 60 footprint CloudSat-CALIPSO averages compared to native distributions of DLR, DLR_{clr} and CRE_{LW} for the North Atlantic, Central Arctic, and Greenland across different seasons. Similarities are in the form of the percentage of overlapping area to that of the native CloudSat-CALIPSO distributions.

60x Native CloudSat-CALIPSO					
Region	Variable	DJF	MAM	JJA	SON
North Atlantic	DLR	89	93	93	92
North Atlantic	DLR_{clr}	99	99	99	99
North Atlantic	CRE	74	79	83	79
Central Arctic	DLR	96	97	90	96
Central Arctic	DLR_{clr}	98	97	93	98
Central Arctic	CRE	87	84	82	82
Greenland	DLR	96	97	94	96
Greenland	DLR_{clr}	97	98	92	97
Greenland	CRE	91	89	85	86

While analyzing seasonal time scales leads to greater differences between the coarsened and native resolutions' PDFs compared to the annual scale (Fig. 3.5 versus Fig. 3.4c), the distributions are still largely the same, particularly for DLR and DLR_{clr}. Furthermore, even though CRE_{LW} (red dashed in Fig. 3.5) exhibits larger differences (typically 80-90% similarity to native resolution), the characteristics of the distribution remain consistent:

one mode near 0 W/m^2 (representing cloud-free and transmissive clouds) and another near 75-80 W/m^2 (opaque clouds). The persistence of these two modes ensures the main characteristics of DLR also persist. Specifically, when there is an approximate balance between the total frequency of the transmissive and opaque CRE$_{LW}$ modes, two evenly weighted modes in DLR arise (for example, Fig. 3.5f,k). When CRE$_{LW}$ is dominated by the opaque mode, meaning clouds are both frequent and often opaque, the DLR distribution represents a +80 W/m^2 shift in the DLR$_{clr}$ distribution (for example, Fig. 3.5a-d). Conversely, when CRE$_{LW}$ is dominated by the transmissive mode, meaning clouds are either infrequent or clouds are often transmissive, the DLR distribution mostly mirrors that of the DLR$_{clr}$ distribution (for example, Fig. 3.5i). Again, the fact that these coarsened distributions largely resemble that of the native resolution suggest that reanalyses should theoretically be able to reproduce these distributions.

Guided by Fig. 3.5, we examine reanalyses in the North Atlantic during fall, the central Arctic during spring, and Greenland during summer. The latter two regions offer some of the clearest instances of bimodal longwave flux distributions (irrespective of coarsening; Fig. 3.5f,k), and are of frequent interest to the scientific community due to their important climate impacts (Zwally et al., 2002, Solomon et al., 2014). The North Atlantic region offers a counter example with a unique *lack* of bimodality in DLR (Fig. 3.5d). While this region lacks two modes in DLR, it still features similar cloud behavior, that is, frequent occurrences of opaque clouds. These three regions and seasons are simply used to guide discussion, Tab. 3.2 provides statistics for the full set of 16 seasons and regions shown in Fig. 3.5. We use the native resolution for comparison, but note that differences on

TABLE 3.2: Reanalyses' similarity to observed distributions of DLR, DLR_{clr}, and CRE_{LW} for the North Atlantic, Central Arctic, and Greenland across different seasons. Similarities are in the form of percentage of overlapping area to that of the native CloudSat-CALIPSO distributions. Several distributions are explicitly depicted in Fig. 3.6 and are discussed in the text.

Reanalyses' Similarity To Observations													
Region	Variable	MERRA2				ERA5				ASR			
		DJF	MAM	JJA	SON	DJF	MAM	JJA	SON	DJF	MAM	JJA	SON
North Atlantic	DLR	63	64	75	67	65	70	80	73	82	82	89	87
	DLR_{clr}	92	93	93	94	99	97	95	97	95	96	98	96
	CRE	33	36	59	40	37	41	63	45	70	71	91	75
Central Arctic	DLR	74	73	81	75	90	85	86	87	87	88	88	87
	DLR_{clr}	77	88	89	92	89	94	92	94	84	88	82	89
	CRE	60	44	55	45	58	47	61	53	84	76	84	73
Greenland	DLR	87	86	71	84	89	88	79	90	85	85	78	87
	DLR_{clr}	76	79	85	84	84	82	86	89	84	85	87	88
	CRE	73	60	42	58	75	63	47	64	91	93	79	88

the order of Fig. 3.5 could be simply due to model gridbox size rather than incorrect modeling of cloud processes.

Figure 3.6 displays density functions of DLR, DLR_{clr} and CRE_{LW} for the three regions and seasons of interest, derived from each reanalysis product along with native CloudSat-CALIPSO observations for comparison. CRE_{LW} distributions include cloud-free scenes, which, by definition, have a CRE_{LW} equal to 0 W/m^2. These CRE_{LW} distributions therefore also include the effect of differing cloud frequency. Note that clear-sky fluxes in 2B-FLXHR-LIDAR are driven by a model as well. Temperature and humidity profiles for each scene are derived from ECMWF model data interpolated onto CloudSat's CPR bins (Partain, 2004) and then run through a radiative transfer model. CRE_{LW} offers the best way to evaluate the reanalyses representation of clouds as it generally removes the model environment.

Notable differences exist between the DLR distributions in observations and reanalyses.

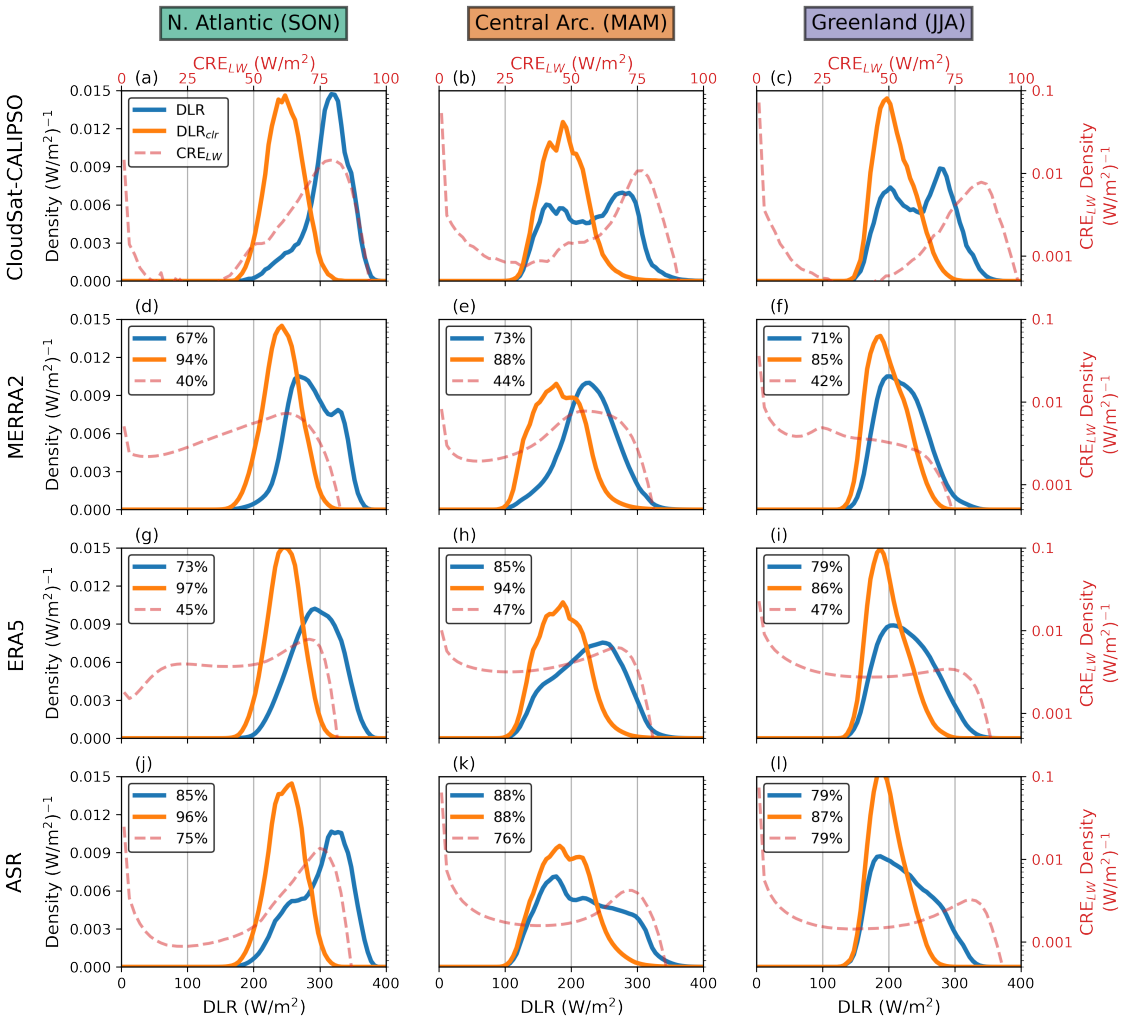

FIGURE 3.6: The three regions of interests' (see text) DLR, DLR$_{clr}$, and CRE$_{LW}$ density functions as derived by CloudSat-CALIPSO's 2B-FLXHR-LIDAR (top row), MERRA2 (second row), ERA5 (third row), and ASR (bottom row). Reanalyses panels contain the percentage of shared area compared to observed native-resolution DLR, DLR$_{clr}$, and CRE$_{LW}$ distributions. Note that CRE$_{LW}$ distributions are plotted on a different axis and use a log scale to more easily see the structure of the peaks. CRE$_{LW}$ includes cloud-free scenes.

Specifically, the two distinct modes present in Fig. 3.6b,c are almost completely absent in the reanalyses. For instance, over Greenland, reanalyses essentially miss the existence of the more opaque mode (around 275 W/m^2) entirely, which is the dominant mode in summer. These opaque occurrences are likely associated with the greatest surplus in

the surface energy balance (most conducive to melting), and so capturing their existence should not be understated. Likewise, each model tends to shift the North Atlantic DLR distribution (Fig. 3.6a) to lower values.

Generally, the reanalyses produce similar clear-sky longwave flux distributions to that of CloudSat-CALIPSO, with approximately 80-95% overlap (Tab. 3.2, Fig. 3.6). This indicates that deviations in DLR from observations are primarily driven by differences in cloud representation (i.e., CRE_{LW}) rather than variations in clear-sky model components.

A combination of cloud frequency and cloud properties (phase, height, water path, etc.) generally shape the distributions of CRE_{LW}. Observations indicate that clouds in the Arctic tend to have characteristics that cause them to preferentially lead to a very transmissive CRE_{LW} (≈ 0 W/m^2) or a very opaque CRE_{LW} (≈ 80 W/m^2). What causes this is explored more explicitly in Sect. 3.4.1. However, modeling this preferential behavior in combination with the correct cloud frequency is necessary to accurately match observed CRE_{LW} distributions. Given the strong connection between CRE_{LW} modality and DLR modality, incorrect modeling of these cloud factors leads to a lack of distinct modes in the reanalyses' DLR distributions compared to observations.

In the case of ASR (Fig. 3.6k,l), while CRE_{LW} modes are located correctly (one near 0 W/m^2 and the other near 80 W/m^2), their frequencies are incorrect. Specifically, the opaque cloud mode (near 80 W/m^2) occurs far too infrequently, and there are too many occurrences of intermediate CRE_{LW} values compared to CloudSat-CALIPSO, resulting in an under-defined second DLR mode. ERA5 exhibits similar behavior (Fig.3.6h,i) but

to a greater extent. Although the two CRE_{LW} modes are somewhat present, they are insufficiently distinct, with large variances and many intermediate values, thus also blending the two DLR modes together. MERRA2 essentially produces an average of the two defined DLR modes, forming a single intermediate peak (Fig.3.6e,f). This highlights the danger of evaluating distributions using Gaussian assumptions (i.e., mean and variance). Comparing the means of the observed and MERRA2 DLR distributions (230 W/m^2 and 228 W/m^2, respectively) might suggest similar behavior, but a complete view of the distributions reveals obvious differences. This also indicates that the 'mean state', especially in the case of CRE_{LW}, is not physically meaningful.

3.4.1 Origins of CRE_{LW} Modes

We have shown that the bimodality in CRE_{LW} is what ultimately leads to bimodality in polar DLR distributions. To better understand the origins of the two CRE_{LW} modes, we conduct a series of idealized radiative transfer calculations using an offline version of BUGSrad (Stephens et al., 2001). BUGSrad is the radiative transfer algorithm used in CloudSat-CALIPSO's 2B-FLXHR-LIDAR product and shows agreement with the Clouds and the Earth's Radiant Energy System (CERES) observations (Henderson et al., 2013, Matus and L'Ecuyer, 2017). We reproduce the profiles of temperature, humidity, reflectivity, etc. used by 2B-FLXHR-LIDAR to compute radiative fluxes and then directly modify them to understand the sensitivity of CRE_{LW} to altered conditions, such as increased optical thickness of clouds or cloud emission temperature.

Figure 3.7 illustrates an idealized experiment focusing on a summer profile over Greenland

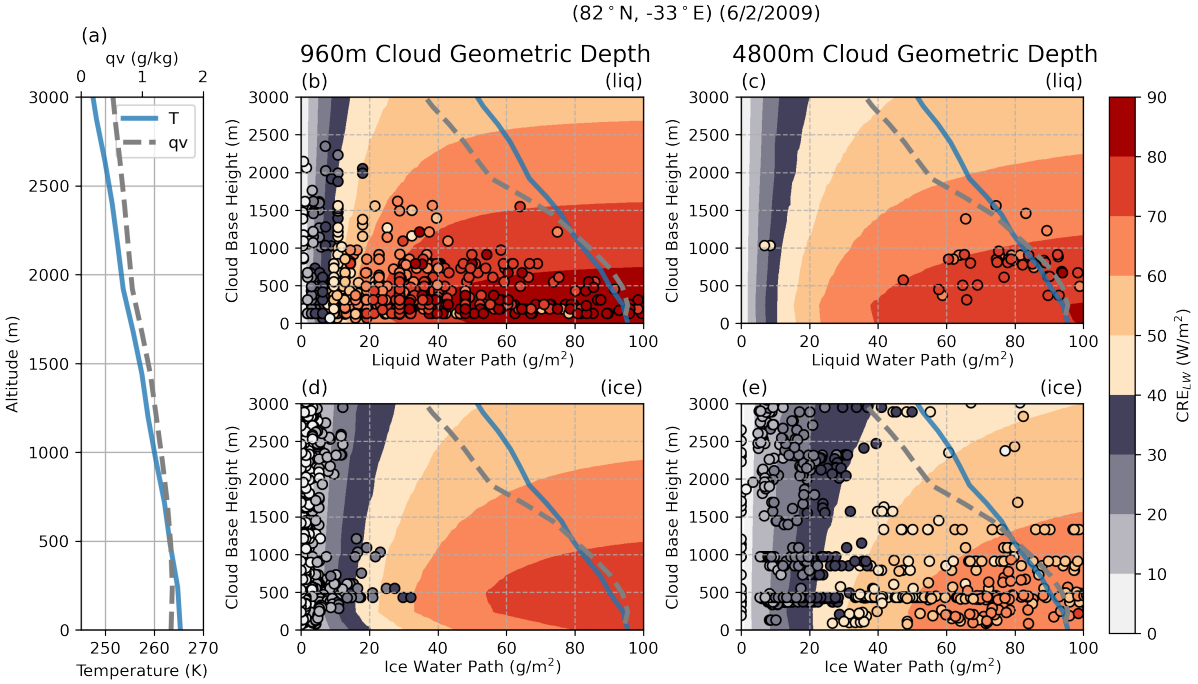

FIGURE 3.7: Synthetic experiments of cloud radiative effect using the offline version of 2B-FLXHR-LIDAR for a randomly selected scene over Greenland during the summer. (a) Depicts the profile of temperature (blue) and specific humidity (grey dashed). (b) inserts a thin liquid cloud (c) a thick liquid cloud (d) a thin ice cloud and (e) a thick ice cloud. The x-axis on each plot indicates the opacity of the cloud (via an increased water path) and the y-axis indicates where within the column the cloud base is placed. Cloud water is evenly distributed throughout the cloud. Dots represent randomly selected Arctic-wide CloudSat-CALIPSO cloud CRE_{LW} as a function of the retrieved ice or liquid water path and cloud base height. (b) samples liquid clouds with a thickness less than 1.5 km and (c) samples liquid clouds with a thickness greater than 1.5 km. (d) Samples ice clouds with a thickness less than 1.5 km and (e) samples ice clouds with a thickness greater than 1.5 km. The colorbar is broken to indicate when clouds are classified as 'opaque' (red shades). The profiles from (a) are shown on top of (b-e) for additional reference of cloud environmental conditions.

as the base case (profile in Fig. 3.7a). In this setup, the clear-sky flux remains constant, while a cloud of varying optical thickness and cloud base height is inserted into the profile. These properties are modified since they are dominant controls on cloud's thermal emission to the surface Shupe and Intrieri (2004). For simplicity, the cloud water content is evenly distributed throughout the thickness of the cloud, meaning, the water content

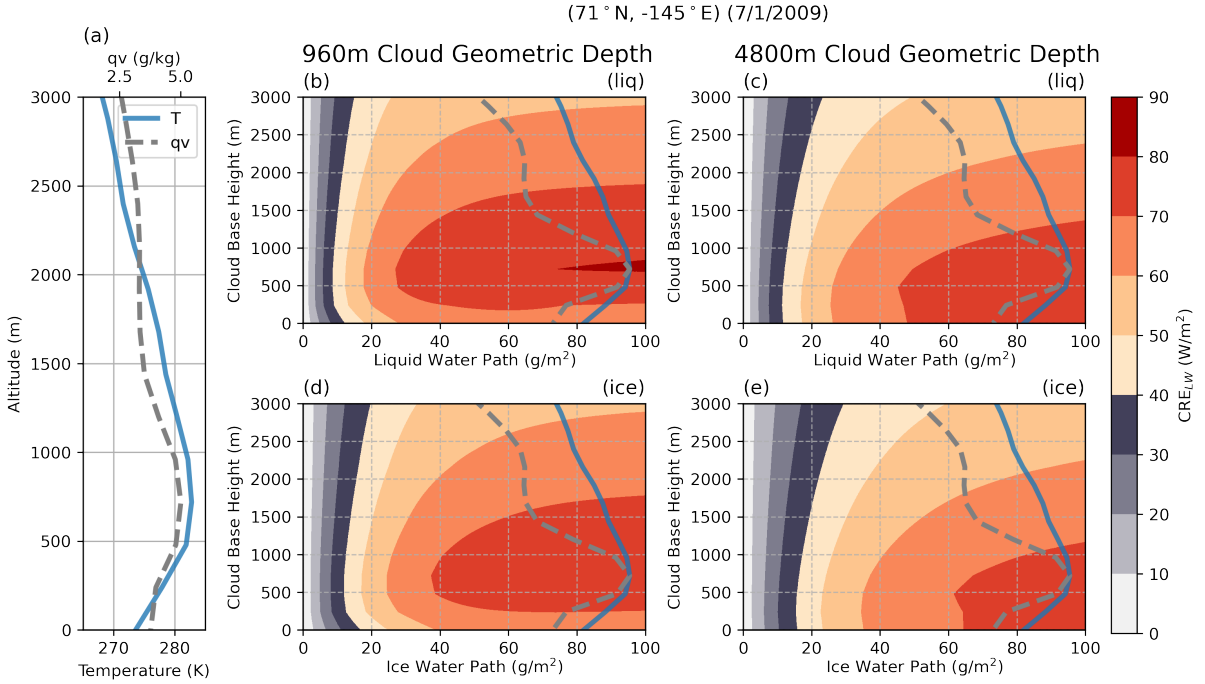

FIGURE 3.8: As Fig. 3.7 but for a profile over the Beaufort Sea in July, in which there is a humidity and temperature inversion present.

at any given cloud layer is equal to the water path divided by the number of cloud layers.

Figure 3.7b,c depict clouds composed entirely of liquid water with thicknesses of approximately 1 km and 5 km, respectively. Figure 3.7d,e is identical but for clouds composed entirely of ice. In all cases, a large amount of the phase-space is covered by a CRE$_{LW}$ >40 W/m^2, representing values falling into the 'opaque' mode of Fig. 3.6c. Note that some of these synthetic clouds may not actually be observed in nature, for example, liquid clouds with high water path will generally not exist several kilometers above the surface in the Arctic (i.e., top right of Fig. 3.7b and Fig. 3.7c) but are included for completeness.

Increasing the geometric thickness of a cloud (Fig. 3.7c,e) generally mirrors the behavior of the thinner cloud (Fig. 3.7b,d), although it does slightly reduce the CRE$_{LW}$ throughout

the phase-space. This reduction results from a decrease in the water content (and thus the optical depth) of low-level cloud layers that emit at warmer temperatures due to the water path being spread over a greater number of layers. Elevating the cloud base height (decreasing the emission temperature) reduces the CRE_{LW} more greatly for optically thick clouds versus more transmissive clouds. For instance, a 1 km-thick cloud with a LWP of 80 g/m^2 has a CRE_{LW} of approximately 80-90 W/m^2 at 500m versus 60-70 W/m^2 at 2500m, whereas a cloud with a LWP of 10 g/m^2 has a CRE_{LW} of approximately 40-50 W/m^2 at 500m versus 30-40 W/m^2 at 2500m (Fig. 3.7b). Nevertheless, the value of CRE_{LW} remains substantial regardless of height, indicating that even a cloud further from the surface can exhibit a large CRE_{LW} if it is sufficiently opaque.

Overlying Fig. 3.7b-e are randomly selected scenes from CloudSat-CALIPSO; these are observations and not synthetically modified in any way. Water path values are directly retrieved from the 2B-FLXHR-LIDAR processing pipeline (Henderson et al., 2013, Henderson and L'Ecuyer, 2022) and are derived from a combination of radar, lidar, and reanalysis data. Points generally follow the underlying idealized simulations' pattern. Scenes that have lower CRE_{LW} (grey dots within red contours), may be more humid, colder, or have a geometrically thicker (and thus optically thinner at a single level) cloud, relative to the idealized simulations. Scenes that have higher CRE_{LW} (red dots within grey contours) may be drier, warmer, or have a geometrically thinner (and thus optically thicker at a single level) cloud. Notably, these points are sampled from the entirety of the Arctic, meaning these results generalize well for the domain. This is further exhibited in Fig. 3.8, which presents similar information but for a profile that contains a temperature

and humidity inversion, a common feature in the polar regions. Notably, the pattern remains largely consistent from the previous examples, but the peak CRE_{LW} now aligns with the level at which the inversion exists (i.e., where the temperature is greatest).

Much of the phase-space in Figs. 3.7 and 3.8 being covered by large CRE_{LW} values is a characteristic feature of the Arctic environment. This results from the longwave cloud radiative effect saturating relatively rapidly with increasing water path (Shupe and Intrieri, 2004, Sedlar et al., 2011), coupled with climatologically low water vapor values, reducing clear-sky emissivities. And hence, while converting the cloud to ice (Fig. 3.7d,e) reduces the CRE_{LW} due to the lower absorption characteristics of ice versus liquid, much of the phase-space is still covered by CRE_{LW} >40 W/m^2.

One can also get an idea of the frequency of these cloud configurations from the random sampling in Fig. 3.7. For example, thin liquid clouds infrequently have a base above approximately 2 km (exhibited by the low density of dots in Fig. 3.7b at this level) and generally fall into the opaque regime. Similarly, ice clouds typically exhibit two populations, geometrically thin clouds that tend to be transmissive and geometrically thick clouds that are often opaque. The fact that CRE_{LW} saturates much more rapidly for liquid versus ice further promotes nearly all liquid clouds falling into the opaque cloud mode. The relative populations of these clouds and their associated radiative effect are analyzed more explicitly in Figs. 3.9 and 3.10.

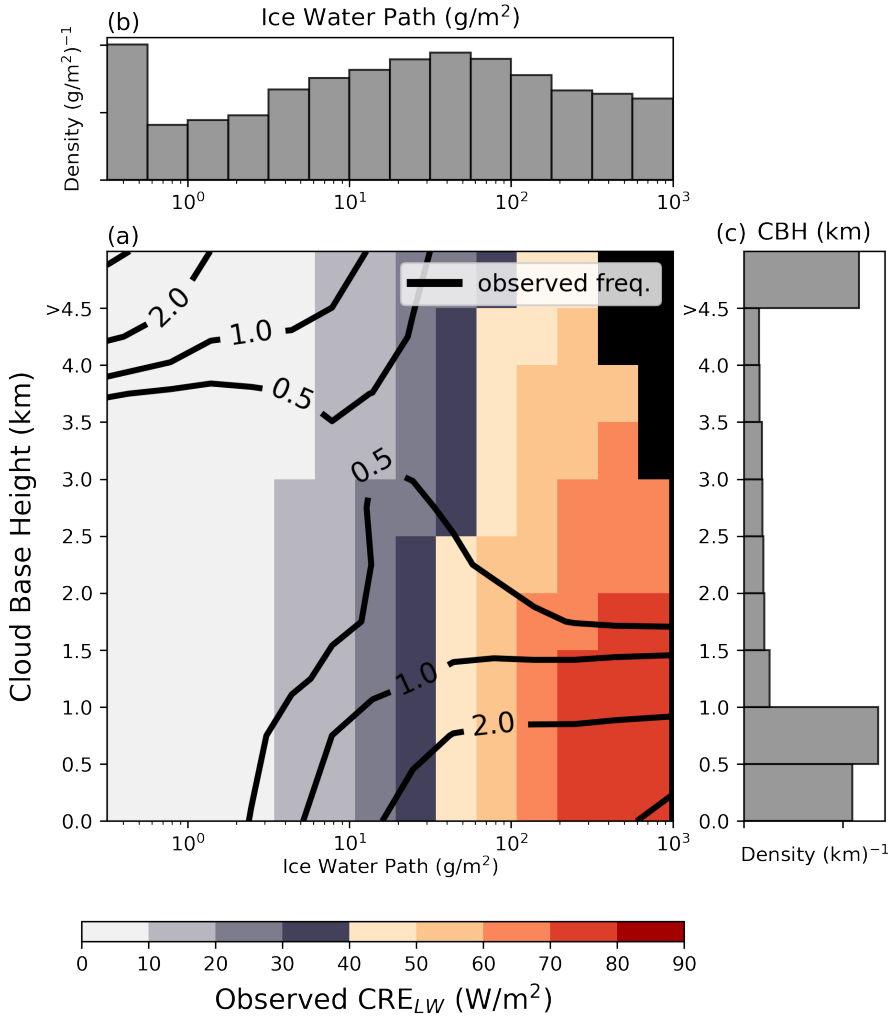

FIGURE 3.9: (a) Mean values of CRE_{LW} as a function of observed ice water path and cloud base height for Arctic (poleward of 60 N) ice cloud scenes according to CloudSat and CALIPSO observations. Ice clouds are defined by those scenes in which the fraction of ice water path to total water path is greater than 2/3 (see text). Black contours indicate the relative densities of observed cloud configurations. Contour intervals depict the percentage of the total dataset, bins with less than 100 samples are omitted (indicated by black boxes), as are multi-layer clouds. (b) and (c) individually depict the densities of ice water path and cloud base height, respectively. Note that clouds bases above 4.5 km are included in the highest bin. Similarly, water paths beyond the edges of the histogram are clipped and included in the most extreme bins.

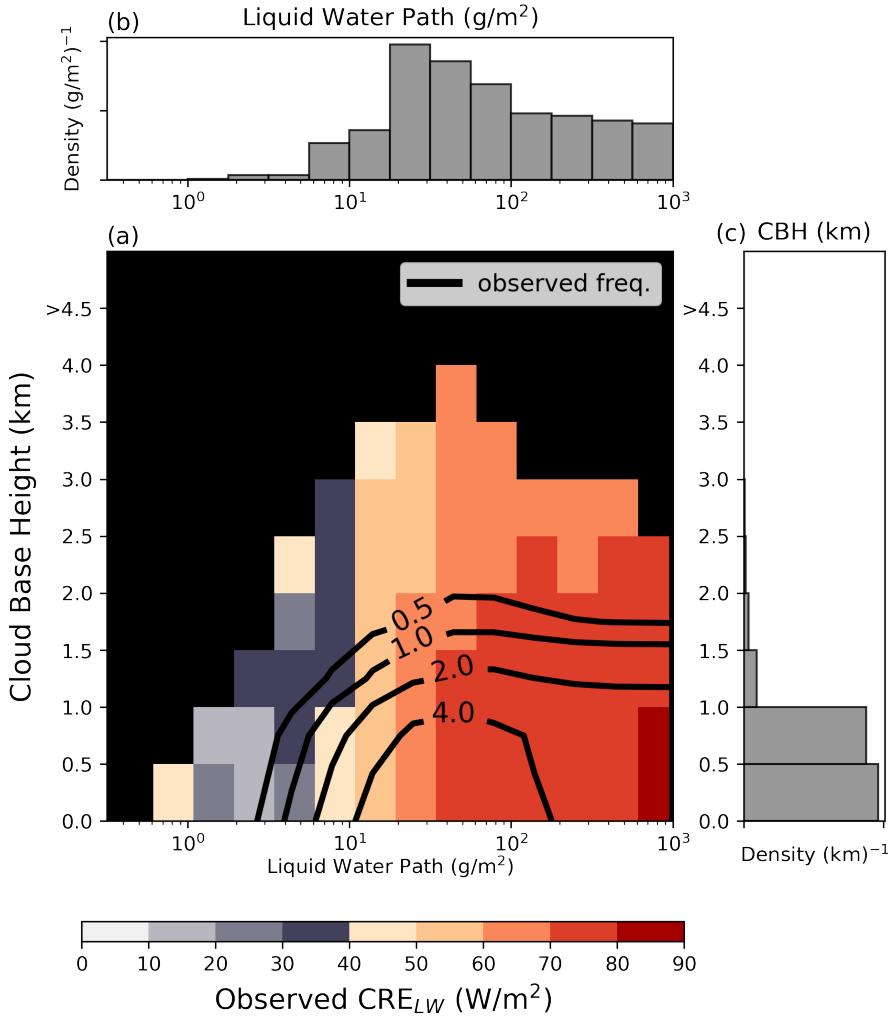

FIGURE 3.10: As Fig. 3.9 but for liquid clouds.

Figure 3.9 depicts the frequencies of ice water path and cloud base height for observed Arctic ice clouds, derived from CloudSat and CALIPSO observations. Alongside this, the associated CRE_{LW} is provided. Figure 3.10 provides similar information but for observed liquid clouds. Here we opt for a simple phase definition to enable a more direct comparison with models. In this approach, scenes are classified as 'multi-layer' if multiple distinct cloud layers are detected (approximately one-third of scenes). If a single cloud

layer is identified and IWP/TWP >2/3 (ice water path divided by total water path), the scene is categorized as 'ice'. Conversely, if a single cloud layer is detected and IWP/TWP <2/3, the scene is classified as 'liquid', encompassing mixed-phase cloud occurrences as well. A relative threshold of 2/3 is used since many model clouds contain some small amount of both liquid and water, and thus, a non-zero definition is insufficient. While the selection of the threshold is arbitrary, it facilitates a straightforward comparison with models; moreover, the results remain largely the same whether this threshold is increased or decreased. Furthermore, using the definition of phase as determined by 2B-CLDCLASS-LIDAR leads to similar results, indicating that the phase classification presented here, although simple, is relatively robust.

The observed distributions of ice and liquid water path spans several orders of magnitude, with peaks in occurrence near values of 20-100 g/m^2 for both distributions. Both liquid and ice clouds have a peak in occurrence for cloud base heights below 1 km, while ice clouds have an additional peak further from the surface (bases of 4.5 km or higher). The CRE_{LW} behavior generally mirrors that of the synthetic experiment, confirming that those findings generalize well. That is, aligning with findings in Fig. 3.7, a large portion of ice clouds are high and thin (transmissive) and a separate population are low and thick (typically opaque). Liquid clouds are near the surface and typically opaque.

Thus despite the inhomogeneity present across the Arctic, characteristically low water vapor values allow for clouds with a sufficiently high water path to have a large CRE_{LW}

regardless of many macro and microphysical properties of the cloud, hence the ubiquitous nature of the states. Of course, differing cloud properties contribute to the variance exhibited in the opaque CRE_{LW} mode. For example, clouds that are geometrically thin, predominately liquid, near the surface, and in a extremely dry environment, likely contribute to the highest CRE_{LW} values ($\approx$ 90-100 W/m^2) of the opaque cloud mode. Clouds that are geometrically thicker, predominately ice, elevated further from the surface, and in a moister environment likely contribute to lower CRE_{LW} values ($\approx$ 40-50 W/m^2) of the opaque cloud mode. For example, CRE_{LW} shift towards lower values for the opaque cloud mode in the North Atlantic and Central Arctic during summer when water vapor values are typically larger (Fig. 3.5c,g). In contrast, Greenland exhibits a shift towards higher CRE_{LW} values during the summer (Fig. 3.5k) due to increased occurrence of liquid and mixed-phase clouds (see Chapter 2).

3.4.2 Clouds in ASR

There are challenges associated with directly comparing cloud parameters from conventional reanalyses against instantaneous satellite observations (e.g., Stengel et al., 2018). Thus, in the subsequent discussion, analysis is centered on the Arctic System Reanalysis product as its output most closely aligns CloudSat-CALIPSO observations and it most realistically represents cloud processes (Fig. 3.6, Tab. 3.2). We aim to understand why ASR typically underestimates opaque clouds. Note that due to models' tendency to simulate optically thin clouds that are undetectable by observations (Kay et al., 2016), directly comparing cloud frequency between models and observations can be difficult.

There is an expectation that some portion of the 'clouds' in models exhibit behavior akin to 'clear' scenes in CloudSat-CALIPSO (i.e., having a near-zero radiative effect). That is to say, even if models could perfectly represent the climate system, the cloud frequency may not exactly match observations. For simplicity, a total (ice + liquid) water path threshold of 10^{-3} g/m^2 is used to demarcate clear versus cloud scenes in ASR. Using a threshold representative of a less sensitive instrument (for example, 10^{-1} g/m^2) does not have a meaningful effect on the presented results. 'Ice' includes all frozen precipitation (i.e., ice, snow and graupel) while 'liquid' includes cloud water and rain.

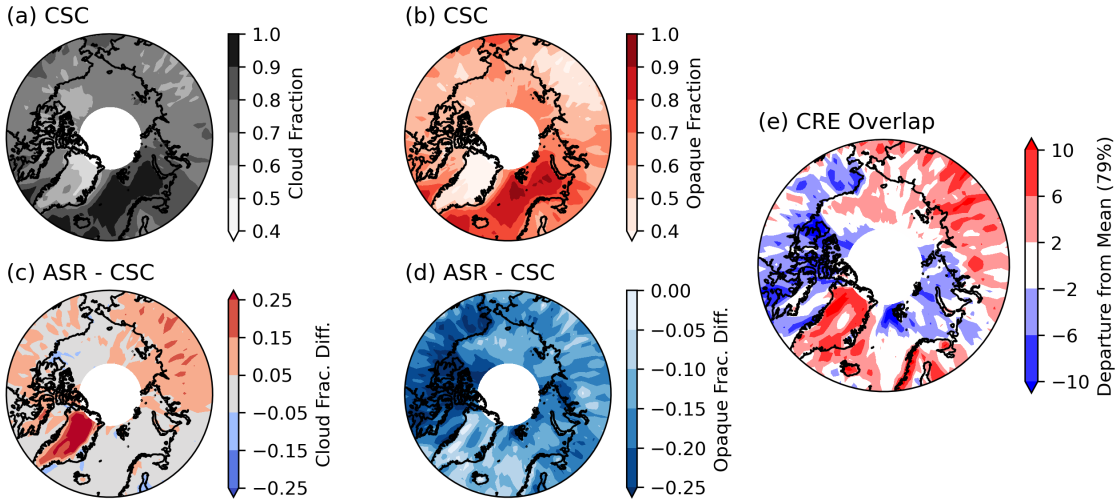

FIGURE 3.11: (a) Cloud fraction according to CloudSat-CALIPSO observations averaged over 2007-2010. (b) As (a) for but for the fraction of time in which CRE$_{LW}$ >40 W/m^2, relative to all scenes. (c,d) depicts the difference in (a,b) relative to ASR. (e) The overlap percentage (see text) for ASR CRE$_{LW}$ distributions compared to CloudSat-CALIPSO. Note that the mean (79%) has been removed to better show regions of enhanced or diminished skill.

The structure of CRE$_{LW}$ in ASR resembles that of CloudSat-CALIPSO observations for all three regions of interest: the Central Arctic, Greenland, and the North Atlantic (Fig. 3.6). Namely, two clearly defined modes are present in approximately the correct

location; however, ASR lacks an opaque mode with sufficient frequency making low and intermediate CRE_{LW} seem relatively frequent.

Figure 3.11 provides some spatial context to these mischaracterizations in the form of cloud frequency, opaque cloud frequency, and overlap statistics for CRE_{LW} in ASR compared to observations. ASR generally has more cloud cover than CloudSat-CALIPSO, particularly over Greenland, where it exceeds observations by nearly 25%. Although cloud cover is more prevalent, clouds are less frequently opaque in ASR compared to observations (both in absolute occurrence and relative to cloud occurrences), especially in the western Arctic (Fig. 3.11d). Regions with lower observed opaque cloud frequency (Fig. 3.11b) tend to have better overlap percentages (Fig. 3.11e), for example, Greenland and eastern Siberia. Conversely, areas with noticeably deficient opaque cloud frequency in ASR (Fig. 3.11d), such as the Arctic Archipelago, show relatively poor matches with observed CRE_{LW} distributions. These results further suggest that opaque clouds are a dominant source of issue in appropriately capturing longwave flux distributions.

To unravel the reasons behind the apparent over-prevalence of the transmissive (and intermediate) CRE_{LW} in ASR compared to CloudSat-CALIPSO, Figs. 3.12, 3.13 and 3.14 present the distributions of CRE_{LW} of each cloud phase, for each region of interest. The same phase definitions of ice, liquid and multi-layer clouds, as defined in the previous section are used. In all cases, ASR has nearly double the occurrence rate of ice clouds (Figs. 3.12-3.14a) and about half the occurrence of liquid clouds (Figs. 3.12-3.14b) compared to observations. This aligns with previous findings, where climate models tend to

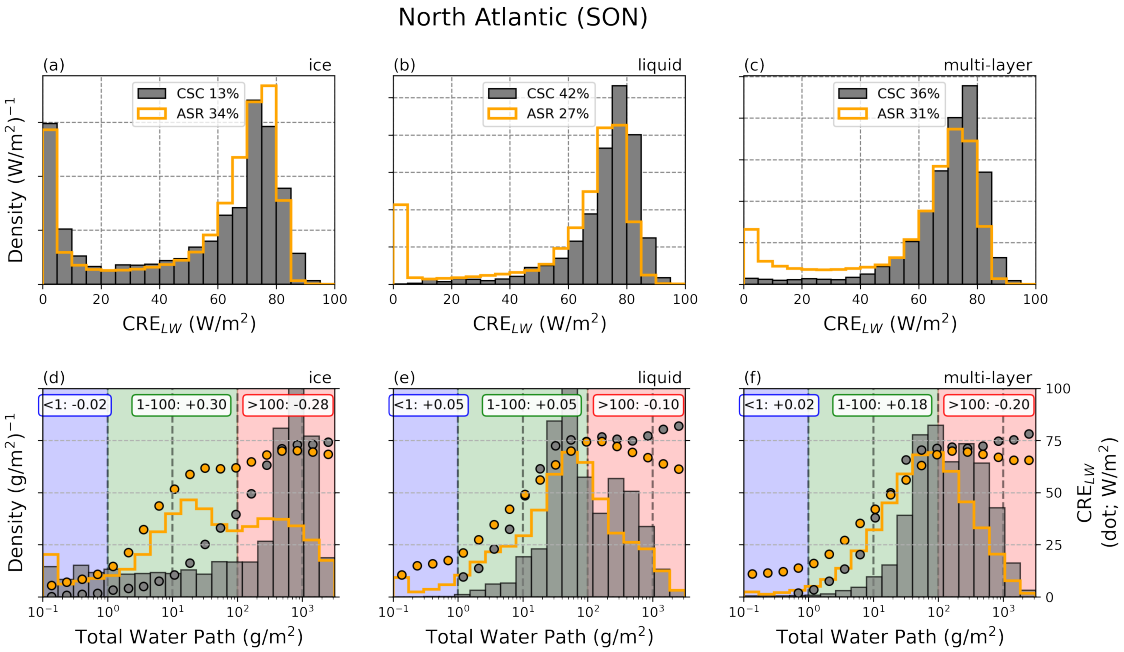

FIGURE 3.12: (a-c) Density functions of CRE_{LW} for the North Atlantic region during September through November using ASR (orange line) and CloudSat-CALIPSO (grey bar), separated by ice, liquid and multi-layer clouds, respectively. (d-f) As (a-c) but density functions of total water path (TWP). For each water path bin, the mean CRE_{LW} for CloudSat-CALIPSO (grey dot) and ASR are also provided (orange dot). The difference in relative occurrence from ASR to CloudSat-CALIPSO (ASR-CSC) of three different groups of TWP are provided at the top of each plot: less than 1 g/m^2, 1-100 g/m^2, and greater than 100 g/m^2. The lowest and highest bins are clipped such that they include values lower than 10^{-1} and higher than 3x10^3 g/m^2, respectively.

produce too many ice clouds and too few liquid clouds (Cesana et al., 2012), though this may be improving in some models (McIlhattan et al., 2020). While ice clouds also have an opaque mode, it is less frequent compared to liquid clouds and intermediate CRE_{LW} are also slightly more frequent. Thus, this drastic disparity in phase frequency is likely a prominent cause for the differences in the CRE_{LW} distributions depicted in Fig. 3.6.

In some cases, the CRE_{LW} distributions of ASR match quite closely with observations (for example, all North Atlantic phases; Fig. 3.12a-c), while in others, there's a noticeable lack

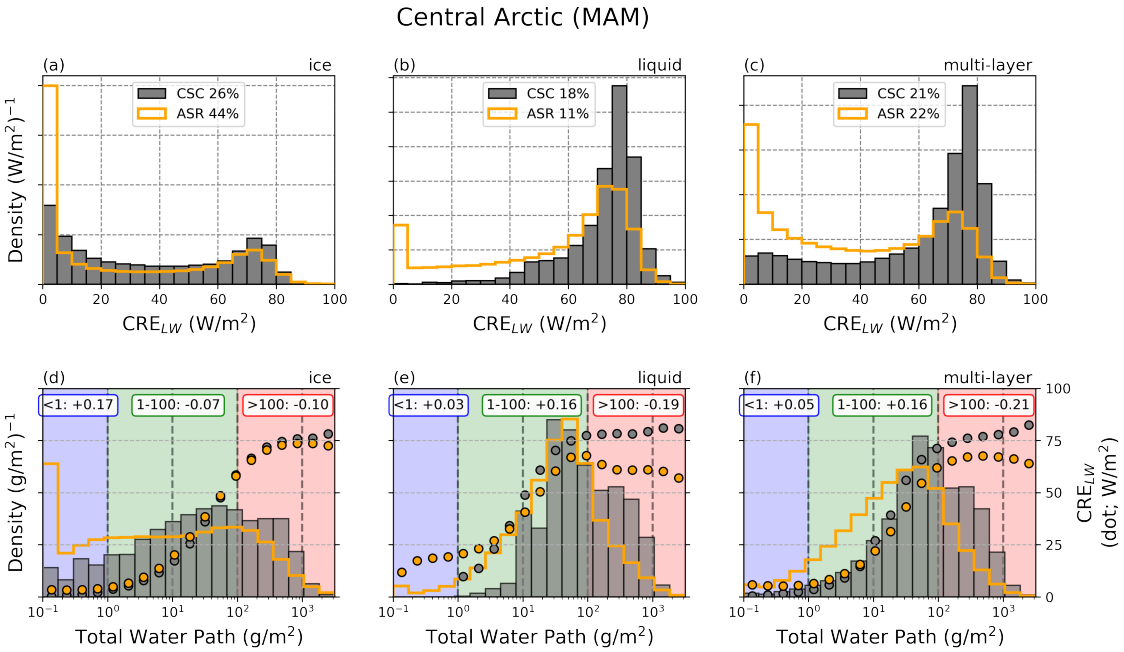

FIGURE 3.13: As Fig. 3.12 for the Central Arctic during March through May.

of opaque cloud occurrences (for example, liquid and multi-layer clouds in the Central Arctic and Greenland; Figs. 3.13&3.14b,c). The latter leads to intermediate CRE$_{LW}$ values that are relatively frequent in ASR.

In most cases, ice cloud distributions between ASR and observations are relatively similar, though there is a larger population of near 0 W/m^2 cases in ASR. Additionally, ASR produces a notable number of transmissive liquid clouds (Figs. 3.12-3.14b). While transmissive ice clouds are often observed, transmissive liquid and mixed-phase clouds are not frequently observed in the Arctic. Due to the highly reflective nature of liquid droplets, it is unlikely that CALIPSO's CALIOP misses a large number of ultra-thin liquid layers, and CALIPSO observations have been shown to align well with ground-based detection capabilities of liquid clouds (Lacour et al., 2017), being particularly adept at identifying

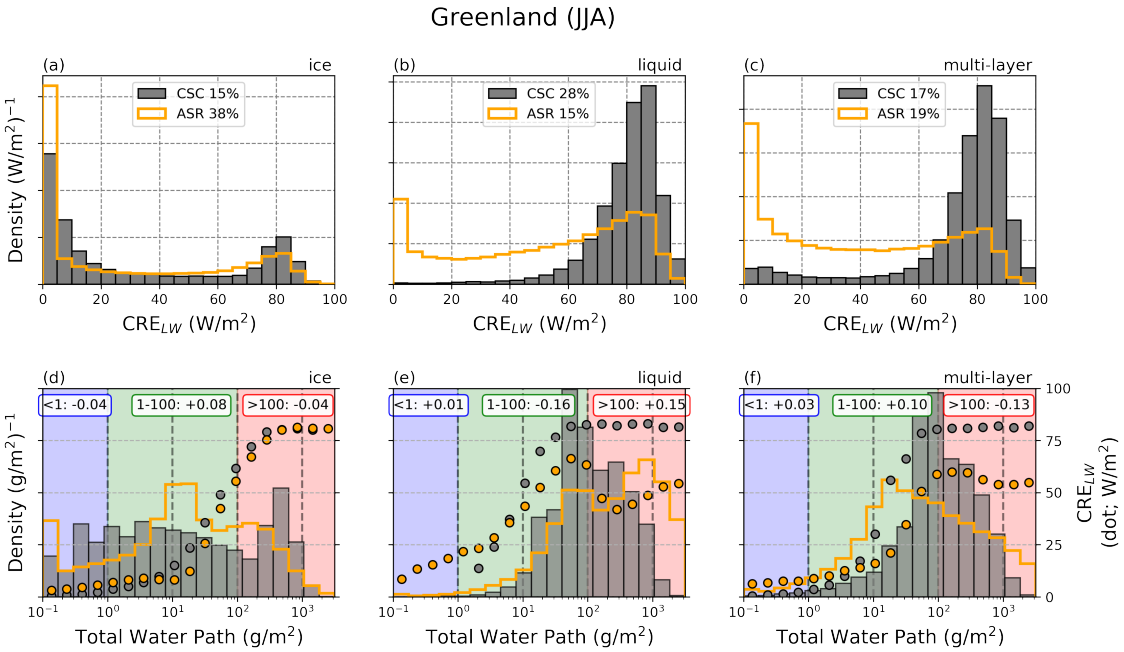

FIGURE 3.14: As Fig. 3.12 for Greenland during June through August.

optically thin cloud features (Devasthale et al., 2011).

While comprehensively explaining the causes of the discrepancies between ASR and observations is outside the scope of this manuscript, Figs. 3.12-3.14(d-f) offer an initial insight into potential model inaccuracies within the three regions. Aligning with the overabundance of transmissive liquid and multi-layer clouds, Figs. 3.12-3.14(e,f) tend to show that relatively high water path values (defined as >100 g/m^2) are less common in ASR versus observations, compensated by a relative increase in low and intermediate water path values (defined as <1 and 1-100 g/m^2, respectively). These lower water path bins often exhibit low and intermediate CRE$_{LW}$ values, thus leading to an opaque cloud mode that is less frequent. For example, in the Central Arctic, relative to all multi-layer clouds, very optically thick (>100 g/m^2) clouds occur 21% less frequently in ASR versus

observations (Fig. 3.13f). The scatter points of mean CRE_{LW} as a function of TWP (grey and orange dot) illustrate how low values of water path typically correspond with low CRE_{LW} (as expected), while high values of water path typically correspond to high CRE_{LW} (as expected). Hence, ASR produces a less defined opaque mode for multi-layer clouds (Fig. 3.13c)

However, the relative frequencies of total water path between ASR and observations is not the sole issue. Figure 3.13d demonstrates that while the behavior of CRE_{LW} as a function of TWP for ice clouds is, on average, similar between observations and ASR in the Central Arctic (i.e., the grey dots and orange dots share similar shapes), the behavior of liquid and multi-layer clouds (Fig.3.13e,f) presents more contrasting patterns. Not only is the frequency mismatched between models and observations (again, a deficiency in very high TWP values), but the relationship between mean CRE_{LW} and water path is quite different. While observations saturate and peak at TWP values near 100 $\mathrm{g/m^2}$ (with a CRE near 75 $\mathrm{W/m^2}$), consistent with the synthetic studies, there is a decrease in mean CRE_{LW} (to about 55 $\mathrm{W/m^2}$) for ASR.

This contrasting CRE_{LW} behavior is present in all three regions to varying degrees. For example, in Greenland liquid and multi-layer clouds it seems to have an especially large effect: Very high water path values are more common in ASR liquid clouds versus observations (Fig. 3.14e); this ought to produce more clouds with a large CRE_{LW}. However, the mean CRE_{LW} is below 50 $\mathrm{W/m^2}$ for high TWP values, leading to a drastic under-representation of the opaque mode and an over-prevalence of intermediate values

(Fig. 3.14b). This discrepancy may stem from differences in cloud emission temperature (i.e., where the cloud resides relative to an inversion or the strength of said inversion), or how the water is distributed vertically in the cloud; however, further investigation is required to determine the cause.

Despite these deficiencies, considering the degrees of freedom, the fact that ASR CRE_{LW} distributions match relatively closely to observations in these regions is impressive. While perhaps occurring at the wrong frequency, the central pattern of an opaque mode existing at approximately 75-80 W/m^2 exists in every region and every phase, as is exhibited in observations. These results are generally encouraging for ASR's ability to resolve Arctic cloud properties and are certainly a strong foundation to improve upon. Accurately representing the impacts of clouds on Arctic climate and quantifying feedbacks, will however, require improved representation of the frequencies of the opaque and transmissive modes.

3.5 Discussion and Conclusions

This study explores how well global and regional reanalyses resolve two recurring Arctic radiative states, deemed opaque and transmissive, exhibited through bimodal surface longwave flux distributions. These states exert a large impact on the surface energy balance and are observable on basin-wide scales in many seasons. Leveraging the vertical profiling capabilities provided by CloudSat and CALIPSO, we examine how reanalyses of varying resolution and complexity (MERRA2, ERA5, and ASR) fare in capturing the states' behavior across the entire domain.

Although model gridboxes represent areas larger than a single CloudSat footprint, Arctic radiative states are found to be spatially homogeneous, existing on the order of tens to hundreds of kilometers in chord length (Figs. 3.1 and 3.2). Furthermore, 'coarsening' Cloudsat-CALIPSO observations by averaging consecutive sets of 30 and 60 footprints leads to minimal changes in the derived PDFs and bimodality in DLR is still frequent (Fig. 3.4). Consequently, models should be capable of resolving much of the distributions' behavior.

While ASR and ERA5 tend to outperform MERRA2, none of the reanalyses are able to resolve the distinct modes of DLR exhibited in observations for the regions examined in this study (Fig. 3.6b,c). This is mostly due to the inability of reanalyses to capture observed cloud characteristics and frequency, indicated by poor matches to observed CRE_{LW} distributions. This is a result that is expected given that clouds are predominantly parameterized in models and are commonly produced with an incorrect frequency, phase, and radiative impact (Curry et al., 1996, Taylor et al., 2019, Inoue et al., 2021, Yeo et al., 2022).

Explicitly considering full DLR distributions reveals several details that would be obscured when only comparing means and standard deviations. For example, MERRA2 has a tendency to merge the two observed, well-defined CRE_{LW} modes into a single intermediate modem, ultimately reflecting a fusion of the two defined modes in DLR as well (Fig. 3.6e,f). While this blending may lead to high model skill from a Gaussian perspective, i.e., comparing the mean and variance of distributions between models and

observations, it represents a state that is infrequently realized in nature. Since surface longwave radiation is considered an 'inclusive' climate variable in the Arctic (Raddatz et al., 2015), this potentially affects the evolution of many other components of the Arctic climate system. This misrepresentation from a Gaussian perspective underscores the necessity of evaluating models beyond merely the first two moments of the distributions (Graham et al., 2017).

While some work has already been dedicated to understanding the behavior of these states from a process-oriented perspective (e.g., airmass intrusions, transformations, and other transient events), we explore how the two CRE_{LW} modes arise from a purely radiative perspective. Using the offline version of the 2B-FLXHR-LIDAR product, we find the combination of two main factors lead to the frequent development of two modes in CRE_{LW}: 1) CRE_{LW} tends to approach zero at total water path values less than 1 g/m^2 and saturates relatively rapidly (to 80 W/m^2) at higher total water path values (>50-100 g/m^2) and 2) there is preferential behavior for very low water path values (such as thin cirrus clouds) and very high values (such as thick ice clouds or low-level liquid clouds).

Since ASR most explicitly resolves cloud processes and its CRE_{LW} distributions match observations more closely (Fig. 3.6), we dig further into the clouds produced in ASR. Discrepancies in ASR's representation of Arctic radiative states generally occurs due to differences in phase partitioning of clouds (i.e., a relative increase in ice clouds versus liquid clouds in ASR compared to observations), as well as differences in water path values. For example, an overabundance of ice clouds versus liquid clouds leads to a general lack

of opaque mode occurrences since ice clouds, on average, are more transmissive (though ice clouds do contribute to the opaque cloud mode). Additionally, the distributions of water path for liquid and multi-layer clouds are typically shifted to lower values in ASR compared to observations. Consequently, this results in a reduction in water path values where CRE_{LW} is saturated (>100 g/m^2) and an increase in the 'transition zone' (1-100 g/m^2), where CRE_{LW} is frequently at low and intermediate values. However, matching distributions of water path to observations is not the sole issue for ASR. Particularly for liquid clouds, ASR exhibits lower mean CRE_{LW} values ($\approx$ 50-55 W/m^2 compared to 75-80 W/m^2) for a cloud with the same water path compared to observations. This discrepancy leads to a shift in the opaque mode (to lower values), despite water path distributions sometimes exceeding observations (Fig. 3.14e). Furthermore, ASR exhibits a relatively large population of transmissive liquid clouds that are seldom observed in nature.

It is important to emphasize that this study is not aimed at discrediting reanalysis datasets, especially the global products (like MERRA2 and ERA5); their scope naturally entails certain limitations compared to regional counterparts (like ASR). Nonetheless, it is crucial to highlight these limitations as reanalyses are frequently used to study surface radiative fluxes in the Arctic and drive ice sheet and sea ice models (Serreze et al., 2007, Zampieri et al., 2021, Jenkins and Dai, 2022, Murto et al., 2023). The results underscore the need for further advancements, particularly in the development of regional reanalysis products which show increased skill in representing surface flux distributions. Modeling these radiative modes is undoubtedly challenging, however, due to their large impact on

the surface energy budget, it is imperative to accurately resolve them. Once we are able to model these states in today's climate, the fidelity of predicting their behavior in a future climate becomes more practical.

It is crucial to recognize that the relationship between observations and models is complimentary (Kay et al., 2016). Insights can be gained from both directions. Understanding what drives these states will aid in improving their representation in models, potentially leading to new insights about the underlying cloud processes themselves. This is especially true for sparsely observed regions like the Arctic. For future studies, we suggest continued investigation into the factors contributing to model discrepancies in radiative regimes, such as understanding how opaque clouds interact with inversions in models versus observations since this has an influence on both CRE_{LW} and cloud lifetime. Additionally, we encourage the development of non-Gaussian methods for evaluating model skill and the exploration of how these states may evolve in the future based on our current understanding.

Chapter 4

A Rapid Decline of the Transmissive Atmospheric Radiative Regime in the Western Arctic*

*This is a lightly modified version of: Bertossa, Cameron, and Tristan L'Ecuyer. "A Rapid Decline of the Transmissive Atmospheric Radiative Regime in the Western Arctic" (in prep. for submission to GRL)

4.1 Preface

The previous chapters have shown that bimodality in longwave flux distributions arises from several distinct features of the polar regions. First, the high latitudes are often characterized by cold, dry, and stable conditions that suppress the formation of optically thick clouds and reduce the clear-sky emissivity (i.e., that caused by water vapor and well-mixed gases; Curry et al., 1996, Przybylak et al., 2003, Eastman and Warren, 2010). These conditions form the transmissive state (Fig. 4.1c left modes). Secondly, fluxes of heat and moisture into the Arctic atmosphere, driven by local and non-local processes, often lead to cloud formation (Kay and Gettelman, 2009, Doyle et al., 2011, Woods et al., 2013, Gimeno et al., 2019, Papritz et al., 2022). Since clouds rapidly approach blackbodies with small increases in water path, clouds can increase surface downwelling longwave radiation (DLR) by 70–90 W/m^2 with liquid water paths as low as 30 g/m^2 (Shupe and Intrieri, 2004) and ice water paths of 100 g/m^2 (Miller et al., 2015). Further increases in water path have little influence on the cloud's longwave radiative effect (CRE$_{LW}$), meaning many different cloud configurations can induce similar longwave effects on the surface, whether they be ice, liquid, or mixed-phase (Ch. 3). This consistent influence from clouds gives rise to a distinct opaque mode in DLR (e.g., Fig. 4.1c right modes), whose separation from the transmissive mode is approximately defined by the 70–90 W/m^2 CRE$_{LW}$ saturation point (Cox et al., 2015). Since DLR is an 'inclusive' variable in the Arctic climate (Raddatz et al., 2015), meaning its behavior projects onto many other geophysical variables, bimodality in DLR serves as a robust indicator of two broader

atmospheric states (Stramler et al., 2011a).

The seasonal cycle largely determines whether local or non-local sources of heat and moisture contribute to the Arctic thermodynamic budget (Kurita, 2011). For example, in winter, the Arctic Ocean is largely ice covered so moisture perturbations are heavily driven by non-local sources (Sorteberg and Walsh, 2008, Gimeno-Sotelo et al., 2019). In contrast, during autumn, strong ocean-atmosphere coupling coincides with minimal sea ice, making local moisture sources also important (Kay and Gettelman, 2009, Morrison et al., 2018). Since local sources are less episodic, summer and autumn typically correspond to enhanced moisture, warmer temperatures, and higher cloud fractions compared to winter and spring (Fig. 4.1a).

Thus, the seasonal cycle largely influences DLR distributions by (1) changing clear-sky fluxes, modifying the location of the transmissive mode and (2) influencing cloud frequency, modifying the frequency of the transmissive mode. In summer, for example, warm and humid conditions are accompanied by frequent optically thick liquid-containing clouds (Shupe, 2011, Yu et al., 2019), shifting clear-sky distributions to higher values while also leading to a predominantly opaque state (Fig. 4.1c second panel). This phenomenon is not confined to the seasonal cycle, however. The North Atlantic storm track remains warm, moist, and predominantly covered by opaque clouds, regardless of the season (Mioche et al., 2015, Alekseev et al., 2019, Bertossa and L'Ecuyer, 2024).

As the Arctic continues to warm and moisten in response to both local and non-local forcings (Woods and Caballero, 2016, Nygård et al., 2020), DLR is expected to increase

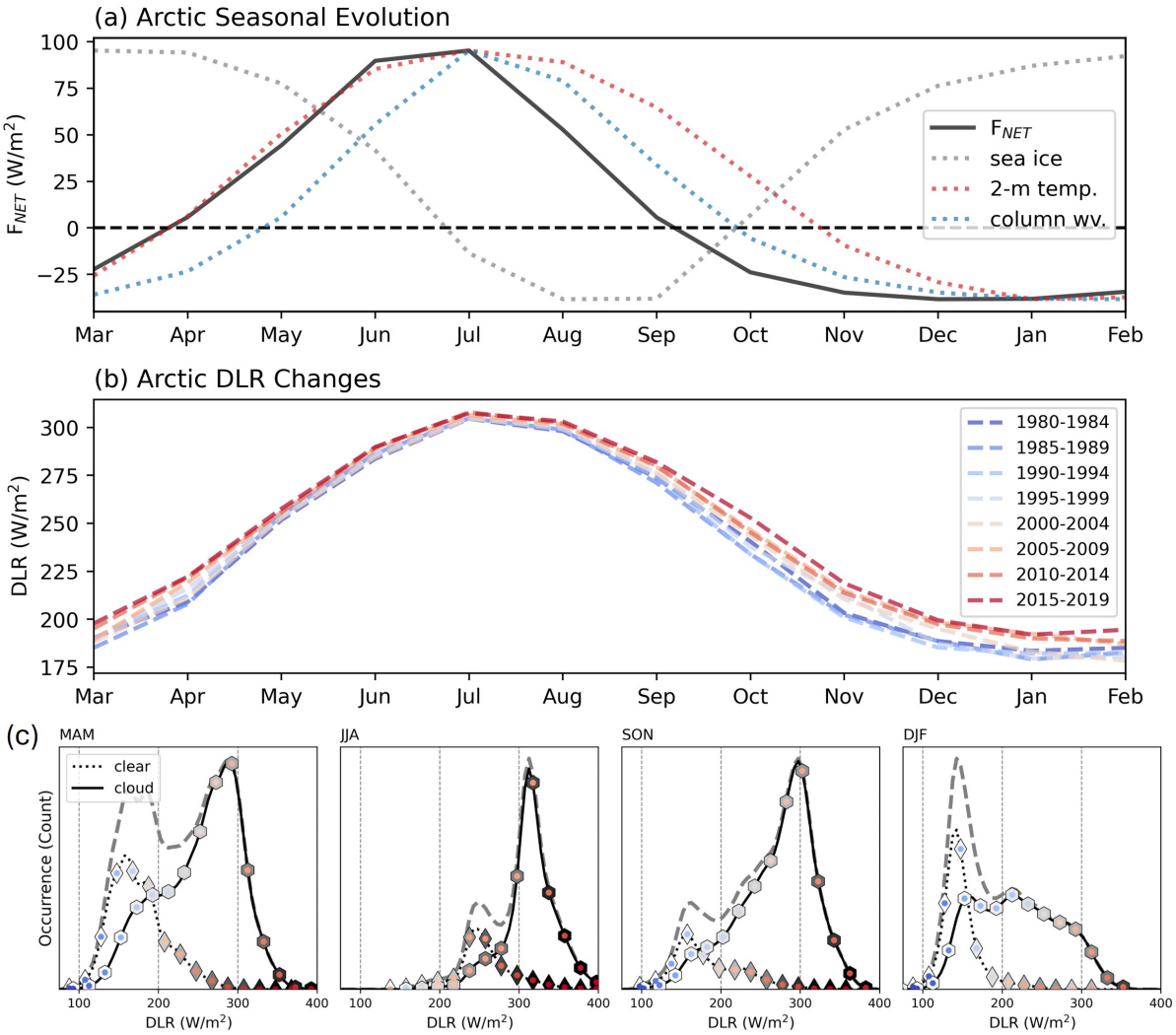

FIGURE 4.1: (a) Arctic (poleward of 60 N) climatology of surface net radiation (F_{NET}), sea ice, 2-meter temperature, and column water vapor as determined by 1980-2020 ERA5 monthly data. Positive F_{NET} (above black dashed) is excess energy towards the surface, all other geophysical quantities are plotted on separate axes. (b) 5 year composites of monthly Arctic surface downwelling longwave radiation. (c) Arctic seasonal distributions of DLR as determined by 2007-2010 CloudSat and CALISPO data (Stephens et al., 2002, Winker et al., 2007). Darker colors for diamonds and hexagons indicate higher mean column water vapor for cloud-free and cloudy scenes, respectively. Redder circles within each shape indicate warmer average 2-meter temperatures. Fluxes derive from 2B-FLXHR-LIDAR (Henderson et al., 2013), cloud presence from 2B-CLDCLASS-LIDAR (Sassen et al., 2008), and geophysical quantities from ECMWF-AUX (Partain, 2004).

due to higher clear-sky emissivities (Curry et al., 1995, Serreze et al., 2012, Ghatak and Miller, 2013, Vihma et al., 2016). However, to what degree is the changing climate modifying the two documented Arctic states? While current conditions promote the existence of a transmissive state and an opaque state, the processes connected to these states are non-linear. Therefore, a small change in the local environment (for example, sea ice extent) may lead to a relatively large change in the prevalence of one state versus the other, and thus, the shape of DLR distributions.

Given the ubiquitous nature of these states, and their dominant role on the surface energy budget, it is important to understand how the two states evolve with the climate. The purpose of this study is to elucidate how Arctic DLR distributions have changed over the observational record. Specifically we are interested in changes related to the modality of distributions, indicating the evolving presence of multiple preferred states. This study focuses on the western Arctic where the two states were first identified from the SHEBA (Surface HEat Budget of the Arctic ocean) campaign (Uttal et al., 2002, Stramler et al., 2011a). This region is within the large 'Central Arctic' cluster presented in Chapter 2. The western Arctic is particularly interesting since it is a major moisture transport pathway (Liu and Barnes, 2015, Gimeno et al., 2019, Papritz et al., 2022) and has experienced enhanced changes in sea ice cover (Vihma, 2014), meaning local and non-local processes are important to the evolution of the two states.

4.2 Data

The Department of Energy's Atmospheric Radiation Measurement (ARM) North Slope of Alaska (NSA) site at Utqiagvik (formerly known as Barrow), Alaska, offers some of the most persistent measurements of the Arctic state (Stamnes et al., 1999). Numerous studies of Arctic weather and climate have relied on products generated from this site's measurements (Kay et al., 2008, Dong et al., 2010, Shupe, 2011, Zhang et al., 2022, Cox et al., 2023) and measurements are likely to continue into the future. The general climatology of the North Slope is found to be well representative of the wider western Arctic and strongly influenced by surrounding sea ice behavior (Cox et al., 2016) indicating that these findings are relevant beyond the single site. Furthermore, considering the clustering behavior in Chapter 2, we may be able to connect these findings to the broader Central Arctic region.

The ARM-NSA site hosts nearly 60 instruments monitoring atmospheric and surface conditions, aerosols, and cloud properties. Among these, DLR measurements are obtained using a sky radiometer on a stand (Andreas et al., 2018), providing a direct measure of incoming thermal radiation. For this analysis, hourly averages of quality controlled DLR data are used (Riihimaki et al., 2024). Even in challenging winter conditions, the average uncertainty associated with these measurements are on the order of 1-3 W/m^2 (Marty et al., 2003, McArthur, 2005, Cox et al., 2020). An hourly sampling frequency preserves variability and prevents averaging of the two distinct states, which may occur with daily

or monthly averages. Analysis excludes the partially filled first (1998) and last (2024) years, resulting in 25 years of data (1999–2023).

4.3 Results

4.3.1 Trends over the ARM-NSA Observational Record

Trends in DLR from the ARM-NSA station for 1999-2023 are shown in Fig. 4.2. Significant positive trends in DLR are observed across all seasons, with magnitudes varying by season. For example, the transition seasons exhibit larger positive trends, particularly autumn (8.0 W/m^2/decade), while summer exhibits the smallest positive trend (3.3 W/m^2/decade). All seasons, especially winter, experience large interannual variability in DLR. Summer has the largest mean DLR, aligning with when Arctic temperature and moisture are largest, while winter has the lowest mean DLR. Autumn mean DLR exceeds spring by approximately 50 W/m^2, due to increased atmospheric moisture, temperature, and high cloud fractions (Serreze et al., 1995, Dong et al., 2010).

Figure 4.2 (right column) provides a first look at how enhanced trends in DLR may be driven by the behavior of the two individual states. Histograms are constructed using observations from the NSA station during the first five years (1999–2003; gray bars) and the final five years (2019–2023; black bars) of each season on record. The mean DLR for each time period are also provided. Compared to the first five years, the final five years on record reveal a shift toward more opaque conditions across all four seasons, though the magnitude of the change varies by season. For example, summer and winter show smaller

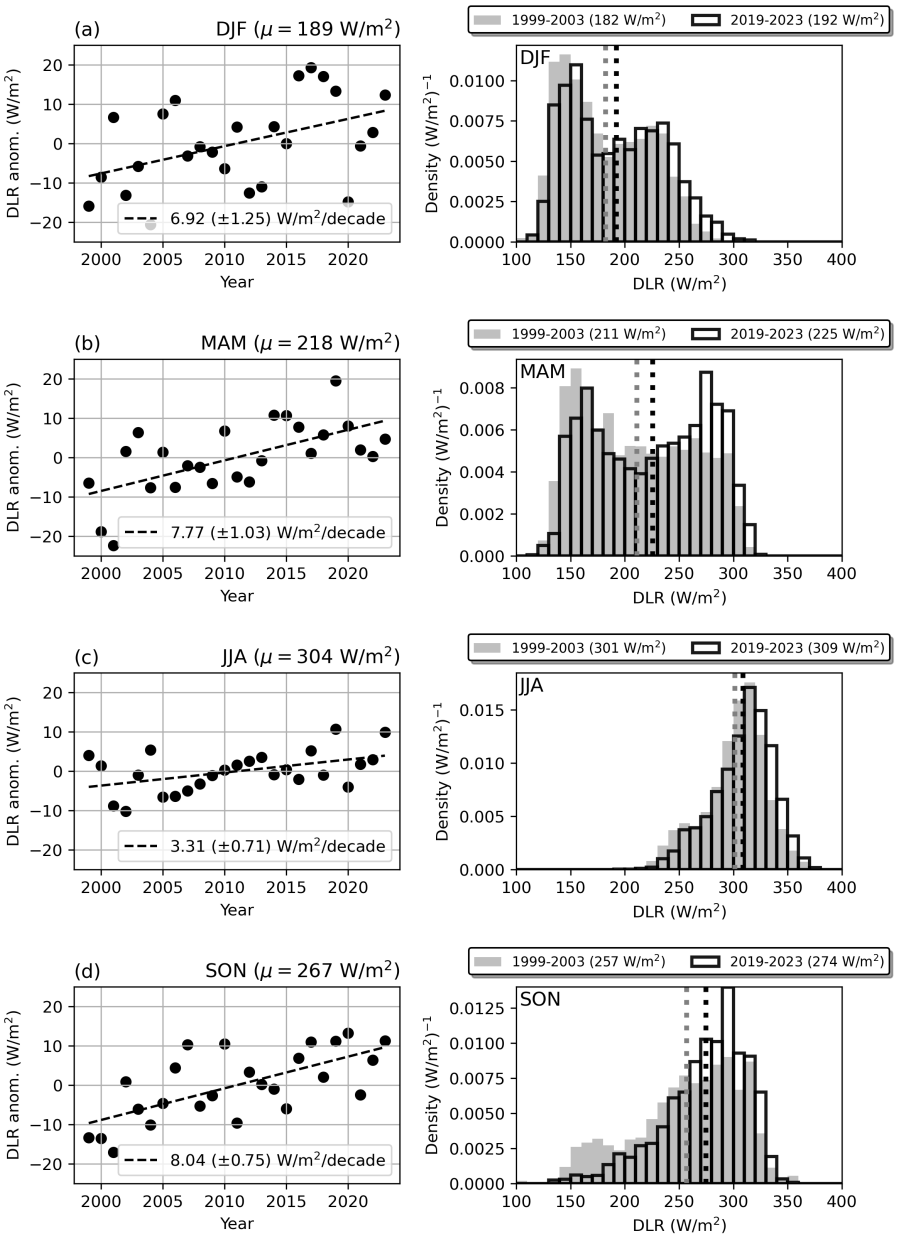

FIGURE 4.2: (left column) Seasonal trends in DLR for the ARM-NSA station from 1999-2023. 95% confidence intervals for the trends are calculated using a jackknife routine. The scatter plot shows anomalies relative to the 1999-2023 mean (listed at the top of each panel). (right column) Histograms of DLR using the first five years (1999-2003; grey bar) and final five years (2019-2023; black line) of ARM-NSA data. Mean values of each five year period are indicated with vertical dotted lines and listed at the top of each panel.

shifts in the mean of the distributions (Fig. 4.2a,c), while the transition seasons exhibit larger changes (Fig. 4.2b,d). The largest shift occurs during autumn with an increase of 17 W/m^2 in the mean of the distribution. These results all qualitatively align with the explicit trend analysis.

How do these changes connect to the behavior of the two states? The relatively small DLR changes in summer and winter are associated with relatively little change in the shape of the distributions as well; that is, the frequency of the clear-sky and opaque state are relatively unchanged. In these seasons, the increase in the mean of the distribution may be mostly attributed to increased clear-sky fluxes driven by increased temperature and moisture. In contrast, larger DLR differences in the transition seasons are also associated with decreases in the transmissive mode and compensating increases in the opaque mode. In autumn, for example, the transmissive mode (approximately 175 W/m^2) merges into the opaque mode (approximately 275 W/m^2) from the historical period to the present-day period; producing a distribution of similar shape to summer. During spring, the opaque mode grows at the expense of the transmissive, resulting in a substantial increase in the mean of the distribution (14 W/m^2; Fig. 4.2b).

4.3.2 A Changing Arctic Autumn

There is particular interest in the Arctic's behavior during autumn, when sea ice begins a rapid regrowth period following its climatological minimum in September (Parkinson et al., 1999, Vihma, 2014, Stroeve and Notz, 2018). Due to its insulating and albedo effects, sea ice has a dominant control on the evolution of the Arctic (and global) climate

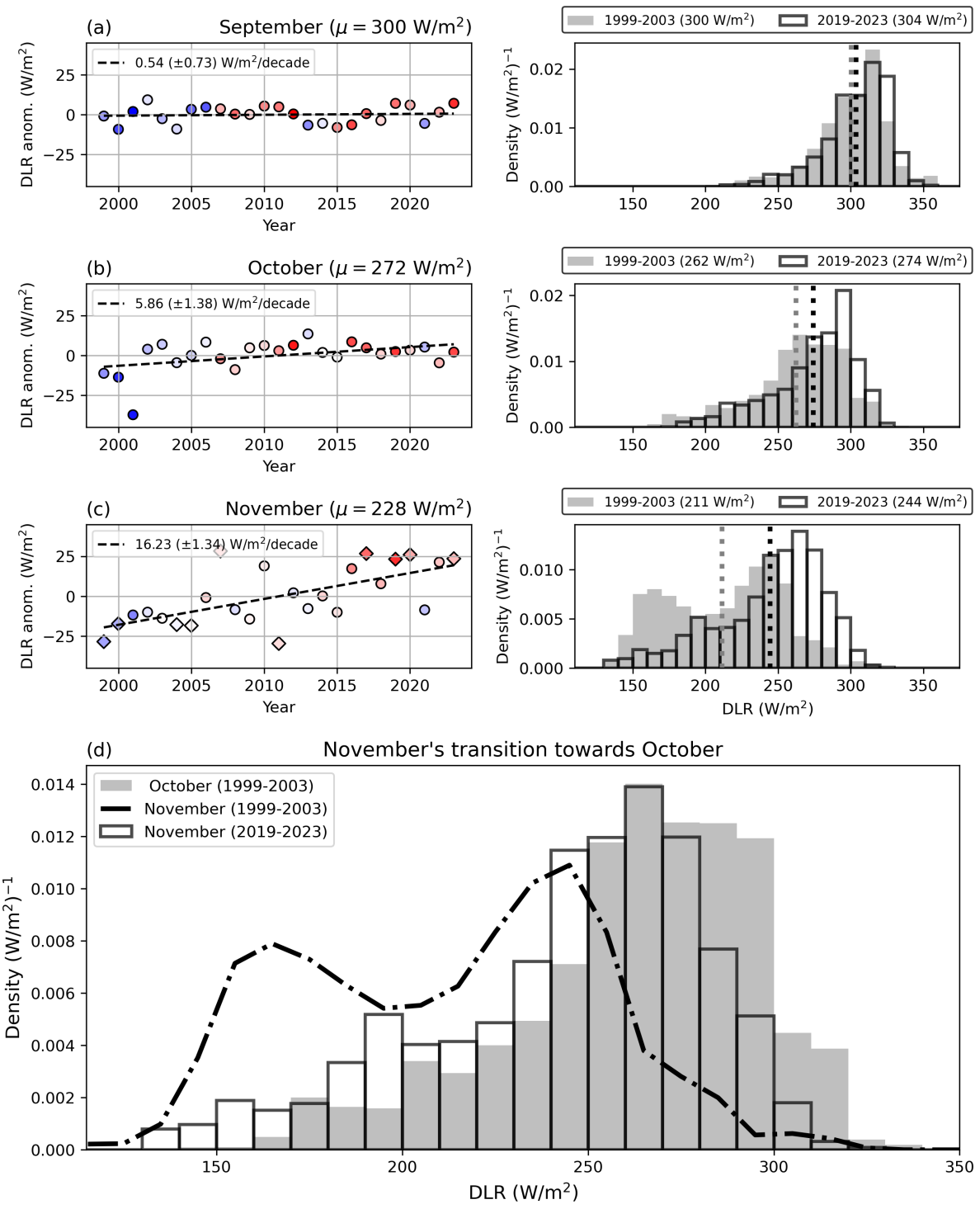

FIGURE 4.3: (a-c) as Fig. 4.2 but for September, October and November individually. Colors on scatter points indicate monthly anomalous sea ice extent for the Chukchi and Beaufort Seas (the two bodies of water immediately surrounding the North Slope) as determined by NSIDC database (C.2; Fetterer et al., 2017), warmer colors are less ice. Colors are equivalent across panels such that the same shades indicate the same absolute differences from the monthly mean. Diamond scatter points in (c) are the five most extreme (high and low) DLR years and are discussed in the text and Fig. 4.4. (d) Comparison showing how November is beginning to resemble past October; discussion in text.

(Taylor et al., 2018). Arctic sea ice is forming later, is less extensive, is becoming thinner and is less persistent than ever before (Stroeve et al., 2012).

Given the influence of sea ice on the Arctic climate, it is important to understand the extent to which the enhanced changes in the Arctic radiative modes exhibited in autumn (Fig. 4.2d) are connected to local changes in moisture and temperature due to evolving sea ice. Morrison et al. (2018) highlights a strong relationship between reduced sea ice extent and increased low-level cloud fraction during autumn in observations, driven by surface-atmosphere coupling, which is further supported by Community Earth System Model version 1 (CESM1) simulations (Morrison et al., 2019). Arouf et al. (2024) demonstrate that reduced Arctic sea ice increases the magnitude of low-level clouds' CRE_{LW} due to increased cloud water path, with November distributions being particularly sensitive to sea ice concentration.

Thus, reduced sea ice not only drives increased cloud cover but, specifically, clouds with larger radiative effects due to increased opacity. By November, solar insolation at the North Slope is near zero (Maykut and Church, 1973). This means that the warming influence of optically thick clouds dominates, as there is little to no compensation in shortwave reflectence. These optically thick clouds promote a strong positive feedback loop as they warm the surface, delay freezing, and further sustain a warm, moist atmosphere conducive to additional cloud formation (Kay and Gettelman, 2009, Yu et al., 2019).

We repeat a similar analysis as Fig. 4.2 but for September, October, and November individually (Fig. 4.3). The historical period for these three months show the transition

from a relatively warm, moist, and cloudy Arctic in September to a relatively cold, dry and cloud-free Arctic in November and how this influences the shape of each DLR distribution. Historically, the ARM-NSA station almost entirely existed in the 'opaque' state during September (Fig. 4.3a). In contrast, by November, sea ice had typically refrozen and the atmosphere tended to be drier and colder. This inhibits low-cloud formation and thus promoted the formation of the transmissive mode (Fig. 4.3c, historical period).

However, across all three months, the mean of each DLR distribution has shifted toward higher values from the first five years to the final five years, though the trend for September is not statistically significant. The increase in mean DLR for November is nearly three times greater than October and eight times greater than September. The pronounced shift in November appears tied to the decline of the transmissive mode highlighted earlier in Fig.4.2, becoming particularly evident in this month (Fig.4.3c). In contrast, September, which already historically existed in a near-permanent 'opaque state' (i.e., lacking cloud-free conditions), shows a relatively small shift in DLR despite experiencing the largest changes in other climate variables, such as sea ice extent (Cavalieri and Parkinson, 2012).

4.3.3 Drivers of Extreme DLR Years

In October and November, years with higher DLR values are generally associated with lower sea ice extents, suggesting a connection between the two geophysical quantities (Fig. 4.3b,c). To further elucidate the processes contributing to enhanced changes in DLR, the broader climatological context of the five most extreme DLR Novembers (i.e., upper and lower DLR quintiles) during the ARM-NSA record are compared (Fig. 4.4 left

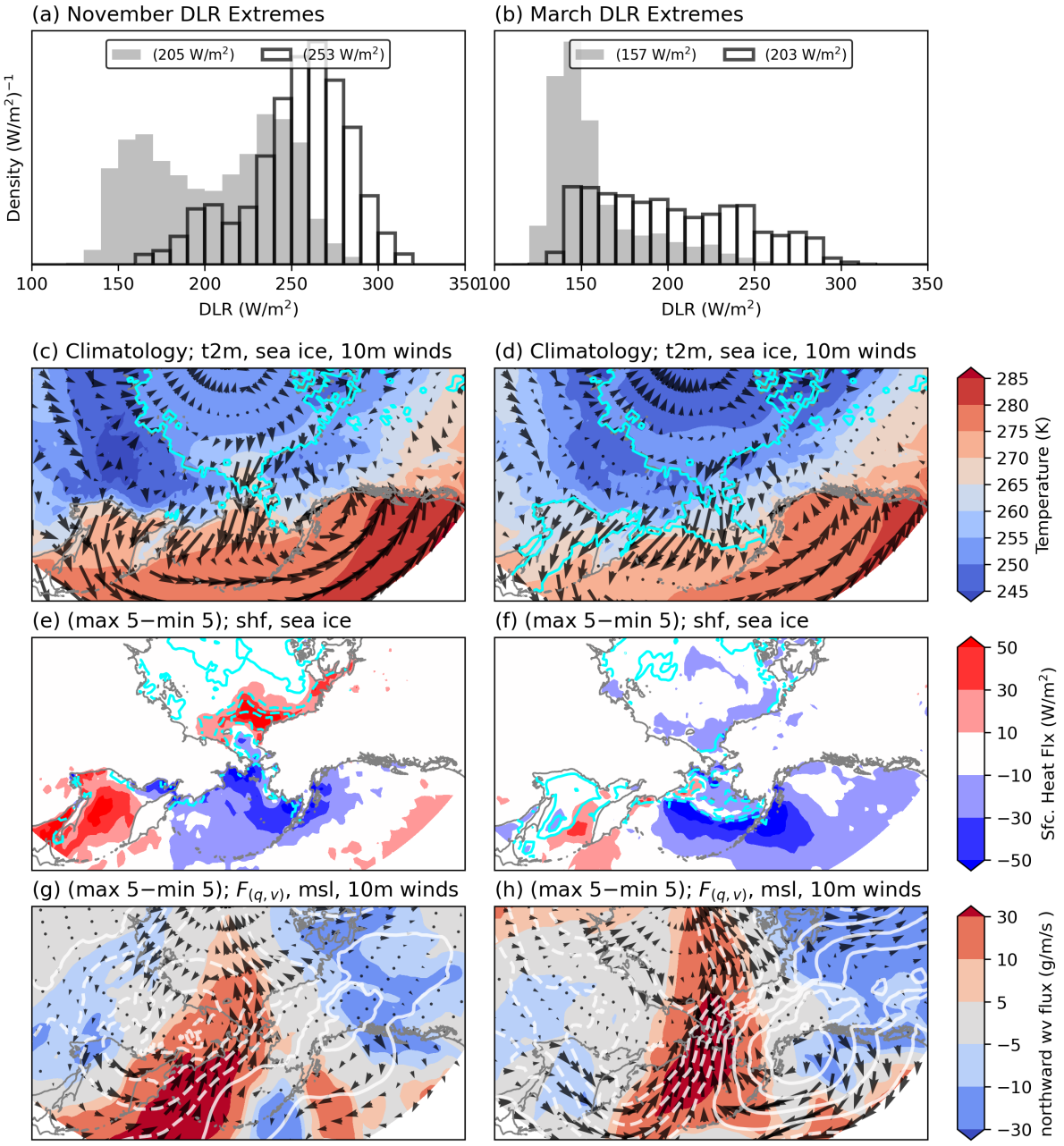

FIGURE 4.4: 5-year extreme DLR composites for November (left) and March (right). Extreme DLR years in November include: 2011, 1999, 2005, 2004, 2000 (lower quintile) and 2019, 2023, 2020, 2017, 2007 (upper quintile). Extreme DLR years in March include: 2012, 2008, 2006, 2001, 2009 (lower quintile) and 2014, 2002, 2023, 2018, 2019 (upper quintile). (a,b) PDFs of DLR for both 5-year periods at ARM-NSA location. (c,d) ERA5 climatological values from 1980-2020 for 2-meter temperature (colors), $>$ 15% sea ice (blue contour), and 10-meter winds (arrows). (e,f) Difference in surface (sensible + latent) heat fluxes (colors) and sea ice (contours) from 5 maximum DLR years to 5 minimum DLR years. Positive values indicate enhanced fluxes from surface to atmosphere, dashed contours are decreased sea ice. (g,h) Difference in meridional moisture flux (colors), sea level pressure (contours), and 10-meter winds (arrows) from 5 maximum DLR years to 5 minimum DLR years. Contour intervals are every 2 mb, dashed contours indicate negative values.

column). Low DLR years are associated with a large transmissive mode while high DLR years are associated with predominately an opaque mode(Fig. 4.4a).

Greater sea ice extent in the Chukchi Sea and along the northern Alaskan coast promotes a more robust transmissive mode leading to lower mean DLR (Fig. 4.4e). Decreases in sea ice increase surface heat fluxes by over 30 W/m^2. These changes are linked to increased moisture and heat fluxes from the surface to the atmosphere, which enhance clear-sky fluxes and cloud frequency (Morrison et al., 2018). Accompanying these local changes, there is enhanced long range transport of water vapor and heat from the lower latitudes through the Bering Strait (Fig. 4.4g). Note that regions of reduced latent heat flux in Fig. 4.4e do not indicate a reversal of direction, just a decrease in magnitude. This reduction may result from a combination of factors: (1) lower near-surface wind speeds compared to climatology, which diminish turbulent fluxes, and (2) anomalous transport that reduces the surface-to-atmosphere gradients in moisture and temperature, thereby lowering flux magnitudes.

March also exhibits large and significant trends in DLR over time (12 W/m^2; Fig. C.1). However, unlike November, Arctic sea ice extent is at its maximum in March and has experienced relatively little decline over the observed record (Cavalieri and Parkinson, 2012). Thus, unlike November, changes in DLR during March have little association with direct changes in local moisture supply. As a means of comparison, extreme DLR years for March are provided in Fig. 4.4 (right column). Minimum years in DLR correspond to nearly entirely the transmissive mode while higher years are more evenly dispersed

(Fig. 4.4b). Climatologically, the mean behavior in March is similar to November but the 10-meter winds are generally weaker, land surfaces are warmer, oceans slightly colder, and the sea ice is more extensive (Fig. 4.4d). Corresponding with more sea ice and weaker surface-to-atmosphere gradients, climatological surface heat fluxes are decreased compared to November (not shown).

Unlike November, sea ice extent does not appear to be a driver of DLR in March. Local changes in sea ice and associated surface heat fluxes are small (Fig. 4.4f). However, 10-meter wind differences are larger, as are the associated magnitudes of meridional water vapor transport (Fig. 4.4h). Anomalous northward water vapor transport occurs over much of western Alaska, including the North Slope. This pattern suggests that non-local transport of heat and moisture (associated with, for example, cyclone activity) may play a more important role in the observed DLR differences in March compared to November, as might be expected (Dai, 2023).

4.4 Conclusions

Larger changes in DLR over time can be connected to changes in the modality of DLR distributions, explicitly the decrease of a transmissive mode, indicating the declining presence of cloud-free conditions in the Arctic. This is exhibited in November in particular, which over the last 30 years has experienced the largest monthly mean increase in DLR at the ARM-NSA station, associated with an almost complete disappearance of the transmissive atmospheric state.

Multiple factors, beyond the existence of a (once) large transmissive mode, make November particularly sensitive to changes in DLR. In autumn, the warm, moist ocean strongly contrasts with the cold, dry atmosphere, creating large thermal and moisture gradients at the surface. These gradients drive turbulent fluxes, reduce lower tropospheric stability, and promote low-level cloud formation (Kay and Gettelman, 2009, Taylor et al., 2015). Sea ice, however, acts as a barrier to this coupling, suppressing the development of optically thick low-level clouds (Taylor and Monroe, 2023). That is, delayed sea ice freeze fosters increased optically thick clouds, which enhances DLR and further delays sea ice growth (Francis et al., 2005, Liu et al., 2012). Since shortwave insolation is near zero by November, there is little compensating albedo effect, further promoting a warming positive feedback.

Although sea ice has also declined in other seasons, such as summer, the ocean-atmosphere coupling is generally weaker (Morrison et al., 2018). Strong surface coupling in autumn amplifies the local DLR response, supplementing the broader non-local forcing observed in other months. Additionally, reduced sea ice in autumn may intensify baroclinic cyclones, further driving long-range atmospheric transport (Rinke et al., 2017). Thus, the locally enhanced surface fluxes during autumn contribute to both direct and indirect positive feedback mechanisms linked to DLR.

These findings indicate a significant shift in the Arctic climate over the past 25 years, where a truly transmissive state in November is becoming increasingly rare. Such transmissive conditions are ultimately what promotes the shedding of excess energy at the

surface and the formation of ice. For context, the global mean direct radiative forcing caused by greenhouse gas emissions has increased by approximately 1 W/m^2 since 2000 (Butler and Montzka, 2016). The additional 30 W/m^2 driven by the changing behavior of the radiative modes, integrated over a month, is thus a dramatic forcing on the local climate. This phenomenon underscores the need to study these preferred states closely.

Arouf et al. (2024) suggests that as ice growth continues to be delayed, future Novembers in the Arctic will resemble present-day Octobers due to enhanced longwave forcing of clouds. This study supports that claim, further asserting that this shift is already evident in historical data from the ARM-NSA station. Explicitly, the distribution of November data from the final five years of the ARM-NSA record closely resembles that of October's first five years (Fig. 4.3d). Connected to this, western Arctic November sea ice extents at the end of the record are near October extents at the start of the record (Fig. C.2).

The signal of November approaching October may be delayed into the future further north, as sea ice is less variable and the feedback with clouds becomes weaker. The 2024 launch of EarthCARE (Earth Clouds, Aerosols, and Radiation Explorer; Illingworth et al., 2015) marks an advancement in our ability to monitor the evolving behavior of DLR distributions, extending beyond the limited number of long-term station measurements. Featuring radar and lidar instrumentation similar to those on CloudSat and CALIPSO, EarthCARE allows for continuity in observing these distinct radiative regimes throughout the high latitudes. With an expected lifetime of three years, EarthCARE offers a unique

opportunity to investigate how these radiative states have evolved Arctic-wide, from the start of the CloudSat and CALIPSO era in 2006, to more than two decades later.

Chapter 5

Evolution of Arctic Radiative States: A Modeling Perspective

5.1 Preface

The previous chapter has shown that the North Slope of Alaska exhibits a robust increase in DLR over the last 25 years. Enhanced changes in DLR can be connected to the changing behavior of the two preferred radiative states. However, this begs the question: how representative is this of the wider Arctic?

While one may use the evolution from past to present to map the trajectory of the two states, the relatively young and sparse observational record in the polar regions, coupled with its high interannual variability, makes testing the representativeness of trends thus far a difficult endeavor. Furthermore, since the Arctic climate system is highly non-linear, understanding if that trajectory will remain constant into the future can be difficult.

Alternatively (or, complimentary), one can use climate models to examine the trajectory of the climate system, explicitly projecting its behavior into the future under a standard forcing scenario (Randall et al., 2007). However, due to their computational cost, climate models are often spatially and temporally coarse. Furthermore, since clouds are largely parameterized, climate models are known to have trouble accurately producing cloud fields (Kay et al., 2016, Taylor et al., 2019). As mentioned, cloud frequency, phase, and height are dominant controls on these two states, thus using a system with well-documented deficiencies related to these factors likely poses issue.

These shortcomings are evident in Fig. 5.1, which compares seasonally observed Arctic surface downwelling longwave radiation distributions to output from the frequently used

Community Earth System Model version 2 (CESM2; Danabasoglu et al., 2020). In all seasons, the unique bimodal structure associated with the two preferred states is evident in observations. CESM2 exhibits large discrepancies, not only compared to the fully observed probability density function (PDF), but also in the mean of the distribution, consistently under-representing the more transmissive mode associated with clear-sky fluxes. Two reanalysis products are also offered for comparison: the European Centre for Medium-range Weather Forecasts Reanalysis 5 (ERA5; Hersbach et al., 2020) and the Arctic System Reanalysis version 2 (ASRv2; Bromwich et al., 2018), the latter being an Arctic specific product. Similar to CESM2, even reanalysis products struggle to capture the complete behavior of the observed PDFs; this is in part due to the high dependency on model components stemming from sparse observations.

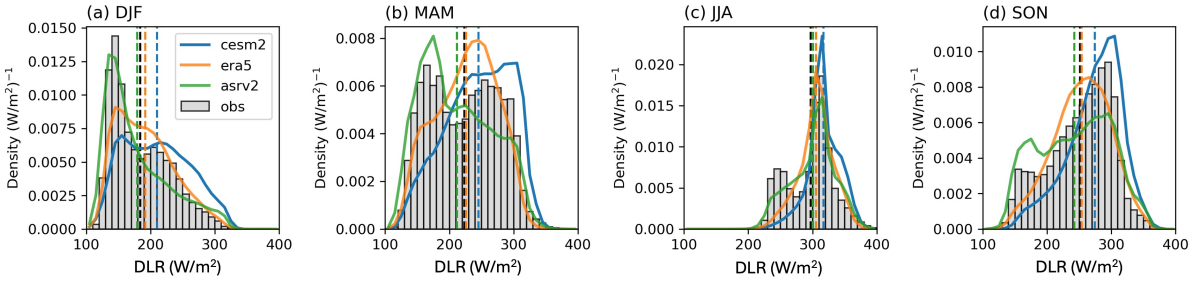

FIGURE 5.1: Comparisons of surface downwelling longwave radiation (DLR) for CESM2, ERA5 and ASRv2 to observations. Observations are determined from CloudSat-CALIPSO's 2B-FLXHR-LIDAR product which can sample surface fluxes with high accuracy (see text discussion). CloudSat was fully operational from 2007-2010, so only those four years for each product and dataset are shown for comparison. PDFs are built from gridboxes or observations which reside within this study's model domain (see Fig. 5.2a), native resolutions of each product are not altered.

There are several commonly used methods to compensate for these limitations with climate models, one being dynamical downscaling. Dynamical downscaling uses a limited-area, high-resolution model (sometimes referred to as a regional climate model, RCM)

whose boundary conditions are driven from a global climate model (like CESM) to derive smaller-scale information (Giorgi and Mearns, 1991). RCM have the added benefit of being able to be specified toward processes which most influence the domain of interest. For example, the Polar-optimized version of the Weather Research and Forecasting model (PWRF) is designed to better capture polar conditions, such as ambient aerosol concentrations and heat transfer over ice, and is not necessarily intended for global use (Hines and Bromwich, 2008). The previous chapter showed that ASR, which is built on PWRF, tends to exhibit the presence of the two states the best out of three reanalysis products evaluated; though deficiencies are still present. This is further exhibited in Fig.5.1, where ASR exhibits the emergence of two modes, albeit not perfectly. Naturally, this indicates the potential usefulness of dynamical downscaling within this context, specifically through the use of PWRF, though, modifications will likely still be necessary.

Thus, the purpose of this chapter is to understand if PWRF can act as a useful RCM to study the current and future behavior of these radiative states. We use the observed rapid decline of transmissive conditions in November from the previous chapter for comparison.

5.2 Methods

5.2.1 Model Description

The polar-optimized version of WRF (PWRF) is used for all model simulations in this chapter (Hines and Bromwich, 2008). Compared to standard WRF, PWRF incorporates enhanced parameterizations for ice, surface processes, and microphysics, making it

TABLE 5.1: PWRF model configuration

Parameter	Selection
Domain	
Horizontal Grid	12.5 km (d01) and 2.5 km (d02)
Dimensions	215 x 215 (d01) and 360 x 360 (d02)
Time step	60 s
Number of Vertical Levels	52
Model Top Pressure	25 hPa
Physics	
Microphysics	P3
Cumulus	Kain–Fritsch (d01)
Radiation	Rapid Radiative Transfer Model (longwave and shortwave)
Planetary Boundary Layer	MYNN 2.5
Atmospheric Surface Layer	MYNN
Land Surface Model	Noah Land Surface Model
Boundary Conditions	
Data	ERA5/ CESM1 Bias Corrected
Frequency	6 hours

better suited for polar environments. These modifications have demonstrated improved performance in simulating both Arctic and Antarctic conditions (Hines et al., 2015, Xue et al., 2022). The model configuration used here employs a one-way nested grid with an outer domain at 12.5 km resolution and an inner domain at 2.5 km resolution. The inner domain explicitly resolves convective processes, meaning no cumulus parameterization is used, in line with model recommendations. That being said, convection is generally less influential at high latitudes. While the chosen grid resolutions are somewhat arbitrary, they do not significantly impact the presented results. Both domains are centered over the ARM-NSA site to facilitate comparisons with long-running observational data from the ground pyranometer.

Figure 5.2 presents distributions of downwelling longwave radiation at the surface (DLR)

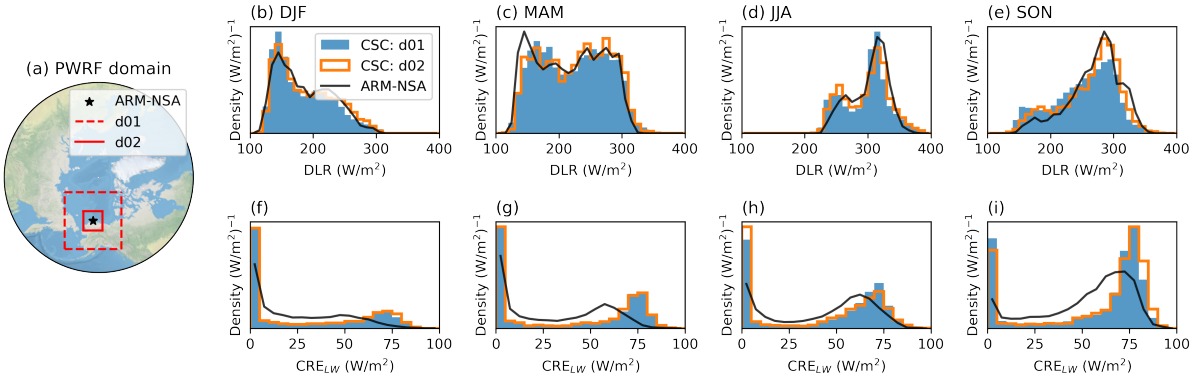

FIGURE 5.2: DLR and CRE$_{LW}$ PDFs for 2007-2010 for the model domain used in this study. (a) The outer domain (d01, dashed), inner domain (d02, solid) and location of the ARM-NSA station (star), to which the two domains are centered on. (b-e) The seasonal distributions of surface downwelling longwave radiation using CloudSat-CALIPSO's 2B-FLXHR-LIDAR product for 2007-2010 for the outer domain (blue) and inner domain (orange). Distributions from ARM-NSA observations for the same years are also provided (black). (f-i) as (b-e) but for longwave cloud radiative effect.

for the described PWRF domain using CloudSat and CALIPSO's 2B-FLXHR-LIDAR, as well as from the ARM-NSA station for 2007-2010. The outer domain, inner domain, and the NSA location have relatively similar PDFs, with bimodality being present in all seasons, highlighting the ubiquitous nature of the states.

Numerical models are sensitive to the choice of parameterization schemes, especially those related to microphysics and boundary layer processes (Taylor et al., 2019, Inoue et al., 2021). Unfortunately there is rarely a 'best model configuration' and one set of parameterizations may outperform another (i.e., more closely match observations) depending on the processes dominating that particular simulation period. Running a full set of simulations with many different parameterization options can be computationally impractical, particularly when developing a pseudo-climatology that requires many simulation days, as is done in this study. Therefore, we depend on prior studies to identify an optimal

set of parameterizations suitable for reproducing a wide range of Arctic conditions. We use the majority of configuration choices from the Arctic System Reanalysis (ASR) version 2 (Bromwich et al., 2018), an Arctic-specific reanalysis product built upon PWRF simulations. ASR has undergone extensive testing and mirrors many of the choices from other PWRF studies (Sledd and L'Ecuyer, 2019, Graham et al., 2019, Cho et al., 2020, Avila-Diaz et al., 2021). Table 5.1 depicts the parameter set used in this study, for further details readers are directed to Bromwich et al. (2018) and the references therein. This set of model configurations serves as a baseline setup, as it has been shown to at least capture the states to some extent.

One main difference from ASRv2, however, is the use of a more advanced microphysics scheme in the two-moment Predicted Particle Properties (P3) scheme (Morrison and Milbrandt, 2015). The Goddard scheme used in ASRv2 is acknowledged to be somewhat dated due to more recent advances in how super-cooled liquid is represented in clouds (Dodson et al., 2021). P3 uses a single ice category represented by four mixing ratio variables: total mass, rime mass, rime volume, and number. The main motivation behind the scheme is to omit the use of relatively arbitrary ice categories (i.e., 'ice' versus 'snow' versus 'graupel') in favor of a continuum. The P3 scheme is found to produce some of the best matches to observations, specifically for clouds containing super-cooled liquid water, which have a strong role in the evolution of the two Arctic states (Bromwich et al., 2009, Listowski and Lachlan-Cope, 2017, Hines et al., 2019, Cho et al., 2020). Furthermore, P3 is indicated as a possible candidate for the next version of ASR (see author discussion in Dodson et al., 2021).

That being said, we test several different parameterization options for a 5-day run and present the results in Fig. 5.3. As previously mentioned, different schemes can, in certain cases, lead to quite different results for a particular simulation. P3 tends to match observed distributions of DLR and CRE_{LW} the best for the subset of simulation days examined. Increasing the vertical resolution of the model has little influence on resulting PDFs, suggesting that is not a limiting factor in the base model setup (indicated by similar PDFs in p3 and p3_{hv}). In contrast, changing the microphysics scheme has a large influence on the evolution of the cloud field, and thus, the PDFs of DLR and CRE_{LW}. Specifically, using the Goddard scheme tends to result in an underdevelopment of opaque clouds, and thus, the opaque mode in DLR. This aligns with ASRv2 which also underrepresents the opaque DLR mode (as seen in Ch. 3 and Fig. 5.1). The Morrison 2-moment scheme, similar to P3, shows potential in the representation of these two states and is also frequently used in the modeling community (Morrison et al., 2005, Hines et al., 2019, Zou et al., 2021). However, ultimately, we decide to use P3 since it is motivated by the next version of ASR and it exhibits a much more distinct opaque mode, which was the main deficiency found in the reanalysis study (Ch. 3).

5.3 Preliminary Results

Given the enhanced sensitivity observed in the previous chapter, coupled with computational constraints, we focus on simulating the behavior of DLR distributions specifically in November. We explore if models exhibit a similar pattern in the decline of the clear-sky mode over time. By focusing on November, there's an added advantage that longwave

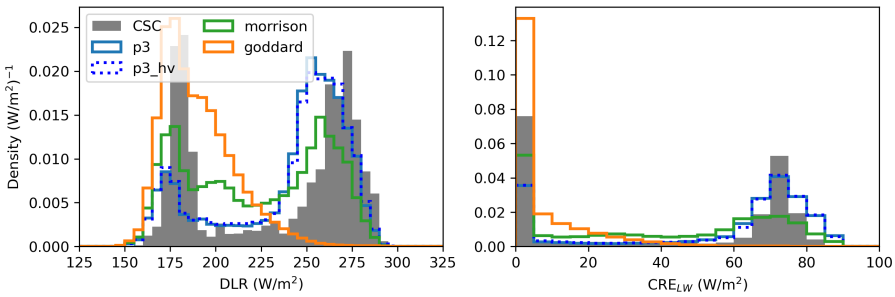

FIGURE 5.3: Sensitivity analysis for different PWRF microphysics and model configurations. PDFs are generated from a single 5-day simulation for November 1-6, 2008 using ERA5 boundary conditions. CloudSat-CALIPSO overpasses that coincide with d02 during this 5 day stretch is used as 'truth' (grey bar). PDFs for the following sensitivity tests are shown for comparison: the 'base' model configuration (Tab. 5.1) (blue solid), increased number of model levels to 75 (blue dashed), substituted P3 for the Morrison double-moment scheme (green), substituted P3 for the Goddard scheme (orange).

radiation constitutes a larger portion of the surface energy balance. This allows our framework based entirely in downwelling longwave radiation to more directly connect with the total energy balance, being less concerned about any potential compensating cloud shortwave effects. We leave the effort of extending this analysis to other months and a greater portion of the Arctic to a future study.

Before analyzing the changing behavior of the states, it is important to first determine whether PWRF, as a system, can accurately simulate observed conditions– specifically, the existence of two preferred states. To simplify this evaluation, we initially set aside the added challenge of assessing how well a climate model can produce realistic present-day forcing conditions necessary for the formation of these radiative states. Explicitly, this is done by forcing PWRF with ERA5 reanalysis data (henceforth referred to as PWRF-ERA5), rather than with conditions generated by a GCM. While ERA5 has its own limitations (discussed in Chapter 3), it is expected to better approximate observed

conditions than a climate model and is commonly used to force WRF. We expect ERA5 to better approximate observed conditions since reanalysis models are constrained by observations to reproduce the Earth system climatology and its historical evolution, while global climate models are often run unconstrained. As a result, the atmospheric state produced by climate models usually does not follow historical evolution and may be a worse match to the observed climatology than that of reanalyses.

5.3.1 Functionality of Polar WRF

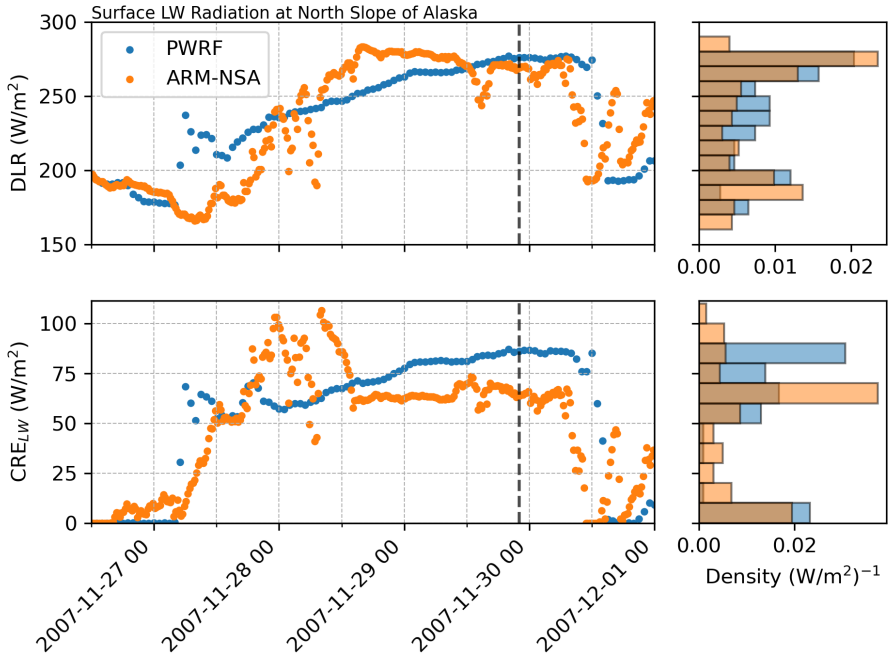

FIGURE 5.4: Example PWRF-ERA5 simulation for November matched to ARM-NSA observations. (a) Timeseries of surface downwelling longwave radiation for PWRF (blue) compared to ARM's pyranometer (orange). (b) Histograms of DLR built from (a). (c,d) as (a,b) but for longwave cloud radiative effect. The timestep depicted with the black vertical dashed line is examined in Fig. 5.5 and discussed in the text.

Figures 5.4 and 5.5 present a sample simulation for November 26-30, 2007, comparing the 2.5 km resolution inner domain to observational data. Fig. 5.4 first presents a timeseries

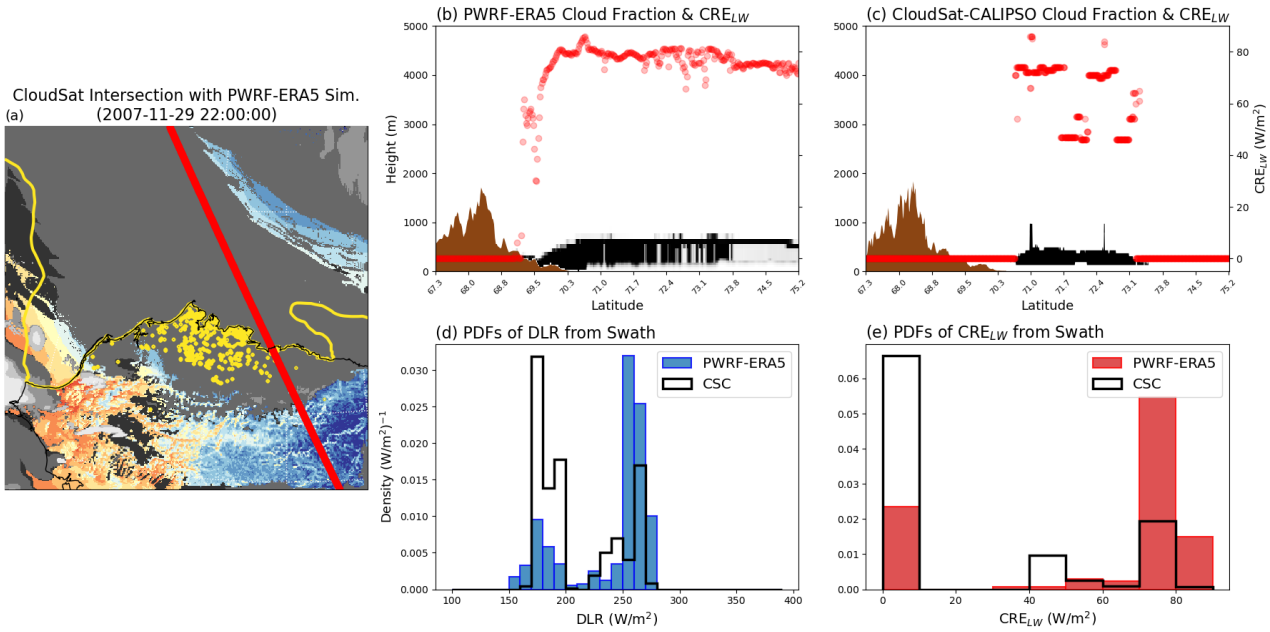

FIGURE 5.5: (a) Example 2d field generated with PWRF-ERA5 for November 29th, 2007 at 22 UTC. Greys and blacks indicate the presence of clouds, while blues and reds indicate surface temperature. Thick yellow line indicates the ice boundary. The red line depicts an intersecting CloudSat & CALIPSO swath that occurred during this time. (b) The 2d cloud mask (black) and 1d CRE$_{LW}$ (red dot) associated with the CloudSat swath according to the PWRF-ERA5 simulation. (c) as (b) but from true CloudSat-CALIPSO observations. (d) PDFs of DLR from the CloudSat-CALIPSO swath according to PWRF-ERA5 (blue) and CloudSat-CALIPSO (black bar). (e) as (d) but for CRE$_{LW}$.

where the nearest gridpoint from d02 is compared to observations at the ARM-NSA station. In this case, PWRF-ERA5 does relatively well in simulating observed conditions. While there are some differences in CRE$_{LW}$ and DLR, the model successfully captures two regime transitions: from transmissive to opaque around 00 UTC on 11-27 and from opaque to transmissive around 12 UTC on 11-30. These regimes persist on the characteristic timescales of a few days. Overall, two distinct modes are evident in both the observations and the model, occurring in similar locations with comparable frequencies, which is ultimately the goal for PWRF in the context of this study.

To gain more spatial understanding of what PWRF is doing, Fig. 5.5 presents a 2D field from 22 UTC on 11-29, during this timeseries (black dashed in Fig. 5.4), matched to a CloudSat & CALIPSO overpass that took place. Low-level liquid containing clouds span from about 70.5 ^{o}N to 73.5 ^{o}N of the observed swath. These clouds have a high CRE_{LW} and thus promote an opaque mode. While similar clouds appear in the model, they cover about double the area as what is observed. That being said, like observations, there are two modes in DLR for the model's PDF. Furthermore, the two modes are located in approximately the same location as the 2B-FLXHR-LIDAR product (Fig. 5.5d). However, due to the model's overproduction of clouds, the opaque mode appears at a disproportionately high frequency in the model's PDF compared to observations. This overproduction of opaque clouds is surprising considering all reanalysis products examined in Chapter 3 exhibited the opposite problem.

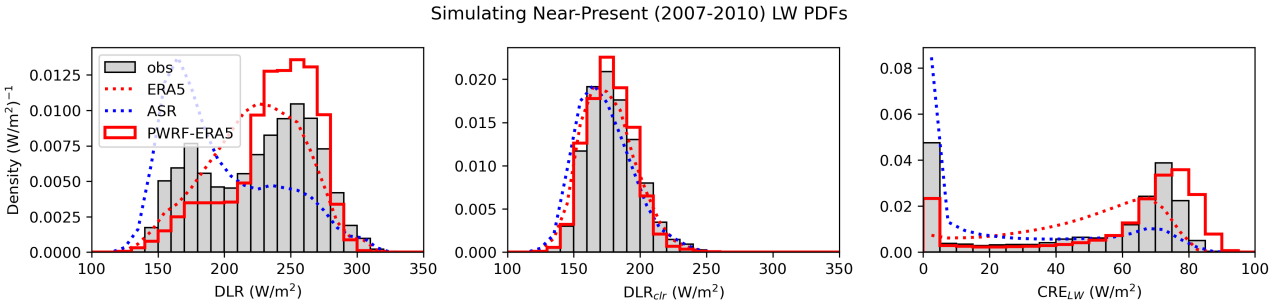

FIGURE 5.6: 2007-2010 PDFs of DLR, DLR_{clr} and CRE_{LW} for d02 of the model study. PDFs are generated using CloudSat and CALIPSO 2B-FLXHR-LIDAR (gray bar), ERA5 hourly data (red dotted), ASR 3-hourly data (blue dotted), and PWRF-ERA5 hourly data (red solid).

We now explore how well PWRF-ERA5 can simulate the two observed DLR modes in a more systematic manner. Fig. 5.6 presents November PDFs of DLR, DLR_{clr}, and CRE_{LW} simulated by PWRF-ERA5 for 2007-2010 (four years), compared to CloudSat-CALIPSO

observations. This climatology is generated by simulating the first and final five days of November for each year, using hourly output. The first 24 hours of each simulation period are removed for spin-up, which is standard for PWRF simulations (Wilson et al., 2011, Hines et al., 2019). By focusing on just the first and final five days of November, we capture the range of DLR conditions (maximum and minimum) for November (Fig. D.1) while also conserving computational resources. This approach enables simulations across more years, allowing us to better capture inter-annual variability.

Apparent in Fig. 5.6 is a systematic overproduction of clouds that appeared in the example swath (Fig. 5.5). The overproduction of clouds, and the infrequent realization of a true 'clear-sky', seems to be a common occurrence in Arctic regional climate models (Tjernström et al., 2008), and specifically in PWRF (Bromwich et al., 2009, Hines and Bromwich, 2017). The reasons for this are variable, but are likely associated with improper interactions with the surface at the lowest model level, specifically over cold ice-covered surfaces.

These misrepresentations over ice-covered surfaces are clearly illustrated by comparing vertical profiles of cloud fraction and distributions of CRE_{LW} over ocean and ice-covered surfaces in observations versus PWRF-ERA5 simulations (Fig. 5.7). As expected, and consistent with previous studies (Morrison et al., 2018, Arouf et al., 2024), observations show that cloud frequency is generally lower over ice-covered surfaces compared to ocean-covered surfaces, resulting in a much larger proportion of scenes with CRE_{LW} near 0 $\mathrm{W/m^2}$. However, PWRF simulations depict higher cloud fractions near the surface over

sea ice than over the ocean. In fact, the mean cloud frequency over ice surfaces in PWRF approaches 100%, compared to 95% over ocean surfaces (not shown). Ultimately this leads to a reversal of what is observed, with scenes where CRE_{LW} is approximately 0 $\mathrm{W/m^2}$ becoming more common over the ocean than over sea ice. Ocean scenes exhibiting higher cloud frequencies in PWRF than what is observed only further promotes the absence of clear-sky conditions.

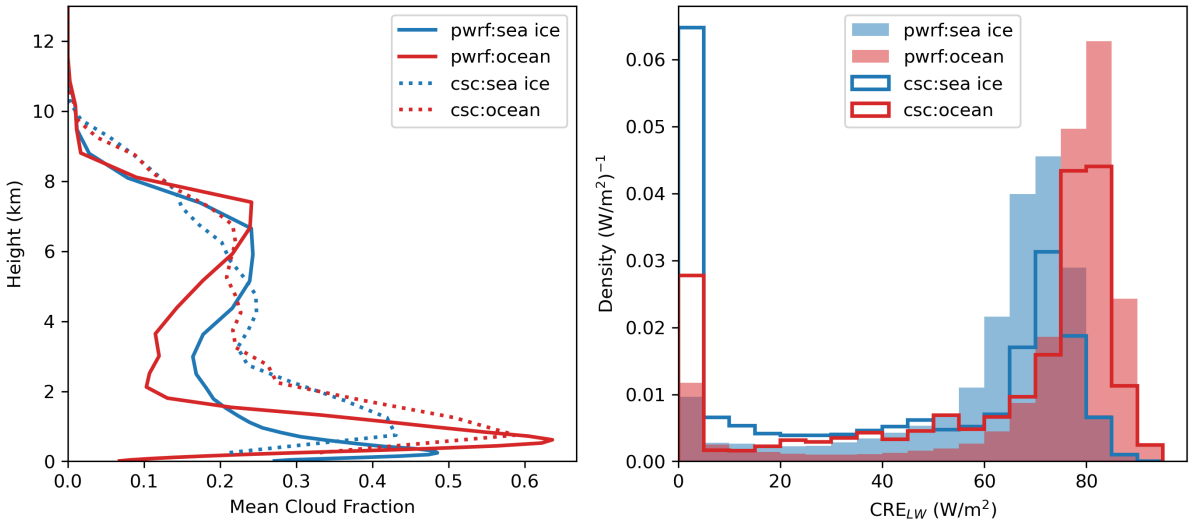

FIGURE 5.7: (a) Vertical cloud fraction for 2007-2010 according to PWRF-ERA5 simulations (solid line) and CloudSat-CALIPSO observations (dashed line) for d02. Mean cloud fractions are separated by sea ice covered (blue) and ocean covered (red) surfaces. (b) Longwave cloud radiative effect distributions separated by surface type for PWRF-ERA5 distributions (solid bar) and CloudSat-CALIPSO observations (outlined bar).

Currently, the dramatic overproduction of clouds by the current model setup is a limitation for using PWRF to study the changing Arctic. The rapid decline of a clear-sky mode is fundamental to the enhanced changes in November's DLR exhibited in Chapter 4. By lacking such a mode in the first place, it is difficult to show how this decline will occur elsewhere into the future. That being said, encouragingly, two modes are present

in PWRF-ERA5 CRE_{LW} PDFs whose locations and individual variability closely match observations. This indicates potential usefulness in PWRF's ability to study the climatological behavior of these states, albeit with some tuning still needed. More work is needed to determine which modifications will produce a simulation with preferred state behavior that more closely matches observations. However, the next section presents some conclusions derived from the work thus far, as well as future work stemming from this study.

5.4 Discussion

5.4.1 Preliminary Conclusions

Accurately reproducing the existence of preferred Arctic radiative states is a challenge for models, and this study is no exception. Here we've evaluated the potential for PWRF to be used as an RCM to study preferred radiative states in the western Arctic. While further refinement is needed, PWRF shows promise, capturing cloud radiative modes with magnitudes that closely match observations, though their frequency is misrepresented. Considering the prevalence of these radiative states, addressing the driving factors that lead to the misrepresentation of the states' frequency offers an opportunity to enhance PWRF's ability to model the complete Arctic climate further.

By adopting a setup similar to that of the operational ASR, we assess the potential impact of using a more advanced microphysics scheme. Specifically, we compare the performance of the P3 scheme, a candidate for ASRv3, to the Goddard scheme used in

ASRv2. Our findings reproduce the known tendency of the Goddard scheme to overproduce the transmissive state while underrepresenting opaque cloud occurrences (Ch 3). Conversely, replacing it with the P3 scheme results in the opposite issue, with an overrepresentation of the opaque state. This is perhaps linked to cloud longevity and optical depth differences stemming from P3's ice continuum strategy, though more investigation is needed.

Improper sensitivity to surface conditions seems to at least partially drive the overproduction of the opaque state in the current PWRF setup. Observations and previous studies indicate that sea ice is a deterrent to cloud formation, which the model does not currently mimic. To better capture this relationship, some potential changes to the model set up could be revisited, including the microphysics parameterization or the boundary layer scheme. Insufficient vertical resolution of the model does not appear to be a driving factor for these discrepancies (Fig. 5.3).

Additionally, we demonstrate the advantages of using PWRF with ERA5 as a dynamical downscaler over relying solely on 'raw' ERA5 (Fig. 5.6). PWRF more effectively preserves the distinction between the two CRE_{LW} modes, whereas ERA5 tends to blend them, potentially masking important climatic features. This further promotes that PWRF is a useful tool for refining Arctic cloud and radiative process simulations, making it a valuable resource for future studies on Arctic climate dynamics.

5.4.2 Future work: Forcing PWRF with CESM

If we can refine the model parameterization to better capture clear-sky occurrences, then applying the model to future climate scenarios becomes more meaningful for assessing changes in these states. While PWRF does not systematically capture the properties of the modes as resolved by CloudSat-CALIPSO, it does demonstrate some ability in representing the physical processes that give rise to these modes and in reproducing their overall existence (i.e., the development of both an opaque cloud mode and a transmissive mode). However, it is also possible that current modeling capabilities or our understanding of these processes impose fundamental limitations, and thus, the need for continued model development is necessary to fully capture the changing behavior of these states in the following proposed setup.

A bias-corrected form of CESM1 has been created for the specific purpose of forcing WRF (Monaghan et al., 2014). The applied bias correction is derived from ERA-interim reanalysis and is meant to correct the mean state towards the observed seasonal climatology, while still maintaining the variability produced by CESM (Bruyère et al., 2014). This dataset is widely used by the dynamical downscaling community (e.g., Krayenhoff et al., 2018, Ghanbari et al., 2023). The dataset includes a 20th century simulation with the observed forced response from 1861-2005, followed by three different Representative Concentration Pathway (RCP) scenarios (4.5, 6.0, and 8.5) until 2100. Although CESM produces ensembles to capture the internal variability of the Earth system, only one ensemble member has the complete three-dimensional fields required to force WRF

(member #6, known as the 'Mother of All Runs'; MOAR). That is, we are constrained to the variability produced by this single ensemble member. Henceforth we refer to PWRF simulations forced by this CESM dataset as 'PWRF-CESM'.

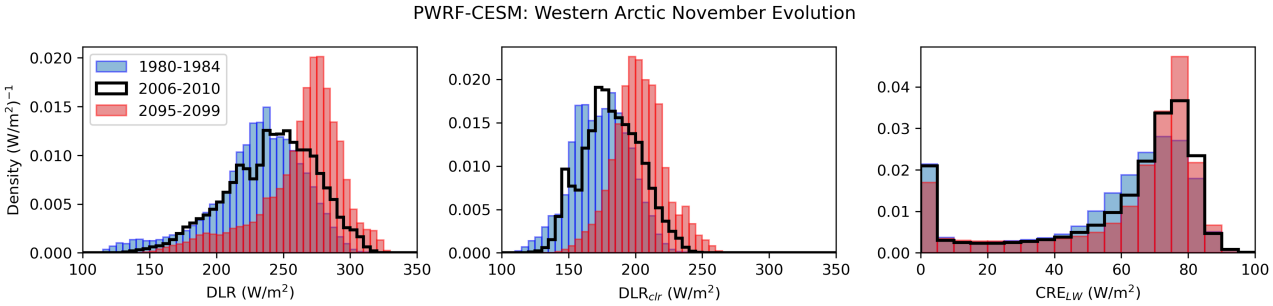

FIGURE 5.8: November PDFs of DLR, DLR_{clr}, and CRE_{LW} for d02 of the model study using PWRF-CESM. Three different 5-year periods are simulated: 1980-1984 (blue), 2006-2010 (black), and 2095-2099 (red).

To produce past, current and future November PDFs, we may take a similar approach as with PWRF-ERA5, but span a greater number of years using the alternate CESM forcing dataset to understand how the states are changing. For example, the first 5 years of the RCP 6.0 simulation (2006-2010) can be used to produce a 'near-present' distribution and the final 5 years of the RCP 6.0 simulation (2095-2099) can be used for a 'future' distribution. The RCP 6.0 forcing represents a 'middle-of-the-road' emissions scenario. Once again, for each year, two sets of 5-day simulations (Nov 1-5 & Nov 26-30) are run. The first 24 hours are removed for spin-up. While 24-hours is typically long enough for the atmosphere to reach equilibrium, slowly evolving processes associated with the surface such as soil moisture, ocean temperatures, and sea ice properties may take much longer (days, weeks, months). While we are focused on the how the atmospheric states are changing, we have shown that surface properties do play a strong role in modulating

the two modes (Ch. 4). Therefore, we will also test running longer simulation periods to understand what effect, if any, longer spin up times have on the results.

Figure 5.8 depicts near-present and future November DLR, CLR_{clr} and CRE_{LW} distributions produced with PWRF-CESM using the suggested approach. In each case, the distinct pattern of bimodal DLR distributions are missing. This is similar to Fig. 5.1, where CESM2 misses the observed bimodality. Even in a historical simulation set (1980-1984), opaque clouds are very frequent (indicated by the large opaque CRE_{LW} mode). This is obviously a deficiency that has persisted from the previous examples. This makes interpreting the results difficult, since, the transition towards more optically thick clouds is the dominant mechanism for enhanced DLR sensitivity in November (Chapter 4). As mentioned, more work is needed to address this kink, however, here we have shown a prepared setup to ingest GCM data once a solution is implemented.

Chapter 6

Synthesis

The Arctic climate is changing more rapidly than anywhere else on Earth, a process known as 'Arctic amplification'. The poles play a crucial role in shaping global climate dynamics by effectively dissipating excess energy received by the Earth's lower latitudes (Budyko, 1969, McGuire et al., 2006, Tomas et al., 2016). Consequently, the energy balance changes associated with Arctic amplification influence weather and climate globally (e.g., Roots, 1989, Kay et al., 2008, Goosse et al., 2018, L'Ecuyer et al., 2021, Sledd and L'Ecuyer, 2021, Prince and L'Ecuyer, 2024).

Several field studies have revealed the existence of two preferred polar radiative states; a transmissive state associated with a relatively large longwave energy deficit at the surface and an opaque state with enhanced atmospheric emission that offsets most of the surface longwave deficit (Stramler et al., 2011a, Graham et al., 2017, Walden et al., 2017, Silber

et al., 2019). The presence of these states significantly modifies the surface energy budget, and thus, the surface temperature and the rate at which ice freezes.

This dissertation has thoroughly examined the existence of preferred polar radiative states initially documented during the 1998 SHEBA campaign, identifying their locations and understanding what controls their behavior. In this final chapter, we summarize the key findings in relation to the research questions introduced in Chapter 1. Additionally, we propose directions for future research on this topic.

6.1 Revisiting Research Questions

1. To what extent are bimodal longwave flux distributions observed across the Arctic and Antarctic? *(Focus area for Chapter 2)*

Bimodal distributions of DLR are ubiquitous across the Arctic and Antarctic. The mean of DLR distributions, and the frequency of each mode, vary largely with season and location. For instance, Greenland often lacks a distinct opaque mode due to its particularly dry and cold climate, which suppresses cloud formation. Though, during the summer, a clearly defined bimodal distribution does emerge. In contrast, the Southern Ocean consistently exhibits a dominant opaque mode, regardless of the season. Regions such as the Antarctic continental boundary and the Central Arctic exhibit more evenly weighted bimodal distributions, with neither mode being overwhelmingly dominant.

The pronounced bimodality in the Antarctic is particularly interesting, considering it has received relatively little attention in the literature. Notably, these bimodal distributions are not solely tied to differing surface types, such as sea ice, ocean, or land; bimodal DLR distributions are observed even when restricted to a single surface type.

2. What processes give rise to bimodal longwave flux distributions, and why are they seemingly unique to the polar regions? *(Focus area for Chapter 2 & Chapter 3)*

Bimodality in longwave flux distributions arises from distinct characteristics of the polar regions. The high latitudes are characterized by cold, dry, and stable conditions, which limit clear-sky emissivity. This is statistically represented by a single, low-variance mode in clear-sky DLR (DLR_{clr}), corresponding to the 'transmissive' mode of DLR distributions. This mode corresponds to either cloud-free scenes or optically thin clouds.

The limited clear-sky emissivity in polar regions means cloud formation often results in a dramatic increase in atmospheric emissivity, significantly enhancing DLR. The longwave radiative effect of clouds (CRE_{LW}) saturates rapidly as clouds approach blackbodies. This saturation occurs relatively quickly with increasing water path and CRE_{LW} is less sensitive to other cloud properties, such as cloud temperature and base height. Both liquid and ice clouds saturate in CRE_{LW}, though ice clouds require higher water paths to reach saturation. As a result, clouds of all phases contribute to the distinct 'opaque cloud mode,' which connects to the higher DLR mode. Thus, a distinct opaque mode in CRE_{LW} is a key factor driving bimodal DLR distributions.

In contrast, at lower latitudes, the relatively high clear-sky emissivity, driven by increased atmospheric water vapor, reduces the magnitude of clouds' CRE_{LW}. Consequently, the opaque mode in CRE_{LW} is absent, and DLR distributions lack the two distinct modes seen in polar regions.

The role of ice clouds contributing to bimodal DLR distributions is not widely presented in the literature. Bimodal DLR distributions are mostly attributed to the presence (or lack thereof) of mixed-phase clouds. However, our findings demonstrate that ice clouds preferentially form in two regimes: optically thin high clouds and optically (and geometrically) thick low clouds. This preferential behavior, coupled with the saturation effect, allows ice clouds alone to generate bimodal DLR distributions.

Considering these findings, capturing the frequency of these two DLR states requires simulating many distinct cloud processes, making it challenging to model. Since DLR is an 'inclusive' variable in the Arctic climate, bimodality in DLR projects onto many other geophysical quantities, such as temperature and moisture. Thus, while simulating DLR distributions is difficult, doing so provides a powerful means to assess the ability of models to represent broader polar processes.

3. How accurately do models, including reanalyses, represent the higher moments of longwave flux distributions? *(Focus area for Chapter 3 & Chapter 5)*

None of the reanalysis datasets examined in this dissertation fully capture the higher moments associated with the two preferred radiative states. This deficiency is primarily

due to the absence of a distinct opaque cloud mode in CRE_{LW}, which limits the existence of the opaque mode in DLR. MERRA2 represents a 'worst-case scenario' that highlights the importance of studying these radiative states. Explicitly, MERRA2 tends to merge the two observed, well-defined CRE_{LW} modes into a single intermediate mode, which results in a single DLR mode as well. This leads to high model skill from a Gaussian perspective, i.e, comparing the mean and variance of distributions to observations, but represents a state that is infrequently realized in nature. This misrepresentation poses challenges for bias correction and for diagnosing deficiencies in model processes.

Even polar-focused products like ASR face difficulties in accurately representing the frequency of the two radiative states. ASR's discrepancies generally stem from differences in cloud phase partitioning, favoring a relative increase in ice clouds over liquid clouds compared to observations, and from differences in cloud water path values.

4. How have these radiative states evolved over time, and how might they change in the future? *(Focus area for Chapter 4 & Chapter 5)*

Using models to understand the evolution of these states has proven difficult, however, long-term observations at the North Slope of Alaska have revealed significant changes in DLR over time. While all seasons show increasing DLR, driven by higher clear-sky fluxes associated with rising atmospheric temperatures and moisture, the transition seasons exhibit particularly pronounced changes. These larger shifts are linked to an increase in the frequency of the opaque DLR mode at the expense of the transmissive mode, indicating that opaque clouds are becoming more prevalent.

November experiences particularly large changes, with the transmissive mode almost entirely disappearing in the past 25 years. These enhanced changes are closely tied to local increases in atmospheric moisture, driven by reduced sea ice extent, and is complemented by enhanced non-local moisture transport also observed during other months.

The presence of these states across both the Arctic and Antarctic, along with their connection to large shifts in DLR (i.e., a rapid decrease in one mode), underscores the need to recognize and study them. In particular, model evaluation methods should not solely assume Gaussianity. An example alternative could be employing a two-mode Gaussian mixture model, which may provide a more representative approach while remaining relatively simple. Accurately capturing the evolution of these states is likely essential for skillfully representing the polar climate as a whole.

6.2 Future Work

This work has blossomed into something much greater than I had originally imagined. With each question answered, more seemed to pop up. Here, I will briefly highlight a few future directions that interest me and naturally extend from the findings presented in this dissertation.

What are the spectral properties of these radiative states?

Thus far, we have examined the broadband longwave properties of these states. However, are there unique spectral signatures associated with them? For example, what role does

the mid-infrared versus far-infrared have? Cox et al. (2015) suggests that while the mid-infrared predominantly determines the existence of the opaque cloud mode in CRE_{LW}, the far-infrared modifies the location of that mode. For instance, the far-infrared window tends to remain 'open' over Greenland, due to its extremely dry conditions, shifting the opaque CRE_{LW} mode to slightly higher values than in locations where the window is 'closed'. Do these findings hold with a broader set of observations? This question aligns well with PREFIRE's objectives (L'Ecuyer et al., 2021), though further examination is needed to determine how effectively DLR can be modeled using PREFIRE's passive TOA measurements.

Is the 'collapse' of the transmissive mode exhibited elsewhere?

Chapter 2 suggests that this signal may also emerge in regions where sea ice is expected to decline. For instance, opaque clouds appear more frequently in scenes classified as ocean rather than sea ice (Fig.2.7). In Chapter 5, we attempted to explore this phenomenon systematically using model simulations. While further refinement of the model setup is necessary for such investigations, this study lays promising groundwork.

Beyond model improvements, we can expand upon the observational analysis in Chapter 4 by incorporating long-term radiation measurements from Svalbard, provided by the Baseline Surface Radiation Network (BSRN; Maturilli et al., 2015). These observations, dating back to August 1992, are similar to those from the ARM-NSA station. While Svalbard shares key environmental characteristics with the NSA station (e.g., significant

non-local moisture transport), it also presents unique features (e.g., being a small island) that may offer additional insights. For example, Svalbard may better represent the moisture intrusion region discussed in Chapter 2, potentially revealing a stronger connection between shifts in transmissive versus opaque conditions and non-local transport mechanisms.

That being said, the final paragraph of Chapter 4 perfectly sums up what I think to be a great future study. CloudSat and CALIPSO observations have been invaluable in mapping the presence of these states across the wider Arctic. While it will take some work to 'degrade' the observations of EarthCare to match that of CloudSat and CALIPSO, repeating this analysis on observations nearly 20 years later would be a great step towards mapping the broader evolution of these states.

How is the morphology of Arctic clouds changing?

Many Arctic clouds are stratus in nature– low altitude, uniform, geometrically thin, and widespread. These clouds are often mixed-phase and sustain themselves through unique dynamical processes that allow for long lifespans in the Arctic (Morrison et al., 2012). However, there is emerging evidence suggesting that, as the Arctic warms, these clouds may shift toward a more stratocumulus-like regime (Eirund et al., 2020). Specifically, Arctic stratus may become optically and geometrically thicker, more organized, and less widespread.

This shift is interesting because it could act as a negative feedback mechanism for these

radiative states. Since CRE_{LW} saturates, increasing the optical thickness of these clouds does little to increase the DLR. However, by reducing the overall area of these clouds, the total energy incident on the surface (when only considering longwave radiation), should decrease.

Appendix A

Supplementary Material for Chapter 2

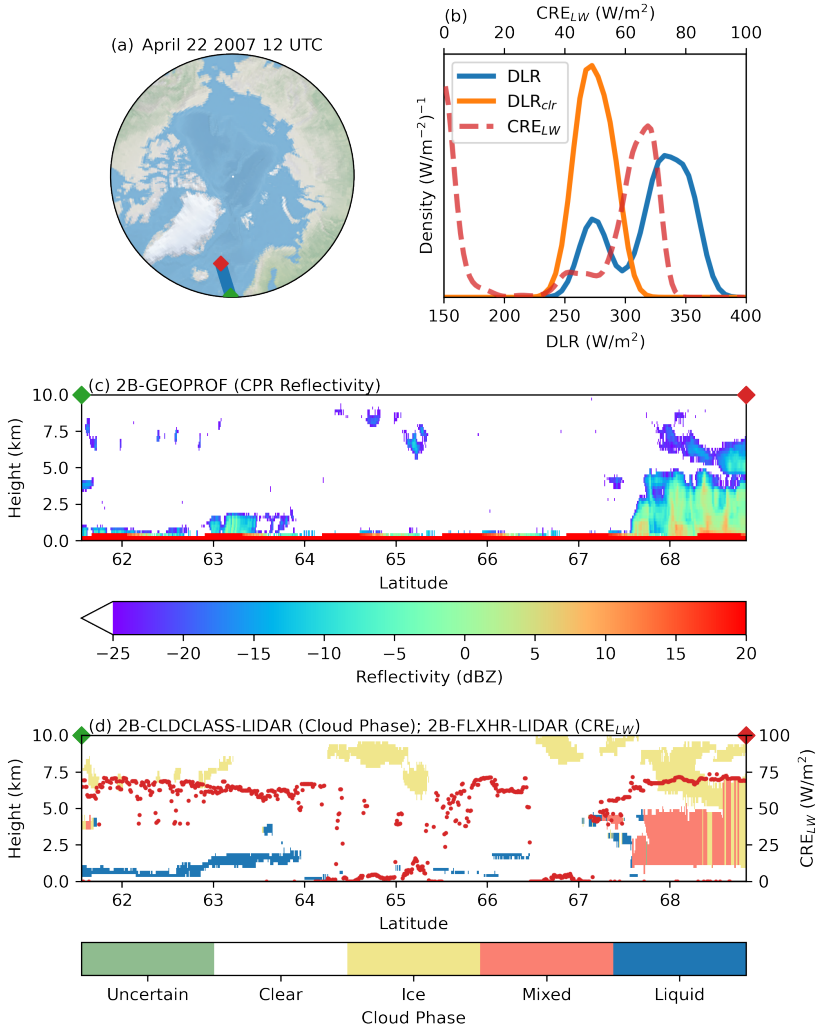

FIGURE A.1: Example CloudSat-CALIPSO swath. (a) Swath location, starting and ending at the green and red diamond, respectively. (b) Probability density functions of DLR (blue), DLR$_{clr}$ (orange), and CRE$_{LW}$ (red) for the scenes contained within the swath. (c) CloudSat's CPR reflectivity for the swath depicted in (a) as a function of height and latitude. (d) As (c) but for cloud phase as determined by 2B-CLDCLASS-LIDAR (color). Values of CRE$_{LW}$ provided by 2B-FLXHR-LIDAR for each scene are included as well (red dot).

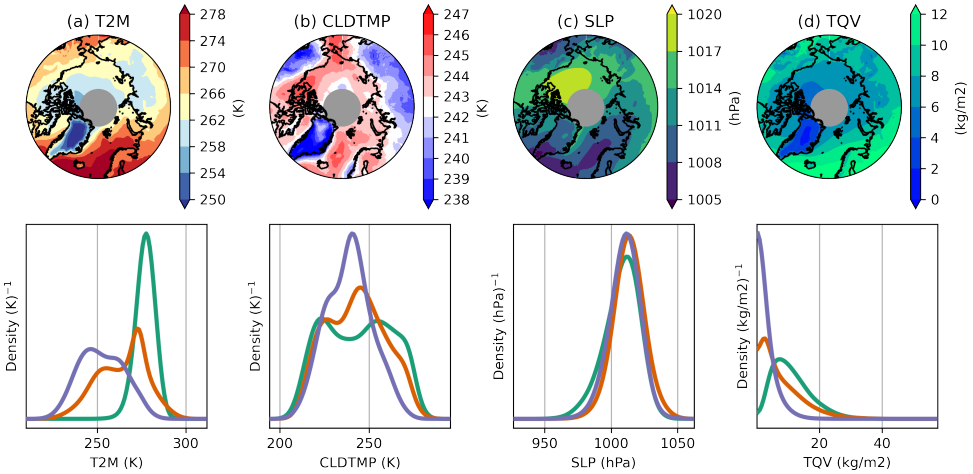

FIGURE A.2: Four Arctic geophysical parameters as determined by MERRA2 reanalysis over 2007-2010. (a) 2-meter temperature, (b) cloud top temperature, (c) mean sea level pressure, (d) total column water vapor. The top row depicts these variables averaged across the four years. The bottom row depicts these variables grouped by the clusters in Fig. 2.3b, using hourly reanalysis data.

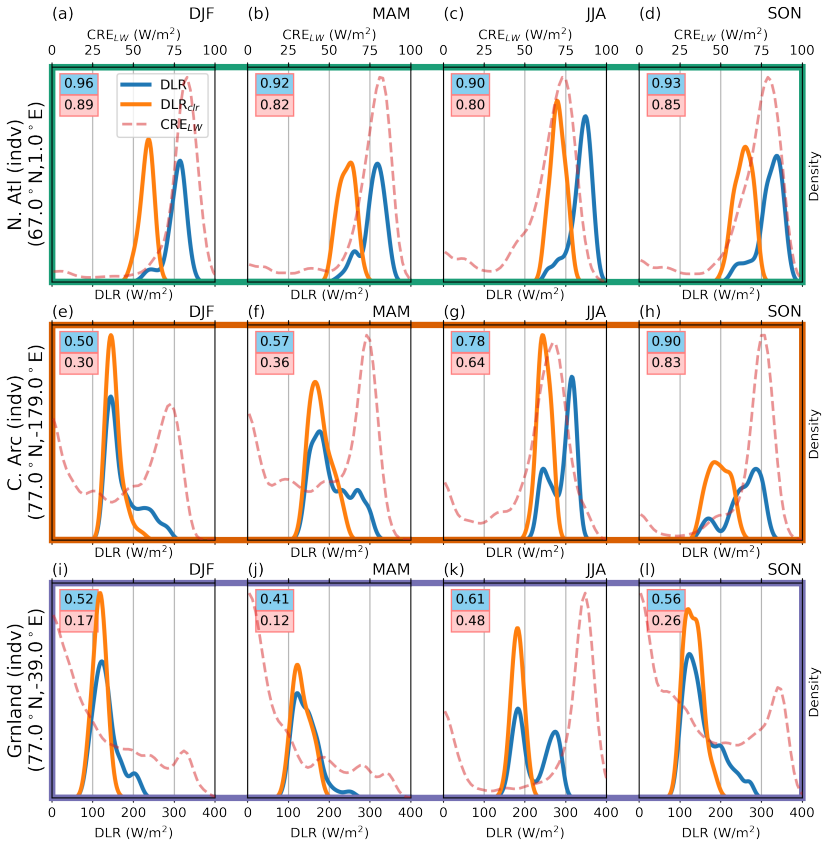

FIGURE A.3: As Fig. 2.5 but for an individual 2x2° gridbox belonging to each clustered region. The gridbox center is listed for each row.

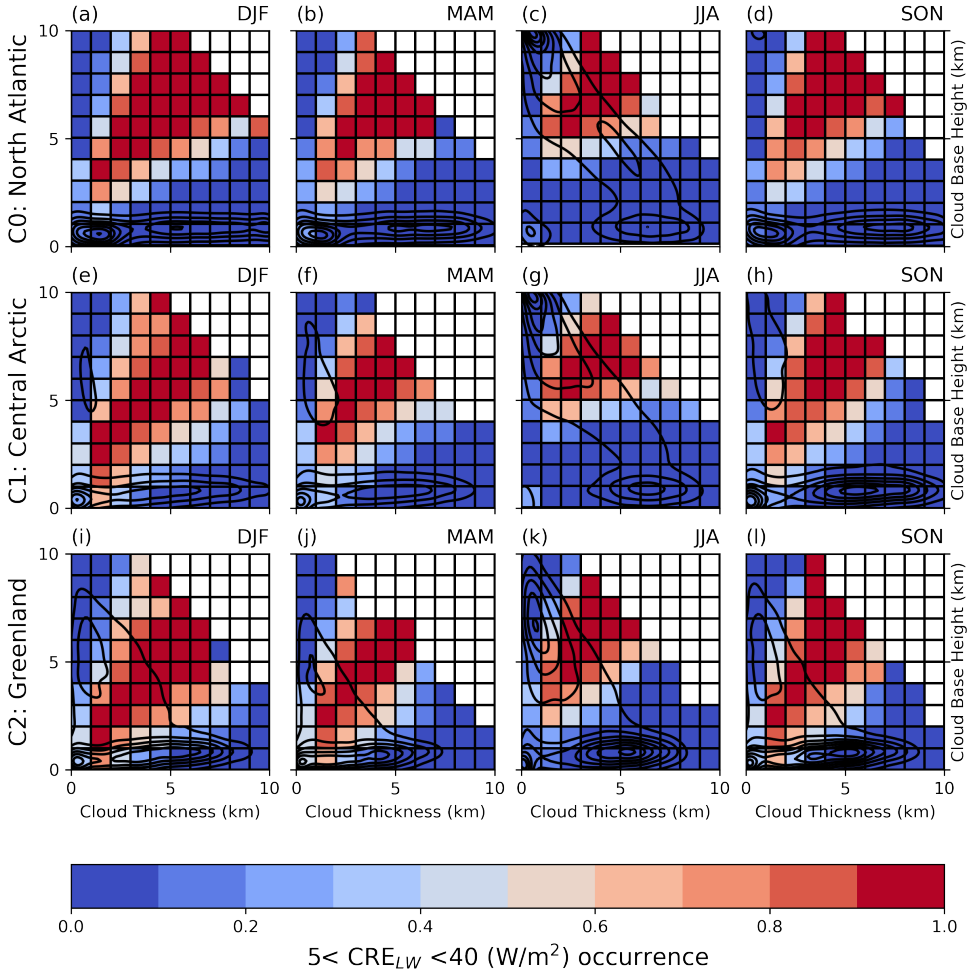

FIGURE A.4: Similar to Fig. 2.11 but showing the frequency of intermediate CRE_{LW} values and broken down by season. Darker shades of red indicate base-thickness combinations that more frequently lead to CRE_{LW} values between the two defined modes. Contours levels do not relate across plots, but only show the relative densities of clouds within each region and season combination.

TABLE A.1: Gaussian Mixture Model values for the DLR density functions presented in Fig. 2.5 (left) and Fig. 2.6 (right).

Arctic Regions							**Antarctic Regions**						
	w	μ_t	σ_t	μ_o	σ_o	D		w	μ_t	σ_t	μ_o	σ_o	D
C0 (DJF)	0.26	241	28	304	20	2.63	C0 (DJF)	0.81	120	19	190	31	2.79
C0 (MAM)	0.26	253	30	310	20	2.18	C0 (MAM)	0.78	093	16	150	33	2.16
C0 (JJA)	0.21	285	25	337	18	2.42	C0 (JJA)	0.75	083	15	130	33	1.81
C0 (SON)	0.24	272	32	324	21	1.89	C0 (SON)	0.76	092	18	144	36	1.81
C1 (DJF)	0.45	149	16	228	39	2.63	C1 (DJF)	0.11	231	19	301	12	4.46
C1 (MAM)	0.46	181	28	273	30	3.13	C1 (MAM)	0.26	222	38	292	17	2.38
C1 (JJA)	0.18	247	13	318	28	3.22	C1 (JJA)	0.44	185	33	273	26	2.95
C1 (SON)	0.34	199	35	287	28	2.75	C1 (SON)	0.27	201	34	282	21	2.86
C2 (DJF)	0.71	137	21	207	31	2.62	C2 (DJF)	0.52	192	30	279	20	3.43
C2 (MAM)	0.73	152	26	234	34	2.70	C2 (MAM)	0.55	152	23	235	29	3.13
C2 (JJA)	0.46	205	24	281	26	3.06	C2 (JJA)	0.59	138	23	215	31	2.84
C2 (SON)	0.61	151	26	238	32	2.95	C2 (SON)	0.57	153	26	237	30	2.99

TABLE A.2: Following the procedure of Tab. 2.2 but for the top of atmosphere upward longwave flux, also known as outgoing longwave radiation (OLR).

	(W/m^2)	DJF	MAM	JJA	SON	Annual
C0	OLRNC	224 (10)	230 (9)	247 (7)	235 (9)	235 (12)
C0	OLR	187 (28)	200 (27)	222 (27)	200 (30)	203 (31)
C0	FREEZE	178 (35)	191 (31)	209 (33)	188 (35)	191 (35)
C0	MELT	209 (14)	220 (13)	239 (11)	223 (13)	225 (15)
C1	OLRNC	183 (17)	207 (20)	242 (11)	211 (20)	212 (27)
C1	OLR	173 (18)	193 (22)	221 (27)	191 (24)	195 (29)
C1	FREEZE	171 (26)	191 (29)	213 (32)	185 (34)	193 (37)
C1	MELT	183 (19)	203 (21)	236 (15)	206 (22)	207 (29)
C2	OLRNC	162 (15)	184 (21)	224 (11)	181 (19)	189 (28)
C2	OLR	156 (15)	179 (20)	211 (20)	174 (19)	181 (27)
C2	FREEZE	155 (21)	179 (24)	209 (24)	172 (25)	180 (32)
C2	MELT	170 (19)	185 (22)	220 (13)	183 (21)	188 (30)

TABLE A.3: Following the procedure of Tab. 2.2 but for the shortwave flux towards the surface (FSDS). Following Haynes et al. (2013), these observations are normalized with the ratio of the diurnally averaged incoming solar flux at TOA to the instantaneous incoming flux at TOA for that location and day of the year, removing some bias caused by the local sampling time. Furthermore, only observations from the ascending orbit (∼1:30 pm local time) are included to avoid artificial inflation in the standard deviation caused by zero shortwave fluxes during periods of no sunlight. That being said, near-zero SW fluxes still occur during winter and fall and assuming a normal distribution (i.e., only considering the mean and standard deviation) may be especially misleading here.

	(W/m^2)	DJF	MAM	JJA	SON	Annual
C0	FSDSNC	14 (21)	238 (97)	336 (65)	67 (63)	169 (146)
C0	FSDS	7 (13)	136 (91)	205 (99)	35 (43)	99 (107)
C0	FREEZE	7 (24)	164 (121)	252 (117)	46 (70)	129 (159)
C0	MELT	7 (24)	132 (123)	217 (104)	29 (73)	80 (166)
C1	FSDSNC	9 (18)	232 (113)	340 (75)	51 (60)	163 (154)
C1	FSDS	7 (15)	175 (99)	232 (113)	29 (41)	114 (124)
C1	FREEZE	7 (19)	196 (127)	273 (117)	38 (65)	138 (163)
C1	MELT	6 (20)	162 (132)	251 (107)	25 (68)	102 (169)
C2	FSDSNC	3 (9)	230 (128)	363 (86)	39 (55)	163 (168)
C2	FSDS	2 (9)	209 (123)	308 (108)	32 (46)	141 (153)
C2	FREEZE	2 (10)	215 (132)	328 (105)	34 (57)	151 (172)
C2	MELT	2 (10)	180 (144)	304 (107)	24 (59)	121 (178)

TABLE A.4: Following the procedure of Tab. A.3 but for the top of atmosphere upward shortwave flux, also known as the outgoing shortwave radiation (OSR).

	(W/m^2)	DJF	MAM	JJA	SON	Annual
C0	OSRNC	6 (8)	44 (31)	43 (16)	17 (13)	28 (25)
C0	OSR	11 (16)	128 (71)	156 (81)	44 (41)	87 (83)
C0	FREEZE	11 (13)	103 (68)	115 (85)	35 (28)	61 (59)
C0	MELT	12 (12)	134 (73)	145 (72)	49 (33)	104 (73)
C1	OSRNC	5 (10)	122 (75)	114 (67)	19 (22)	66 (74)
C1	OSR	6 (12)	150 (85)	187 (84)	35 (41)	97 (99)
C1	FREEZE	6 (11)	139 (82)	158 (90)	29 (30)	81 (82)
C1	MELT	6 (11)	155 (86)	175 (87)	39 (34)	105 (89)
C2	OSRNC	2 (8)	165 (93)	252 (78)	31 (42)	115 (120)
C2	OSR	2 (8)	171 (95)	269 (74)	33 (45)	122 (126)
C2	FREEZE	2 (8)	169 (93)	261 (81)	32 (42)	119 (121)
C2	MELT	2 (8)	182 (97)	273 (84)	36 (43)	130 (123)

Appendix B

Supplementary Material for Chapter 3

To evaluate the impact of CloudSat and CALIPSO's local sampling times of 1:30 AM and 1:30 PM on the derived DLR distributions, similar constraints are applied to reanalysis products for comparison of DLR behavior. Given that the Earth rotates 360 degrees in 24 hours, each hour corresponds to 15 degrees of longitude. Reanalysis products are available for specific UTC times, allowing the calculation of local time based on the distance to the Prime Meridian.

For each validation time, only the gridboxes that align with local times of 1:00 AM and 1:00 PM are selected, corresponding to two separate spans of 15 degrees of longitude. This selection process is repeated for every model validation time. These restricted sampling

times are then used to generate DLR PDFs for analysis (Fig. B.1) and compared to the full sampling rate. While only annual distributions are presented here, results are of the same magnitude when breaking down by season as well.

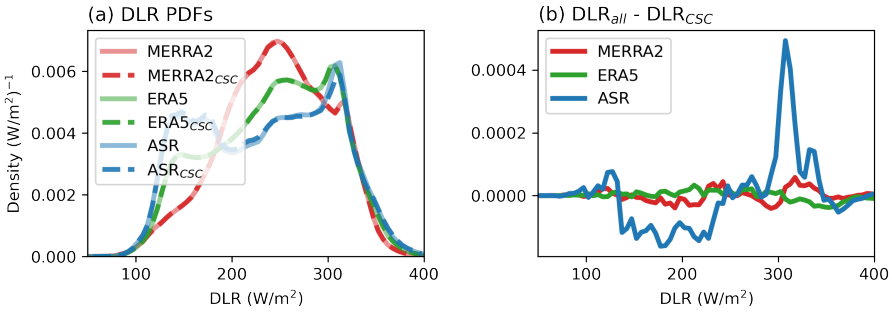

FIGURE B.1: (a) Arctic (poleward of 60 N) DLR distributions for three reanalysis products, MERRA2, ERA5 and ASR. Each product is accompanied by the same distribution only when the product is valid for 1 AM/PM local time (denoted by a subscript 'CSC'), which approximately align with the sampling times of CloudSat and CALIPSO (1:30 AM/PM). For each reanalysis product, the difference in the PDFs when using the full set of reanalysis times versus the limited sampling times is depicted in (b). Note the change in scale from (a) to (b).

Appendix C

Supplementary Material for Chapter 4

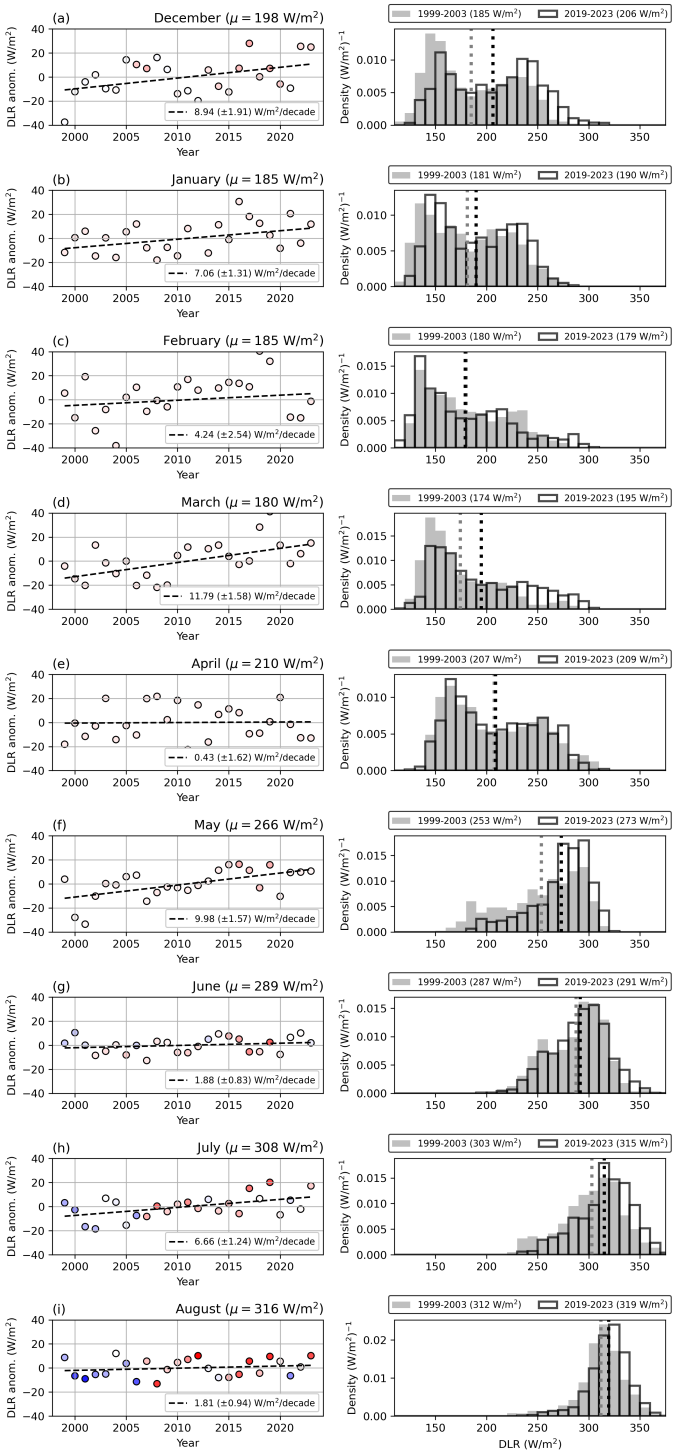

FIGURE C.1: As Fig. 4.3 but for the remaining 9 months (winter, spring, summer).

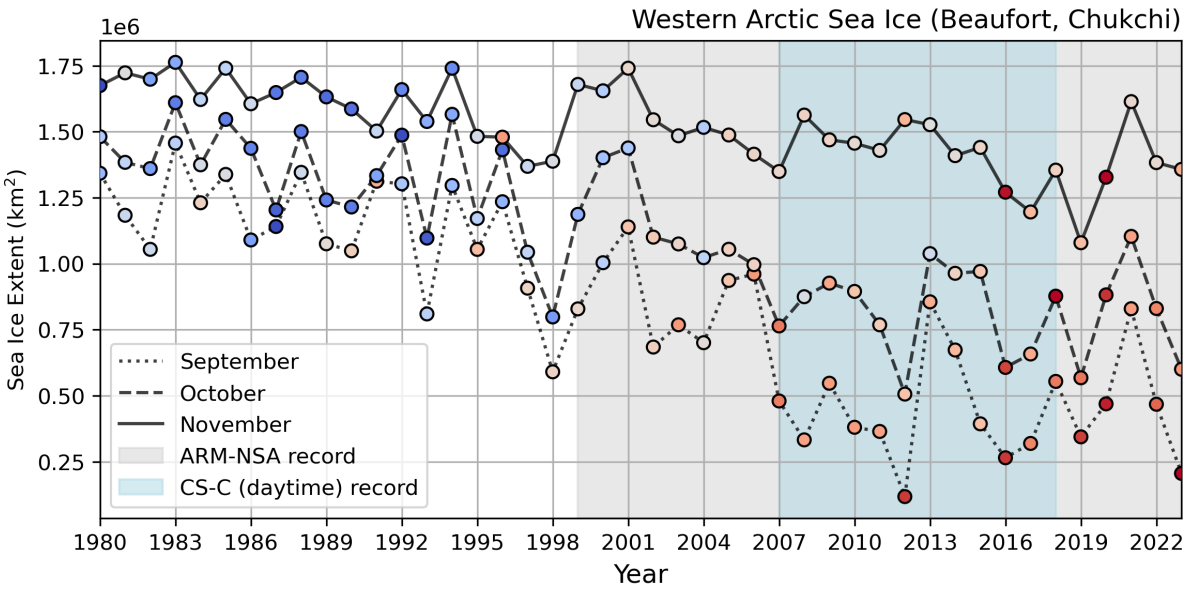

FIGURE C.2: Arctic sea ice extent taken from the NSIDC database (Fetterer et al., 2017), which offers estimates of sea ice extent dating back to November 1978. Sea ice extents are for the sum of the Chukchi and Beaufort Seas, the two bodies of water immediately surrounding the North Slope. Similar patterns are exhibited when including more bodies of water. Colors correspond to monthly mean 2-meter temperature determined by ERA5. Colors are normalized for each month such that dark blue indicates the coldest temperature for that month from 1979-2023 and dark red is the warmest temperature. Colors do not correspond between months. Shading indicates when the ARM-NSA recrod (gray) and CloudSat-CALIPSO daytime 2B-FLXHR-LIDAR product (blue) are active.

Appendix D

Supplementary Material for Chapter 5

Are observations of DLR from the first and final five days of November representative of November as a whole? Here we use a bootstrapping approach with both the ARM-NSA and the CloudSat-CALIPSO daytime record to answer this question. For each observation dataset, 5-year consecutive November DLR distributions are generated using the entire month of observations (black line) and only the first and final five days (red line). In both cases, the limited sampling strategy closely aligns with the full November sampling PDFs, giving indications that the limited sampling used for the model study is sufficient to capture November variability when compiled over enough years.

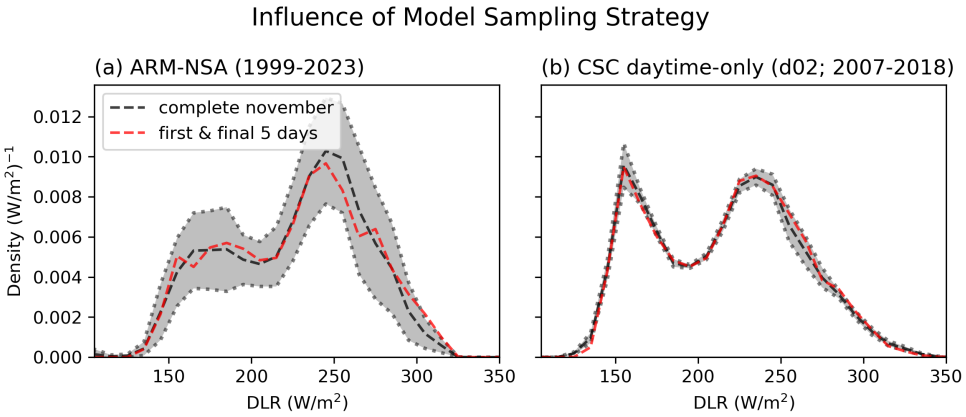

FIGURE D.1: Evaluation of the model sampling strategy. (a) The mean DLR PDF across the different 5-year consecutive Novembers using full sampling from ARM-NSA (black line) and using only observations from the first and final five days, mimicking the model study (red line). Grey shading depicts one standard deviation surrounding the mean. (b) as (a) but using CloudSat-CALIPSO data spanning d02.

Bibliography

Adhikari, L., Z. Wang, and M. Deng, 2012: Seasonal variations of antarctic clouds observed by cloudsat and calipso satellites. *Journal of Geophysical Research: Atmospheres*, **117 (D4)**.

Alapaty, K., J. A. Herwehe, T. L. Otte, C. G. Nolte, O. R. Bullock, M. S. Mallard, J. S. Kain, and J. Dudhia, 2012: Introducing subgrid-scale cloud feedbacks to radiation for regional meteorological and climate modeling. *Geophysical Research Letters*, **39 (24)**.

Albergel, C., E. Dutra, S. Munier, J.-C. Calvet, J. Munoz-Sabater, P. de Rosnay, and G. Balsamo, 2018: Era-5 and era-interim driven isba land surface model simulations: which one performs better? *Hydrology and Earth System Sciences*, **22 (6)**, 3515–3532.

Alekseev, G., S. Kuzmina, L. Bobylev, A. Urazgildeeva, and N. Gnatiuk, 2019: Impact of atmospheric heat and moisture transport on the arctic warming. *Int. J. Climatol*, **39 (8)**, 3582–3592.

Alkama, R., and Coauthors, 2020: Clouds damp the radiative impacts of polar sea ice loss. *The Cryosphere*, **14 (8)**, 2673–2686.

Andreas, A., M. Dooraghi, A. Habte, M. Kutchenreiter, I. Reda, and M. Sengupta, 2018: Solar infrared radiation station (sirs), sky radiation (skyrad), ground radiation (gndrad), and broadband radiometer station (brs) instrument handbook. Tech. rep., DOE Office of Science Atmospheric Radiation Measurement (ARM) Program ....

Arouf, A., H. Chepfer, J. E. Kay, T. S. L'Ecuyer, and J. Lac, 2024: Surface cloud warming increases as late fall arctic sea ice cover decreases. *Geophysical Research Letters*, **51 (3)**, e2023GL105 805.

Arouf, A., and Coauthors, 2022: The surface longwave cloud radiative effect derived from space lidar observations. *Atmospheric Measurement Techniques*, **15 (12)**, 3893–3923.

Ashman, K. M., C. M. Bird, and S. E. Zepf, 1994: Detecting bimodality in astronomical datasets. *arXiv preprint astro-ph/9408030*.

Austin, R. T., A. J. Heymsfield, and G. L. Stephens, 2009: Retrieval of ice cloud microphysical parameters using the cloudsat millimeter-wave radar and temperature. *Journal of Geophysical Research: Atmospheres*, **114 (D8)**.

Avila-Diaz, A., D. H. Bromwich, A. B. Wilson, F. Justino, and S.-H. Wang, 2021: Climate extremes across the north american arctic in modern reanalyses. *Journal of Climate*, **34 (7)**, 2385–2410.

Berger, M., J. Brandefelt, and J. Nilsson, 2013: The sensitivity of the arctic sea ice to orbitally induced insolation changes: a study of the mid-holocene paleoclimate modelling intercomparison project 2 and 3 simulations. *Climate of the Past*, **9 (2)**, 969–982.

Bergeron, T., 1935: On the physics of clouds and precipitation. *Proc. 5th Assembly UGGI, Lisbon, Portugal, 1935*, 156–180.

Bertossa, C., P. Hitchcock, A. DeGaetano, and R. Plougonven, 2021: Bimodality in ensemble forecasts of 2 m temperature: identification. *Weather and Climate Dynamics*, **2 (4)**, 1209–1224.

Bertossa, C., and T. L'Ecuyer, 2024: Two ubiquitous radiative states observed across the high latitudes. *Journal of Climate*, **37 (8)**, 2585–2610.

Blanchard, Y., J. Pelon, C. J. Cox, J. Delanoë, E. W. Eloranta, and T. Uttal, 2021: Comparison of toa and boa lw radiation fluxes inferred from ground-based sensors, a-train satellite observations and era reanalyzes at the high arctic station eureka over the 2002–2020 period. *Journal of Geophysical Research: Atmospheres*, **126 (11)**, e2020JD033 615.

Bromwich, D., and Coauthors, 2018: The arctic system reanalysis, version 2. *Bulletin of the American Meteorological Society*, **99 (4)**, 805–828.

Bromwich, D. H., K. M. Hines, and L.-S. Bai, 2009: Development and testing of polar weather research and forecasting model: 2. arctic ocean. *Journal of Geophysical Research: Atmospheres*, **114 (D8)**.

Bruyère, C. L., J. M. Done, G. J. Holland, and S. Fredrick, 2014: Bias corrections of global models for regional climate simulations of high-impact weather. *Climate Dynamics*, **43**, 1847–1856.

Budyko, M. I., 1969: The effect of solar radiation variations on the climate of the earth. *tellus*, **21 (5)**, 611–619.

Butler, J. H., and S. A. Montzka, 2016: The noaa annual greenhouse gas index (aggi). *NOAA Earth System Research Laboratory*, **58**, 55–75.

Cavalieri, D. J., and C. L. Parkinson, 2012: Arctic sea ice variability and trends, 1979–2010. *The Cryosphere*, **6 (4)**, 881–889.

Cesana, G., J. Kay, H. Chepfer, J. English, and G. De Boer, 2012: Ubiquitous low-level liquid-containing arctic clouds: New observations and climate model constraints from calipso-goccp. *Geophysical Research Letters*, **39 (20)**.

Cho, H., S.-Y. Jun, C.-H. Ho, and G. McFarquhar, 2020: Simulations of winter arctic clouds and associated radiation fluxes using different cloud microphysics schemes in the polar wrf: Comparisons with cloudsat, calipso, and ceres. *Journal of Geophysical Research: Atmospheres*, **125 (2)**, e2019JD031 413.

Cox, C. J., T. Uttal, C. N. Long, M. D. Shupe, R. S. Stone, and S. Starkweather, 2016: The role of springtime arctic clouds in determining autumn sea ice extent. *Journal of Climate*, **29 (18)**, 6581–6596.

Cox, C. J., V. P. Walden, P. M. Rowe, and M. D. Shupe, 2015: Humidity trends imply increased sensitivity to clouds in a warming arctic. *Nature Communications*, **6 (1)**, 10 117.

Cox, C. J., and Coauthors, 2020: The de-icing comparison experiment (d-ice): a study of broadband radiometric measurements under icing conditions in the arctic. *Atmospheric Measurement Techniques Discussions*, **2020**, 1–34.

Cox, C. J., and Coauthors, 2023: Continuous observations of the surface energy budget and meteorology over the arctic sea ice during mosaic. *Scientific Data*, **10 (1)**, 519.

Curry, J., J. Schramm, M. Serreze, and E. Ebert, 1995: Water vapor feedback over the arctic ocean. *Journal of Geophysical Research: Atmospheres*, **100 (D7)**, 14 223–14 229.

Curry, J. A., J. L. Schramm, W. B. Rossow, and D. Randall, 1996: Overview of arctic cloud and radiation characteristics. *Journal of Climate*, **9 (8)**, 1731–1764.

Dai, H., 2023: Role of horizontal heat advection in arctic surface warming during early spring. *Geophysical Research Letters*, **50 (16)**, e2023GL103 234.

Danabasoglu, G., and Coauthors, 2020: The community earth system model version 2 (cesm2). *Journal of Advances in Modeling Earth Systems*, **12 (2)**, e2019MS001 916.

de Boer, G., E. W. Eloranta, and M. D. Shupe, 2009: Arctic mixed-phase stratiform cloud properties from multiple years of surface-based measurements at two high-latitude locations. *Journal of the Atmospheric Sciences*, **66 (9)**, 2874–2887.

Dee, D. P., and Coauthors, 2011: The era-interim reanalysis: Configuration and performance of the data assimilation system. *Quarterly Journal of the royal meteorological society*, **137 (656)**, 553–597.

Deng, M., G. G. Mace, Z. Wang, and E. Berry, 2015: Cloudsat 2c-ice product update with a new ze parameterization in lidar-only region. *Journal of Geophysical Research: Atmospheres*, **120 (23)**, 12–198.

Devasthale, A., M. Tjernström, and A. H. Omar, 2011: The vertical distribution of thin features over the arctic analysed from calipso observations: Part ii: Aerosols. *Tellus B: Chemical and Physical Meteorology*, **63 (1)**, 86–95.

Dodson, J. B., and Coauthors, 2021: Evaluation of simulated cloud liquid water in low clouds over the beaufort sea in the arctic system reanalysis using arise airborne in situ observations. *Atmospheric Chemistry and Physics*, **21 (15)**, 11 563–11 580.

Dong, X., and G. G. Mace, 2003: Arctic stratus cloud properties and radiative forcing derived from ground-based data collected at barrow, alaska. *Journal of Climate*, **16 (3)**, 445–461.

Dong, X., B. Xi, K. Crosby, C. N. Long, R. S. Stone, and M. D. Shupe, 2010: A 10 year climatology of arctic cloud fraction and radiative forcing at barrow, alaska. *Journal of Geophysical Research: Atmospheres*, **115 (D17)**.

Doyle, J., G. Lesins, C. Thackray, C. Perro, G. Nott, T. Duck, R. Damoah, and J. Drummond, 2011: Water vapor intrusions into the high arctic during winter. *Geophysical research letters*, **38 (12)**.

Eastman, R., and S. G. Warren, 2010: Interannual variations of arctic cloud types in relation to sea ice. *Journal of Climate*, **23 (15)**, 4216–4232.

Ebert, E., and Coauthors, 2013: Progress and challenges in forecast verification. *Meteorological Applications*, **20 (2)**, 130–139.

Eirund, G. K., A. Possner, and U. Lohmann, 2019: Response of arctic mixed-phase clouds to aerosol perturbations under different surface forcings. *Atmospheric Chemistry and Physics*, **19 (15)**, 9847–9864.

Eirund, G. K., A. Possner, and U. Lohmann, 2020: The impact of warm and moist airmass perturbations on arctic mixed-phase stratocumulus. *Journal of Climate*, **33 (22)**, 9615–9628.

Engström, A., J. Karlsson, and G. Svensson, 2014: The importance of representing mixed-phase clouds for simulating distinctive atmospheric states in the arctic. *Journal of climate*, **27 (1)**, 265–272.

Ettema, J., M. Van den Broeke, E. Van Meijgaard, W. Van de Berg, J. Box, and K. Steffen, 2010: Climate of the greenland ice sheet using a high-resolution climate model–part 1: Evaluation. *The Cryosphere*, **4 (4)**, 511–527.

Felzer, B., and S. L. Thompson, 2001: Evaluation of a regional climate model for paleoclimate applications in the arctic. *Journal of Geophysical Research: Atmospheres*, **106 (D21)**, 27 407–27 424.

Fetterer, F., K. Knowles, W. N. Meier, M. Savoie, and A. K. Windnagel, 2017: Sea ice index, version 3. National Snow and Ice Data Center, Boulder, Colorado USA,

URL https://doi.org/10.7265/N5K072F8, [Dataset]. Date Last Accessed: 2024-10-03, doi:10.7265/N5K072F8.

Findeisen, W., 1938: Kolloid-meteorologische vorgänge bei neiderschlags-bildung. *Meteor. Z*, **55**, 121–133.

Ford, J. D., T. Pearce, I. V. Canosa, and S. Harper, 2021: The rapidly changing arctic and its societal implications. *Wiley Interdisciplinary Reviews: Climate Change*, **12 (6)**, e735.

Francis, J. A., E. Hunter, J. R. Key, and X. Wang, 2005: Clues to variability in arctic minimum sea ice extent. *Geophysical Research Letters*, **32 (21)**.

Fu, S., X. Deng, M. D. Shupe, and H. Xue, 2019: A modelling study of the continuous ice formation in an autumnal arctic mixed-phase cloud case. *Atmospheric Research*, **228**, 77–85.

Gelaro, R., and Coauthors, 2017: The modern-era retrospective analysis for research and applications, version 2 (merra-2). *Journal of climate*, **30 (14)**, 5419–5454.

Ghanbari, M., M. Arabi, M. Georgescu, and A. M. Broadbent, 2023: The role of climate change and urban development on compound dry-hot extremes across us cities. *Nature communications*, **14 (1)**, 3509.

Ghatak, D., and J. Miller, 2013: Implications for arctic amplification of changes in the strength of the water vapor feedback. *Journal of Geophysical Research: Atmospheres*, **118 (14)**, 7569–7578.

Gimeno, L., M. Vázquez, J. Eiras-Barca, R. Sorí, I. Algarra, and R. Nieto, 2019: Atmospheric moisture transport and the decline in arctic sea ice. *Wiley Interdisciplinary Reviews: Climate Change*, **10 (4)**, e588.

Gimeno-Sotelo, L., R. Nieto, M. Vázquez, and L. Gimeno, 2019: The role of moisture transport for precipitation in the inter-annual and inter-daily fluctuations of the arctic sea ice extension. *Earth System Dynamics*, **10 (1)**, 121–133.

Giorgi, F., and L. O. Mearns, 1991: Approaches to the simulation of regional climate change: a review. *Reviews of geophysics*, **29 (2)**, 191–216.

Goosse, H., and Coauthors, 2018: Quantifying climate feedbacks in polar regions. *Nature communications*, **9 (1)**, 1919.

Graham, R. M., and Coauthors, 2017: A comparison of the two arctic atmospheric winter states observed during n-ice2015 and sheba. *Journal of Geophysical Research: Atmospheres*, **122 (11)**, 5716–5737.

Graham, R. M., and Coauthors, 2019: Evaluation of six atmospheric reanalyses over arctic sea ice from winter to early summer. *Journal of Climate*, **32 (14)**, 4121–4143.

Griesche, H. J., K. Ohneiser, P. Seifert, M. Radenz, R. Engelmann, and A. Ansmann, 2021: Contrasting ice formation in arctic clouds: surface-coupled vs. surface-decoupled clouds. *Atmospheric Chemistry and Physics*, **21 (13)**, 10 357–10 374.

Gu, M., Z. Wang, J. Wei, and X. Yu, 2021: An assessment of arctic cloud water paths in atmospheric reanalyses. *Acta Oceanologica Sinica*, **40 (3)**, 46–57.

Guillaume, A., B. Kahn, Q. Yue, E. Fetzer, S. Wong, G. Manipon, H. Hua, and B. Wilson, 2018: Horizontal and vertical scaling of cloud geometry inferred from cloudsat data. *Journal of the Atmospheric Sciences*, **75 (7)**, 2187–2197.

Ham, S.-H., and Coauthors, 2017: Cloud occurrences and cloud radiative effects (cres) from ceres-calipso-cloudsat-modis (cccm) and cloudsat radar-lidar (rl) products. *Journal of Geophysical Research: Atmospheres*, **122 (16)**, 8852–8884.

Haynes, J. M., R. T. Marchand, Z. Luo, A. Bodas-Salcedo, and G. L. Stephens, 2007: A multipurpose radar simulation package: Quickbeam. *Bulletin of the American Meteorological Society*, **88 (11)**, 1723–1728.

Haynes, J. M., T. H. Vonder Haar, T. L'Ecuyer, and D. Henderson, 2013: Radiative heating characteristics of earth's cloudy atmosphere from vertically resolved active sensors. *Geophysical Research Letters*, **40 (3)**, 624–630.

Henderson, D. S., and T. L'Ecuyer, 2022: Level 2 fluxes and heating rates product process description and interface control document, p2 r05. Technical report, Colorado State University, URL https://www.cloudsat.cira.colostate.edu/cloudsat-static/info/dl/2b-flxhr-lidar/2B-FLXHR-LIDAR_PDICD.P2_R05.rev0.pdf.

Henderson, D. S., T. L'Ecuyer, G. Stephens, P. Partain, and M. Sekiguchi, 2013: A multisensor perspective on the radiative impacts of clouds and aerosols. *Journal of Applied Meteorology and Climatology*, **52 (4)**, 853–871.

Herrmannsdörfer, L., M. Müller, M. D. Shupe, and P. Rostosky, 2023: Surface temperature comparison of the arctic winter mosaic observations, era5 reanalysis, and modis satellite retrieval. *Elem Sci Anth*, **11 (1)**, 00 085.

Hersbach, H., and Coauthors, 2020: The era5 global reanalysis. *Quarterly Journal of the Royal Meteorological Society*, **146 (730)**, 1999–2049.

Hines, K. M., and D. H. Bromwich, 2008: Development and testing of polar weather research and forecasting (wrf) model. part i: Greenland ice sheet meteorology. *Monthly Weather Review*, **136 (6)**, 1971–1989.

Hines, K. M., and D. H. Bromwich, 2017: Simulation of late summer arctic clouds during ascos with polar wrf. *Monthly Weather Review*, **145 (2)**, 521–541.

Hines, K. M., D. H. Bromwich, L. Bai, C. M. Bitz, J. G. Powers, and K. W. Manning, 2015: Sea ice enhancements to polar wrf. *Monthly Weather Review*, **143 (6)**, 2363–2385.

Hines, K. M., D. H. Bromwich, S.-H. Wang, I. Silber, J. Verlinde, and D. Lubin, 2019: Microphysics of summer clouds in central west antarctica simulated by the polar weather research and forecasting model (wrf) and the antarctic mesoscale prediction system (amps). *Atmospheric Chemistry and Physics*, **19 (19)**, 12 431–12 454.

Hinkelman, L. M., and R. Marchand, 2020: Evaluation of ceres and cloudsat surface radiative fluxes over macquarie island, the southern ocean. *Earth and Space Science*, **7 (9)**, e2020EA001 224.

Illingworth, A. J., and Coauthors, 2015: The earthcare satellite: The next step forward in global measurements of clouds, aerosols, precipitation, and radiation. *Bulletin of the American Meteorological Society*, **96 (8)**, 1311–1332.

Inoue, J., and Coauthors, 2021: Clouds and radiation processes in regional climate models evaluated using observations over the ice-free arctic ocean. *Journal of Geophysical Research: Atmospheres*, **126 (1)**, e2020JD033 904.

Jenkins, M. T., and A. Dai, 2022: Arctic climate feedbacks in era5 reanalysis: Seasonal and spatial variations and the impact of sea-ice loss. *Geophysical Research Letters*, **49 (16)**, e2022GL099 263.

Kalesse, H., and Coauthors, 2016: Understanding rapid changes in phase partitioning between cloud liquid and ice in stratiform mixed-phase clouds: An arctic case study. *Monthly Weather Review*, **144 (12)**, 4805–4826.

Kapsch, M.-L., R. G. Graversen, T. Economou, and M. Tjernström, 2014: The importance of spring atmospheric conditions for predictions of the arctic summer sea ice extent. *Geophysical Research Letters*, **41 (14)**, 5288–5296.

Kay, J. E., and A. Gettelman, 2009: Cloud influence on and response to seasonal arctic sea ice loss. *Journal of Geophysical Research: Atmospheres*, **114 (D18)**.

Kay, J. E., M. M. Holland, C. M. Bitz, E. Blanchard-Wrigglesworth, A. Gettelman, A. Conley, and D. Bailey, 2012: The influence of local feedbacks and northward heat

transport on the equilibrium arctic climate response to increased greenhouse gas forcing. *Journal of Climate*, **25 (16)**, 5433–5450.

Kay, J. E., T. L'Ecuyer, A. Gettelman, G. Stephens, and C. O'Dell, 2008: The contribution of cloud and radiation anomalies to the 2007 arctic sea ice extent minimum. *Geophysical Research Letters*, **35 (8)**.

Kay, J. E., T. L'Ecuyer, H. Chepfer, N. Loeb, A. Morrison, and G. Cesana, 2016: Recent advances in arctic cloud and climate research. *Current Climate Change Reports*, **2**, 159–169.

Krayenhoff, E. S., M. Moustaoui, A. M. Broadbent, V. Gupta, and M. Georgescu, 2018: Diurnal interaction between urban expansion, climate change and adaptation in us cities. *Nature Climate Change*, **8 (12)**, 1097–1103.

Kurita, N., 2011: Origin of arctic water vapor during the ice-growth season. *Geophysical Research Letters*, **38 (2)**.

Lacour, A., H. Chepfer, M. D. Shupe, N. B. Miller, V. Noel, J. Kay, D. D. Turner, and R. Guzman, 2017: Greenland clouds observed in calipso-goccp: Comparison with ground-based summit observations. *Journal of Climate*, **30 (15)**, 6065–6083.

L'Ecuyer, T. S., N. B. Wood, T. Haladay, G. L. Stephens, and P. W. Stackhouse Jr, 2008: Impact of clouds on atmospheric heating based on the r04 cloudsat fluxes and heating rates data set. *Journal of Geophysical Research: Atmospheres*, **113 (D8)**.

Listowski, C., and T. Lachlan-Cope, 2017: The microphysics of clouds over the antarctic peninsula–part 2: modelling aspects within polar wrf. *Atmospheric Chemistry and Physics*, **17 (17)**, 10 195–10 221.

Liu, C., and E. A. Barnes, 2015: Extreme moisture transport into the arctic linked to rossby wave breaking. *Journal of Geophysical Research: Atmospheres*, **120 (9)**, 3774–3788.

Liu, Y., 2022: Impacts of active satellite sensors' low-level cloud detection limitations on cloud radiative forcing in the arctic. *Atmospheric Chemistry and Physics*, **22 (12)**, 8151–8173.

Liu, Y., S. A. Ackerman, B. C. Maddux, J. R. Key, and R. A. Frey, 2010: Errors in cloud detection over the arctic using a satellite imager and implications for observing feedback mechanisms. *Journal of Climate*, **23 (7)**, 1894–1907.

Liu, Y., J. R. Key, Z. Liu, X. Wang, and S. J. Vavrus, 2012: A cloudier arctic expected with diminishing sea ice. *Geophysical Research Letters*, **39 (5)**.

Lu, J., and M. Cai, 2009: Seasonality of polar surface warming amplification in climate simulations. *Geophysical Research Letters*, **36 (16)**.

L'Ecuyer, T. S., and Coauthors, 2021: The polar radiant energy in the far infrared experiment: A new perspective on polar longwave energy exchanges. *Bulletin of the American meteorological society*, **102 (7)**, E1431–E1449.

Marty, C., and Coauthors, 2003: Downward longwave irradiance uncertainty under arctic atmospheres: Measurements and modeling. *Journal of Geophysical Research: Atmospheres*, **108 (D12)**.

Maturilli, M., A. Herber, and G. König-Langlo, 2015: Surface radiation climatology for ny-ålesund, svalbard (78.9 n), basic observations for trend detection. *Theoretical and Applied Climatology*, **120**, 331–339.

Matus, A. V., and T. S. L'Ecuyer, 2017: The role of cloud phase in earth's radiation budget. *Journal of Geophysical Research: Atmospheres*, **122 (5)**, 2559–2578.

Maykut, G. A., and P. E. Church, 1973: Radiation climate of barrow alaska, 1962–66. *Journal of Applied Meteorology and Climatology*, **12 (4)**, 620–628.

McArthur, L., 2005: World climate research programme-baseline surface radiation network (bsrn)-operations manual version 2.1.

McGuire, A. D., F. Chapin Iii, J. E. Walsh, and C. Wirth, 2006: Integrated regional changes in arctic climate feedbacks: implications for the global climate system. *Annu. Rev. Environ. Resour.*, **31**, 61–91.

McIlhattan, E. A., J. E. Kay, and T. S. L'Ecuyer, 2020: Arctic clouds and precipitation in the community earth system model version 2. *Journal of Geophysical Research: Atmospheres*, **125 (22)**, e2020JD032 521.

McIlhattan, E. A., T. S. L'Ecuyer, and N. B. Miller, 2017: Observational evidence linking arctic supercooled liquid cloud biases in cesm to snowfall processes. *Journal of Climate*, **30 (12)**, 4477–4495.

Miller, N. B., M. D. Shupe, C. J. Cox, V. P. Walden, D. D. Turner, and K. Steffen, 2015: Cloud radiative forcing at summit, greenland. *Journal of Climate*, **28 (15)**, 6267–6280.

Mioche, G., O. Jourdan, M. Ceccaldi, and J. Delanoë, 2015: Variability of mixed-phase clouds in the arctic with a focus on the svalbard region: a study based on spaceborne active remote sensing. *Atmospheric Chemistry and Physics*, **15 (5)**, 2445–2461.

Monaghan, A., D. Steinhoff, C. Bruyere, and D. Yates, 2014: Ncar cesm global bias-corrected cmip5 output to support wrf/mpas research. UCAR/NCAR-Research Data Archive, [Dataset]. Date Last Accessed: 2024-10-31.

Morrison, A., J. Kay, H. Chepfer, R. Guzman, and V. Yettella, 2018: Isolating the liquid cloud response to recent arctic sea ice variability using spaceborne lidar observations. *Journal of Geophysical Research: Atmospheres*, **123 (1)**, 473–490.

Morrison, A., J. E. Kay, W. Frey, H. Chepfer, and R. Guzman, 2019: Cloud response to arctic sea ice loss and implications for future feedback in the cesm1 climate model. *Journal of Geophysical Research: Atmospheres*, **124 (2)**, 1003–1020.

Morrison, H., J. Curry, and V. Khvorostyanov, 2005: A new double-moment microphysics parameterization for application in cloud and climate models. part i: Description. *Journal of the atmospheric sciences*, **62 (6)**, 1665–1677.

Morrison, H., G. De Boer, G. Feingold, J. Harrington, M. D. Shupe, and K. Sulia, 2012: Resilience of persistent arctic mixed-phase clouds. *Nature Geoscience*, **5 (1)**, 11–17.

Morrison, H., and J. A. Milbrandt, 2015: Parameterization of cloud microphysics based on the prediction of bulk ice particle properties. part i: Scheme description and idealized tests. *Journal of the Atmospheric Sciences*, **72 (1)**, 287–311.

Murto, S., L. Papritz, G. Messori, R. Caballero, G. Svensson, and H. Wernli, 2023: Extreme surface energy budget anomalies in the high arctic in winter. *Journal of Climate*, **36 (11)**, 3591–3609.

Naakka, T., T. Nygård, and T. Vihma, 2018: Arctic humidity inversions: Climatology and processes. *Journal of Climate*, **31 (10)**, 3765–3787.

Nakamura, N., and A. H. Oort, 1988: Atmospheric heat budgets of the polar regions. *Journal of Geophysical Research: Atmospheres*, **93 (D8)**, 9510–9524.

Nygård, T., R. G. Graversen, P. Uotila, T. Naakka, and T. Vihma, 2019: Strong dependence of wintertime arctic moisture and cloud distributions on atmospheric large-scale circulation. *Journal of Climate*, **32 (24)**, 8771–8790.

Nygård, T., T. Naakka, and T. Vihma, 2020: Horizontal moisture transport dominates the regional moistening patterns in the arctic. *Journal of Climate*, **33 (16)**, 6793–6807.

Overland, J., and Coauthors, 2019: The urgency of arctic change. *Polar Science*, **21**, 6–13.

Papritz, L., D. Hauswirth, and K. Hartmuth, 2022: Moisture origin, transport pathways, and driving processes of intense wintertime moisture transport into the arctic. *Weather and Climate Dynamics*, **3 (1)**, 1–20.

Parkinson, C. L., D. J. Cavalieri, P. Gloersen, H. J. Zwally, and J. C. Comiso, 1999: Arctic sea ice extents, areas, and trends, 1978–1996. *Journal of Geophysical Research: Oceans*, **104 (C9)**, 20 837–20 856.

Partain, P., 2004: Cloudsat ecmwf-aux auxiliary data process description and interface control document. *Coop. Inst. for Res. in the Atmos., Colo. State Univ., Fort Collins.*

Pascual-Ahuir, E. G., and Z. Wang, 2023: Optimized sea ice simulation in mitgcm-ecco2 forced by era5. *Ocean Modelling*, **183**, 102 183.

Persson, P., T. Uttal, J. Intrieri, C. Fairall, E. Andreas, and P. Guest, 1999: Observations of large thermal transitions during the arctic night from a suite of sensors at sheba. *Preprints, Fifth Conference on Polar Meteorology and Oceanography*, 10–15.

Persson, P. O. G., M. D. Shupe, D. Perovich, and A. Solomon, 2017: Linking atmospheric synoptic transport, cloud phase, surface energy fluxes, and sea-ice growth: Observations of midwinter sheba conditions. *Climate Dynamics*, **49**, 1341–1364.

Pithan, F., and Coauthors, 2018: Role of air-mass transformations in exchange between the arctic and mid-latitudes. *Nature Geoscience*, **11 (11)**, 805–812.

Prince, H. D., and T. S. L'Ecuyer, 2024: Observed energetic adjustment of the arctic and antarctic in a warming world. *Journal of Climate.*

Protat, A., and Coauthors, 2014: Reconciling ground-based and space-based estimates of the frequency of occurrence and radiative effect of clouds around darwin, australia. *Journal of Applied Meteorology and Climatology*, **53 (2)**, 456–478.

Przybylak, R., R. Sadourny, and L. A. Mysak, 2003: The climate of the arctic.

Raddatz, R., T. Papakyriakou, B. Else, M. Asplin, L. Candlish, R. Galley, and D. Barber, 2015: Downwelling longwave radiation and atmospheric winter states in the western maritime arctic. *International Journal of Climatology*, **35 (9)**, 2339–2351.

Randall, D. A., and Coauthors, 2007: Climate models and their evaluation. *Climate change 2007: The physical science basis. Contribution of Working Group I to the Fourth Assessment Report of the IPCC (FAR)*, Cambridge University Press, 589–662.

Reichler, T., and J. Kim, 2008: How well do coupled models simulate today's climate? *Bulletin of the American Meteorological Society*, **89 (3)**, 303–312.

Riihimaki, L., Y. Shi, and D. Zhang, 2024: Data quality assessment for arm radiation data (qcrad1long). [Dataset]. Date Last Accessed: 2024-12-02, doi:10.5439/1227214.

Rinke, A., M. Maturilli, R. M. Graham, H. Matthes, D. Handorf, L. Cohen, S. R. Hudson, and J. C. Moore, 2017: Extreme cyclone events in the arctic: Wintertime variability and trends. *Environmental Research Letters*, **12 (9)**, 094 006.

Roots, E., 1989: Climate change: high-latitude regions. *Climatic Change*, **15 (1-2)**, 223–253.

Sasirekha, K., and P. Baby, 2013: Agglomerative hierarchical clustering algorithm-a review. *International Journal of Scientific and Research Publications*, **83**, 83.

Sassen, K., Z. Wang, and D. Liu, 2008: Global distribution of cirrus clouds from cloudsat/cloud-aerosol lidar and infrared pathfinder satellite observations (calipso) measurements. *Journal of Geophysical Research: Atmospheres*, **113 (D8)**.

Schweiger, A. J., R. W. Lindsay, S. Vavrus, and J. A. Francis, 2008: Relationships between arctic sea ice and clouds during autumn. *Journal of Climate*, **21 (18)**, 4799–4810.

Sedlar, J., A. Igel, and H. Telg, 2021: Processes contributing to cloud dissipation and formation events on the north slope of alaska. *Atmospheric Chemistry and Physics*, **21 (5)**, 4149–4167.

Sedlar, J., and M. Tjernström, 2009: Stratiform cloud—inversion characterization during the arctic melt season. *Boundary-layer meteorology*, **132 (3)**, 455–474.

Sedlar, J., and Coauthors, 2011: A transitioning arctic surface energy budget: the impacts of solar zenith angle, surface albedo and cloud radiative forcing. *Climate dynamics*, **37**, 1643–1660.

Serreze, M. C., A. P. Barrett, A. G. Slater, M. Steele, J. Zhang, and K. E. Trenberth, 2007: The large-scale energy budget of the arctic. *Journal of Geophysical Research: Atmospheres*, **112 (D11)**.

Serreze, M. C., A. P. Barrett, and J. Stroeve, 2012: Recent changes in tropospheric water vapor over the arctic as assessed from radiosondes and atmospheric reanalyses. *Journal of Geophysical Research: Atmospheres*, **117 (D10)**.

Serreze, M. C., R. G. Barry, M. C. Rehder, and J. E. Walsh, 1995: Variability in atmospheric circulation and moisture flux over the arctic. *Philosophical Transactions of the Royal Society of London. Series A: Physical and Engineering Sciences*, **352 (1699)**, 215–225.

Serreze, M. C., and J. A. Francis, 2006: The arctic amplification debate. *Climatic change*, **76 (3)**, 241–264.

Shaw, J., Z. McGraw, O. Bruno, T. Storelvmo, and S. Hofer, 2022: Using satellite observations to evaluate model microphysical representation of arctic mixed-phase clouds. *Geophysical Research Letters*, **49 (3)**, e2021GL096 191.

Shupe, M., and Coauthors, 2020: The mosaic expedition: A year drifting with the arctic sea ice. *Arctic report card*.

Shupe, M. D., 2011: Clouds at arctic atmospheric observatories. part ii: Thermodynamic phase characteristics. *Journal of Applied Meteorology and Climatology*, **50 (3)**, 645–661.

Shupe, M. D., and J. M. Intrieri, 2004: Cloud radiative forcing of the arctic surface: The influence of cloud properties, surface albedo, and solar zenith angle. *Journal of climate*, **17 (3)**, 616–628.

Shupe, M. D., S. Y. Matrosov, and T. Uttal, 2006: Arctic mixed-phase cloud properties derived from surface-based sensors at sheba. *Journal of the atmospheric sciences*, **63 (2)**, 697–711.

Silber, I., J. Verlinde, M. Cadeddu, C. J. Flynn, A. M. Vogelmann, and E. W. Eloranta, 2019: Antarctic cloud macrophysical, thermodynamic phase, and atmospheric inversion coupling properties at mcmurdo station—part ii: Radiative impact during different synoptic regimes. *Journal of Geophysical Research: Atmospheres*, **124 (3)**, 1697–1719.

Sledd, A., and T. L'Ecuyer, 2019: How much do clouds mask the impacts of arctic sea ice and snow cover variations? different perspectives from observations and reanalyses. *Atmosphere*, **10 (1)**, 12.

Sledd, A., and T. L'Ecuyer, 2021: Emerging trends in arctic solar absorption. *Geophysical Research Letters*, **48 (24)**, e2021GL095 813.

Sledd, A., T. L'Ecuyer, J. Kay, and M. Steele, 2023: Clouds increasingly influence arctic sea surface temperatures as co2 rises. *Geophysical Research Letters*, **50 (8)**, e2023GL102 850.

Solomon, A., M. D. Shupe, O. Persson, H. Morrison, T. Yamaguchi, P. M. Caldwell, and G. de Boer, 2014: The sensitivity of springtime arctic mixed-phase stratocumulus clouds to surface-layer and cloud-top inversion-layer moisture sources. *Journal of the Atmospheric Sciences*, **71 (2)**, 574–595.

Solomon, A., and Coauthors, 2023: The winter central arctic surface energy budget: A model evaluation using observations from the mosaic campaign. *Elem Sci Anth*, **11 (1)**, 00 104.

Sorteberg, A., and J. E. Walsh, 2008: Seasonal cyclone variability at 70 n and its impact on moisture transport into the arctic. *Tellus A: Dynamic Meteorology and Oceanography*, **60 (3)**, 570–586.

Stamnes, K., R. Ellingson, J. Curry, J. Walsh, and B. Zak, 1999: Review of science issues, deployment strategy, and status for the arm north slope of alaska–adjacent arctic ocean climate research site. *Journal of Climate*, **12 (1)**, 46–63.

Stengel, M., C. Schlundt, S. Stapelberg, O. Sus, S. Eliasson, U. Willén, and J. F. Meirink, 2018: Comparing era-interim clouds with satellite observations using a simplified satellite simulator. *Atmospheric Chemistry and Physics*, **18 (23)**, 17 601–17 614.

Stephens, G. L., P. M. Gabriel, and P. T. Partain, 2001: Parameterization of atmospheric radiative transfer. part i: Validity of simple models. *Journal of the atmospheric sciences*, **58 (22)**, 3391–3409.

Stephens, G. L., and Coauthors, 2002: The cloudsat mission and the a-train: A new dimension of space-based observations of clouds and precipitation. *Bulletin of the American Meteorological Society*, **83 (12)**, 1771–1790.

Stramler, K., A. D. Del Genio, and W. B. Rossow, 2011a: Synoptically driven arctic winter states. *Journal of Climate*, **24 (6)**, 1747–1762.

Stramler, K., A. D. Del Genio, and W. B. Rossow, 2011b: Synoptically driven arctic winter states. *Journal of Climate*, **24 (6)**, 1747–1762.

Stroeve, J., and D. Notz, 2018: Changing state of arctic sea ice across all seasons. *Environmental Research Letters*, **13 (10)**, 103 001.

Stroeve, J. C., T. Markus, L. Boisvert, J. Miller, and A. Barrett, 2014: Changes in arctic melt season and implications for sea ice loss. *Geophysical Research Letters*, **41 (4)**, 1216–1225.

Stroeve, J. C., M. C. Serreze, M. M. Holland, J. E. Kay, J. Malanik, and A. P. Barrett, 2012: The arctic's rapidly shrinking sea ice cover: a research synthesis. *Climatic change*, **110**, 1005–1027.

Tan, I., and T. Storelvmo, 2019: Evidence of strong contributions from mixed-phase clouds to arctic climate change. *Geophysical Research Letters*, **46 (5)**, 2894–2902.

Taylor, P. C., R. C. Boeke, Y. Li, and D. W. Thompson, 2019: Arctic cloud annual cycle biases in climate models. *Atmospheric Chemistry and Physics*, **19 (13)**, 8759–8782.

Taylor, P. C., B. M. Hegyi, R. C. Boeke, and L. N. Boisvert, 2018: On the increasing importance of air-sea exchanges in a thawing arctic: A review. *Atmosphere*, **9 (2)**, 41.

Taylor, P. C., S. Kato, K.-M. Xu, and M. Cai, 2015: Covariance between arctic sea ice and clouds within atmospheric state regimes at the satellite footprint level. *Journal of Geophysical Research: Atmospheres*, **120 (24)**, 12 656–12 678.

Taylor, P. C., and E. Monroe, 2023: Isolating the surface type influence on arctic low-clouds. *Journal of Geophysical Research: Atmospheres*, **128 (16)**, e2022JD038 098.

Tjernström, M., J. Sedlar, and M. D. Shupe, 2008: How well do regional climate models reproduce radiation and clouds in the arctic? an evaluation of arcmip simulations. *Journal of Applied Meteorology and Climatology*, **47 (9)**, 2405–2422.

Tjernström, M., M. D. Shupe, I. M. Brooks, P. Achtert, J. Prytherch, and J. Sedlar, 2019: Arctic summer airmass transformation, surface inversions, and the surface energy budget. *Journal of Climate*, **32 (3)**, 769–789.

Tomas, R. A., C. Deser, and L. Sun, 2016: The role of ocean heat transport in the global climate response to projected arctic sea ice loss. *Journal of Climate*, **29 (19)**, 6841–6859.

Urraca, R., T. Huld, A. Gracia-Amillo, F. J. Martinez-de Pison, F. Kaspar, and A. Sanz-Garcia, 2018: Evaluation of global horizontal irradiance estimates from era5 and cosmo-rea6 reanalyses using ground and satellite-based data. *Solar Energy*, **164**, 339–354.

Uttal, T., and Coauthors, 2002: Surface heat budget of the arctic ocean. *Bulletin of the American Meteorological Society*, **83 (2)**, 255–276.

Van Tricht, K., and Coauthors, 2016: Clouds enhance greenland ice sheet meltwater runoff. *Nature communications*, **7 (1)**, 10 266.

Vannitsem, S., D. S. Wilks, and J. Messner, 2018: *Statistical postprocessing of ensemble forecasts*. Elsevier.

Vihma, T., 2014: Effects of arctic sea ice decline on weather and climate: A review. *Surveys in Geophysics*, **35**, 1175–1214.

Vihma, T., and Coauthors, 2016: The atmospheric role in the arctic water cycle: A review on processes, past and future changes, and their impacts. *Journal of Geophysical Research: Biogeosciences*, **121 (3)**, 586–620.

Walden, V. P., S. R. Hudson, L. Cohen, S. Y. Murphy, and M. A. Granskog, 2017: Atmospheric components of the surface energy budget over young sea ice: Results from the n-ice2015 campaign. *Journal of Geophysical Research: Atmospheres*, **122 (16)**, 8427–8446.

Wang, C., R. M. Graham, K. Wang, S. Gerland, and M. A. Granskog, 2019: Comparison of era5 and era-interim near-surface air temperature, snowfall and precipitation over arctic sea ice: effects on sea ice thermodynamics and evolution. *The Cryosphere*, **13 (6)**, 1661–1679.

Wang, Z., and Coauthors, 2013: Cloudsat project. *Level 2 Combined Radar and Lidar Cloud Scenario Classification Product Process Description and Interface Control Document*, 61.

Wehr, T., and Coauthors, 2023: The earthcare mission–science and system overview. *EGUsphere*, **2023**, 1–47.

Wielicki, B. A., B. R. Barkstrom, E. F. Harrison, R. B. Lee III, G. L. Smith, and J. E. Cooper, 1996: Clouds and the earth's radiant energy system (ceres): An earth observing system experiment. *Bulletin of the American Meteorological Society*, **77 (5)**, 853–868.

Willis, M. D., W. R. Leaitch, and J. P. Abbatt, 2018: Processes controlling the composition and abundance of arctic aerosol. *Reviews of Geophysics*, **56 (4)**, 621–671.

Wilson, A. B., D. H. Bromwich, and K. M. Hines, 2011: Evaluation of polar wrf forecasts on the arctic system reanalysis domain: Surface and upper air analysis. *Journal of Geophysical Research: Atmospheres*, **116 (D11)**.

Winker, D. M., W. H. Hunt, and M. J. McGill, 2007: Initial performance assessment of caliop. *Geophysical Research Letters*, **34 (19)**.

Wood, R., and P. R. Field, 2011: The distribution of cloud horizontal sizes. *Journal of Climate*, **24 (18)**, 4800–4816.

Woods, C., and R. Caballero, 2016: The role of moist intrusions in winter arctic warming and sea ice decline. *Journal of Climate*, **29 (12)**, 4473–4485.

Woods, C., R. Caballero, and G. Svensson, 2013: Large-scale circulation associated with moisture intrusions into the arctic during winter. *Geophysical Research Letters*, **40 (17)**, 4717–4721.

Xue, J., Z. Xiao, D. H. Bromwich, and L. Bai, 2022: Polar wrf v4. 1.1 simulation and evaluation for the antarctic and southern ocean. *Frontiers of Earth Science*, **16 (4)**, 1005–1024.

Yeo, H., M.-H. Kim, S.-W. Son, J.-H. Jeong, J.-H. Yoon, B.-M. Kim, and S.-W. Kim, 2022: Arctic cloud properties and associated radiative effects in the three newer reanalysis datasets (era5, merra-2, jra-55): Discrepancies and possible causes. *Atmospheric Research*, **270**, 106 080.

Yu, Y., P. C. Taylor, and M. Cai, 2019: Seasonal variations of arctic low-level clouds and its linkage to sea ice seasonal variations. *Journal of geophysical research: Atmospheres*, **124 (22)**, 12 206–12 226.

Zampieri, L., F. Kauker, J. Fröhle, H. Sumata, E. C. Hunke, and H. F. Goessling, 2021: Impact of sea-ice model complexity on the performance of an unstructured-mesh sea-ice/ocean model under different atmospheric forcings. *Journal of Advances in Modeling Earth Systems*, **13 (5)**, e2020MS002 438.

Zhang, D., 2003: Data quality assessment for arm radiation data (qcrad1long). 2007-01-01 to 2010-12-31, North Slope Alaska (NSA) Central Facility, Barrow AK (C1), Compiled by D. Zhang. ARM Data Center. Data set accessed 2023-07-17 at http://dx.doi.org/10.5439/1227214.

Zhang, D., J. Comstock, H. Xie, and Z. Wang, 2022: Polar aerosol vertical structures and characteristics observed with a high spectral resolution lidar at the arm nsa observatory. *Remote Sensing*, **14 (18)**, 4638.

Zhao, C., and T. J. Garrett, 2015: Effects of arctic haze on surface cloud radiative forcing. *Geophysical Research Letters*, **42 (2)**, 557–564.

Zou, X., D. H. Bromwich, A. Montenegro, S.-H. Wang, and L. Bai, 2021: Major surface melting over the ross ice shelf part ii: Surface energy balance. *Quarterly Journal of the Royal Meteorological Society*, **147 (738)**, 2895–2916.

Zwally, H. J., W. Abdalati, T. Herring, K. Larson, J. Saba, and K. Steffen, 2002: Surface melt-induced acceleration of greenland ice-sheet flow. *Science*, **297 (5579)**, 218–222.